Predicting the Equilibria of Point Defects in Zirconium Oxide: A Route to Understand the Corrosion and Hydrogen Pickup of Zirconium Alloys

By

Mostafa Youssef Mahmoud Youssef

B.S., Nuclear Engineering (2006)
Alexandria University, Egypt

S.M., Nuclear Science and Engineering (2010)
Massachusetts Institute of Technology

Submitted to the Department of Nuclear Science and Engineering
in Partial Fulfillment of the Requirements for the Degree of
Doctor of Philosophy in Nuclear Science and Engineering
at the
MASSACHUSETTS INSTITUTE OF TECHNOLOGY

February 2014

Author: ________________________
Mostafa Youssef Mahmoud Youssef
Department of Nuclear Science and Engineering
September 27, 2013

Certified by: ________________________
Bilge Yildiz
Associate Professor of Nuclear Science and Engineering
Thesis Supervisor

Certified by: ________________________
Sidney Yip
Professor Emeritus of Nuclear Science and Engineering, and Materials Science and Engineering
Thesis Reader

Accepted by: ________________________
Mujid S. Kazimi
TEPCO Professor of Nuclear Engineering
Chair, Department Committee on Graduate Students

Predicting the Equilibria of Point Defects in Zirconium Oxide: A Route to Understand the Corrosion and Hydrogen Pickup of Zirconium Alloys

by
Mostafa Youssef Mahmoud Youssef
Submitted to the Department of Nuclear science and Engineering
on September 27, 2013 in Partial Fulfillment of the
Requirements for the Degree of Doctor of Philosophy in
Nuclear Science and Engineering

ABSTRACT

The performance of zirconium alloys in nuclear reactors is compromised by corrosion and hydrogen pickup. The thermodynamics and kinetics of these two processes are governed by the behavior of point defects in the ZrO_2 layer that grows natively on these alloys. In this thesis, we developed a general, broadly applicable framework to predict the equilibria of point defects in a metal oxide. The framework is informed by density functional theory and relies on notions of statistical mechanics. Validation was performed on the tetragonal and monoclinic phases of ZrO_2 by comparison with prior conductivity experiments. The framework was applied to four fundamental problems for understanding the corrosion and hydrogen pickup of zirconium alloys.

First, by coupling the predicted concentrations of oxygen defects in tetragonal ZrO_2 with their calculated migration barriers, we determined oxygen self-diffusivity in a wide range of thermodynamic conditions spanning from the metal-oxide interface to the oxide-water interface. This facilitates future macro-scale modeling of the oxide layer growth kinetics on zirconium alloys.

Second, using the computed defect equilibria of the tetragonal and monoclinic phases, we constructed a temperature-oxygen partial pressure phase diagram for ZrO_2. The diagram showed that the tetragonal phase can be stabilized below its atmospheric transition-temperature by lowering the oxygen chemical potential. This work adds a new explanation to the stabilization of the tetragonal phase at the metal-oxide interface where the oxygen partial pressure is low.

Third, using the developed framework, we modeled co-doping of monoclinic ZrO_2 with hydrogen and a transition metal. Our modeling predicted a volcano-like dependence of hydrogen (proton) solubility on the first-row transition metals, which is consistent with a set of systematic experiments from the nuclear industry. We discovered that the reason behind this behavior is the ability of the transition metal to p-type-dope ZrO_2 and hence lower the chemical potential of electron. Therefore, the peak of the hydrogen solubility in monoclinic ZrO_2 also corresponds to an increased barrier for hydrogen gas evolution on the surface. This explanation opens the door to physics-based design of resistant zirconium alloys, and qualitatively consistent with the monoclinic ZrO_2.

Finally, we uncovered the interplay between certain hydrogen defects and planar compressive stress which tetragonal ZrO_2 experiences on zirconium alloys. The stress enhances the abundance of these defects, while these same defects tend to relax the stress. This interplay was used to propose an oxide fracture mechanism by which hydrogen is picked up.

Thesis Supervisor: Bilge Yildiz
Title: Associate Professor of Nuclear Science and Engineering

To my mother Mervat and my sister Dalia for their unconditional love.

Acknowledgements

I'm very thankful to my advisor Professor Bilge Yildiz for her mentorship, guidance and support throughout my PhD. I remain indebted to her in every stage in my academic career.

I thank my thesis reader, Professor Sidney Yip, my thesis committee member, Professor Ju Li, my thesis defense committee member, Professor Jeffrey Grossman, the staff at the Nuclear Science and Engineering Department and all the members of the Yildiz group.

I owe special thanks to my friends Ahmed Hamed, Abdel-Rahman Hassan, Khaled Moharam and my dearest mentor Dr. Amr Mohamed.

This research was supported by the Consortium for Advanced Simulation of Light Water Reactors (CASL), an Energy Innovation Hub for Modeling and Simulation of Nuclear Reactors under U.S. Department of Energy Contract No. DE-AC05-00OR22725. We acknowledge the National Science Foundation for computational support through the XSEDE Science Gateways program with the research allocation (TG-DMR120025).

Contents

Chapter 1 : Motivation and thesis contribution....17

1.1 Motivation....17
1.2 Thesis contribution....19
1.3 Thesis organization....22

Chapter 2 : Literature review of waterside corrosion and hydrogen pickup of zircaloy-4....23

2.1 Water Side Oxidation of Zircaloy-4....24
  2.1.1 Corrosion Kinetics....24
  2.1.2 Zircaloy-4 oxidation as an electrochemical process....25
  2.1.3 Transport processes through the oxide layer....26
    2.1.3.1 Oxygen transport....28
    2.1.3.2 Zirconium transport....34
    2.1.3.3 Electron transport....34
  2.1.4 Oxide phases, microstructure, stoichiometry and stresses....36
    2.1.4.1 Oxide phases....37
    2.1.4.2 Microstructure....40
    2.1.4.3 Stoichiometry....42
    2.1.4.4 Stress state....43
    2.1.4.5 The origin of the transition from cubic to linear growth law....45
2.2 Factors that accelerate the corrosion kinetics....47
  2.2.1 Lithium and boron effects....47
    2.2.1.1 Observed phenomena related to the role of lithium hydroxide and boric acid....47
    2.2.1.2 Hypotheses in the literature to explain the role of lithium and boric acid....50
  2.2.2 The role of secondary phase particles (SPP)....51
  2.2.3 CRUD induced localized corrosion (CILC)....52
2.3 Hydrogen pickup and its relation to corrosion kinetics....54
  2.3.1 Hydrogen pickup and its transport....54
  2.3.2 Effect of hydrogen on the corrosion kinetics....58

Chapter 3 : Modeling defect equilibria in metal oxides: Application to tetragonal and monoclinic zirconium oxide....61

Abstract....61
3.1 Introduction....62
3.2 Theoretical approach to model charged point defect equilibria in a metal oxide....62

3.2.1 Thermodynamics of the formation point defects 63
3.2.2 Construction of the Kröger-Vink diagram 66
3.2.3 Finite temperature effects 68
3.2.4 Density functional theory calculations 71
3.3 Defect equilibria in tetragonal zirconium oxide 73
3.3.1 Defect formation energies at 0K 74
3.3.2 Defect equilibria at finite temperature 78
3.3.2.1 The Kröger-Vink diagram at 1500 K 80
3.3.2.2 The Kröger-Vink diagram at 2000 K 81
3.3.2.3 Comparison with experiments 82
3.3.2.4 Origins of the gap between theory and experiment 83
3.3.3 Off-stoichiometry and electron chemical potential 84
3.3.4 Defect atomic and electronic structures 86
3.4 Defect equilibria in monoclinic zirconium oxide 88
3.4.1 0K formation energies 88
3.4.2 Defect equilibria at finite temperature 89
3.4.2.1 The Kröger-Vink diagram at 1200K 89
3.4.2.2 The Kröger-Vink diagram at 600 K 90
3.5 The accuracy of the Makov-Payne correction 91
3.6 Correcting the O_2 molecule overbinding 94

Chapter 4 : Predicting self-diffusion of oxygen in tetragonal zirconium oxide from first principles 97

Abstract 97
4.1 Introduction 97
4.2 Theoretical and computational approach 99
4.3 The migration barriers of oxygen defects 101
4.4 Analysis of the self-diffusivity of oxygen in tetragonal zirconia 103
4.5 Conclusion 109

Chapter 5 : The role of defects in the thermodynamics of monoclinic-tetragonal phase transition in zirconium oxide 110

Abstract 110
5.1 Introduction 110
5.2 Theoretical and computational approach 111
5.3 The tetragonal-monoclinic phase transition temperature 113

Chapter 6 : Hydrogen defects in tetragonal zirconium oxide 116

Abstract 116
6.1 Introduction 116
6.2 Theoretical and computational approach 119
  6.2.1 Defect structures and charges 119
  6.2.2 Defect energetics 122
  6.2.3 Density functional theory calculations 125
6.3 The energetics of hydrogen defects in tetragonal zirconia 126
  6.3.1 Formation energies and thermodynamic transition levels 126
  6.3.2 Binding energies 130
6.4 The atomic and electronic structure of hydrogen defects in tetragonal zirconia 132
  6.4.1 Interstitial defects 132
  6.4.2 Hydrogen-oxygen vacancy complexes 135
  6.4.3 Hydrogen-zirconium vacancy complexes 138
6.5 On the adequacy of Makov-Payne correction for hydrogen defects in tetragonal ZrO_2 141
6.6 Conclusion 144

Chapter 7 : The interplay between planar stress and hydrogen defects in tetragonal zirconium oxide 146

Abstract 146
7.1 Introduction 146
7.2 Computational details 148
7.3 The interplay between hydrogen defects and the biaxial stress 148
  7.3.1 Defect-free (001) and (101) tetragonal ZrO_2 grains under biaxial compression 148
  7.3.2 Interplay between biaxial compressive stress and hydrogen defects in (001) and (101) tetragonal ZrO_2 grains 150
7.4 Implication for the mechanism of hydrogen pickup 153

Chapter 8 : The impact of transition metal dopants on the hydrogen pickup capacity of zirconium oxide – solubility and surface reactivity 155

Abstract 155
8.1 Introduction 155
8.2 Computational approach 158
  8.2.1 Defect structures and charges 158
  8.2.2 Defect energetics and Kröger-Vink diagrams 159
  8.2.3 Density functional theory calculations 162

8.3 Hydrogen doped monoclinic ZrO_2 162
8.4 The origin of the hydrogen pickup volcano 163

Chapter 9 : Epilogue 167

9.1 Summary 167
9.2 Suggested future directions 169

Bibliography 172

List of Figures

Figure 1-1: Schematic of the zirconium oxide passive layer that grows natively on zirconium alloys. SPP denotes the metallic secondary phase particles (alloying elements). 18

Figure 2-1: Schematic of zirconium oxidation quantified in terms of weight gain vs. time [12]. 25

Figure 2-2: The conventional unit cells of atmospheric pressure phases of zirconia. (a) cubic, (b) tetragonal. (c) monoclinic. Zirconium ions are blue and oxygen ions are red. Figure is adapted from [23]. 28

Figure 2-3: The formation energy of neutral, singly and doubly charged F-centers in zirconia as a function of the Fermi level [26]. 29

Figure 2-4: The diffusion coefficient of oxygen in various zirconia samples [18]. 31

Figure 2-5: Average radius of the pores as a function of the oxide thickness evaluated by out-of-pile loop mercury measurements [34] 33

Figure 2-6: The total chemical diffusion coefficient in zirconia; the upper line is deduced from measured tracer diffusivities in single crystal tetragonal zirconia. The two lower lines are obtained from corrosion kinetic data. The figure is adapted from Ref. [30]. 35

Figure 2-7: Hypothetical pressure-temperature phase diagram for zirconia [44]......................... 38

Figure 2-8: Zirconium-Oxygen phase diagram [11]. 39

Figure 2-9: TEM images (top) and sketch of grains (bottom) of the oxide layer on (a) Zircaloy-4, (b) ZIRLO and (c) Zr-2.5Nb alloys near the metal/oxide interface in 360 ^{0}C. The arrows indicate the growth directions [48]. 41

Figure 2-10: (a) Long-term reference oxidation kinetics. (b) Microscopic observation of the oxide layer of Zircaloy-4 in autoclave at 360 ^{0}C in 3.5 ppm LiOH and 1000 ppm H_3BO_3 chemistry [50]. 42

Figure 2-11: Measured oxygen content fromzircaloy-4 oxide formed in 360 ^{0}C pure water environment using EDS point spectra in TEM [48]. 43

Figure 2-12: Measured stress vs. oxide film thickness [51]. 44

Figure 2-13: Corrosion weight gain vs. exposure time of Zircaloy-4, ZIRLO and Zr-2.5Nb in (a) 360 0C pure water (solid arrows show the transition) and (b) 360 0C lithiated water (solid arrow shows transition in ZIRLO, transition is not discernible in Zircaloy-r and Zr-2.5Nb) [48]......... 48

Figure 2-14: Lithium enrichment in the oxide layers as a function of void fraction in out-of-pile-loop tests [34] 49

Figure 2-15: Effect of secondary phase particles size on corrosion [10]..................................... 51

Figure 2-16: Thermal impact of CRUD deposition [11]. 53

Figure 2-17: The effect of alloying elements on hydrogen pickup percentage [8]....................... 56

Figure 2-18: Temperature dependence of hydrogen solubility in some oxides [73]. 57

Figure 2-19: Corrosion behavior and hydrogen pick-up of Zircaloy-4 in pure water at 360 ^{0}C [78]. 59

Figure 2-20: Schematic diagram of the morphology of the oxide before and after transition [78]. 60

Figure 3-1: (a) Corrections to the free energy of formation of the neutral oxygen vacancy due to the change in the phonon vibrations and the electronic entropy in the solid. (b) The total electronic density of states (DOS) for tetragonal ZrO_2 in a perfect supercell and in a supercell with a neutral oxygen vacancy. The arrow in (b) indicates the electronic state in the gap due to the neutral oxygen vacancy that enhances the electronic entropy of the defect. The position and magnitude of the resonance (in (a)) between μ_F and the defect state (in (b)) depends on temperature and oxygen partial pressure. 71

Figure 3-2: Defect formation energies as a function of the electron chemical potential. (a) Oxygen defects. (b) Zirconium vacancies. (d) Zirconium interstitials. (d) The thermodynamic transition levels for the native defects determined from (a,b,c). 76

Figure 3-3: Calculated Kröger-Vink diagram for tetragonal ZrO_2 at (a) 1500 K using the DFT predicted band gap of 3.9 eV, (b) 1500 K using the experimental band gap of 4.2 eV, (c) 2000 K using the DFT predicted band gap. (d) Conductivity measurements on tetragonal zirconia by Kofstad and Ruzicka [120]. In a,b,c only the defects that have concentrations greater than 10^{-8} are shown. The dash-dot lines in a,b,c,d are guide for the eye showing the (-1/2) and (-1/6) slopes 79

Figure 3-4: (a) Off-stoichiometry in ZrO_{2+x} as a function of the oxygen partial pressure, P_{O_2}, at different temperatures. The dependence of the electron chemical potential, μ_F, on the oxygen partial pressure at different temperatures (b), and on the off-stoichiometry, x, at different temperatures (c). 85

Figure 3-5: Native defect formation energies in monoclinic ZrO_2 as a function of the chemical potential of electrons. The chemical potential of oxygen was set to represent 600K and 1 atm.. 89

Figure 3-6: Calculated Kröger-Vink diagram for undoped monoclinic zirconia at 1200K........ 90

Figure 3-7: Calculated Kröger-Vink diagram for undoped monoclinic zirconia at 600K........ 91

Figure 3-8: Scaling of the relaxed defect formation energy energies. The fitting is according to equation (3-13) using the four points that have no correction. 93

Figure 3-9: Comparison between the calculated formation energy per O_2 for some transition metal oxides and the corresponding formation enthalpies. The latter are adapted from Ref. [94, 137]. The best fit for the computed formation energies is shifted by 1.22 eV from the line that corresponds to the perfect agreement with the experimental enthalpies. 96

Figure 4-1: Two tetragonal zirconia conventional cells projected on the (001) plane are depicted with their boundaries shown in continuous white line. One primitive cell (projected on the same plane) is also shown with its boundary in dashed blue. The crystallographic directions on the right belong to the conventional cell. Both cells share the [001] vector. Green (small) balls represent zirconium ions and red (large) balls represent oxygen ions. The chemical formula of the conventional cell is (Zr_4O_8), while that for the primitive cell is (Zr_2O_4). 100

Figure 4-2: (a) and (b) are reproduction of the previously calculated concentrations of electronic and ionic defects at 1500 K and 2000K from chapter 3. Zirconium interstitials are not shown for clarity. Ionic defects are denoted by Kröger-Vink notation, while n_c an p_v denote conduction band electrons and valence band holes, respectively. (c) and (d) depict the calculated self-diffusivities for oxygen defects and the total oxygen self-diffusivity as a function of P_{O_2} at 1500 K and 2000 K. 104

Figure 4-3: (a) Isothermal oxygen self-diffusivities as a function of P_{O_2}. (b) Isobaric oxygen self-diffusivities as a function of 1/T. (c) Isothermal oxygen self-diffusivities as a function of the off-stoichiometry, x, in T-ZrO_{2-x}. (d) Constant off-stoichiometry oxygen self-diffusivities as a function of 1/T. The experimental data shown in (d), adapted from Ref. [30], are self-diffusivities obtained by scaling the measured tracer-diffusivities by the appropriate correlation factor (of about 0.69) determined in Ref. [30]. 106

Figure 4-4: The effective activation barrier, E_{eff} (blue circles), and effective prefactor, D_0 (red squares), for oxygen diffusion in T-ZrO_{2-x} as a function of (a) P_{O_2} ,and (b) x. 108

Figure 5-1: Comparison between the theoretical calculation of the reference chemical potential of the O2 molecule using the statistical mechanical formulation of ideal di-atomic molecules and the tabulated values from thermochemical tables [94]. 113

Figure 5-2: The calculated temperature-oxygen partial pressure phase diagram for ZrO_2. 115

Figure 6-1: Representative hydrogen defect structures. Interstitial mono-hydrogen: (a) forming a <111> dumbbell with lattice oxygen, (b) in a <001> crowdion site between two lattice oxygens, and (c) in a bond center site. Hydrogen molecule: (d) substituting a lattice oxygen and oriented in <110>, and (e) in an interstitial octahedral site and oriented in <001>. Green (large), red (medium), and white (small) balls represent zirconium, oxygen, and hydrogen, respectively. The sticks are guide for the eye and have no physical significance 120

Figure 6-2: The formation energy of hydrogen defects in (a) oxygen poor conditions, (b) oxygen rich conditions. Solid, dashed, dot-dashed lines indicate oxygen-related, interstitial, zirconium-related defects, respectively. The shading indicates the range of the chemical potential of electrons accessible by self-doping due to the native defects as determined in chapter 3 127

Figure 6-3: The formation energy of hydrogen defect complexes with a zirconium vacancy including the two special clusters that contain 3H and 4H in (a) oxygen poor conditions and (b) oxygen rich conditions. The formation energy of the zirconium vacancy is included for comparison. The shading indicates the range of the chemical potential of electrons accessible by self-doping due to the native defects as determined in chapter 3. 130

Figure 6-4: The minimum energy structures for the thermodynamically stable interstitial hydrogen defects together with an isosurface for the net spin density (if nonzero). (a) $H_i^\bullet$, (b) H_i^x, (c) H_i', (d) $(H_2)_i^x$, and (e) $(H_2)_i'$. The yellow isosurface is taken at 0.01 Å^{-3}. 133

Figure 6-5: The minimum energy structures for the thermodynamically stable hydrogen-oxygen vacancy complexes together with an isosurface for the net spin density (if nonzero). (a) $H_O^\bullet$, (b)

H_O^x, (c) H_O', (d) $(2H)_O^\bullet$, (e) $(2H)_O^x$, and (f) $(2H)_O'$. The yellow isosurface is taken at 0.01 Å^{-3}. 137

Figure 6-6: The minimum energy structures for the thermodynamically stable hydrogen-zirconium vacancy complexes together with an isosurface for the net spin density (if nonzero). (a) H_{Zr}'''', (b) $(2H)_{Zr}^x$, (c) $(2H)_{Zr}'$, (d) $(2H)_{Zr}''$, and (e) $(H_2)_{Zr}''''$. The yellow isosurface is taken at 0.01 Å^{-3}. 139

Figure 6-7: The relaxed structures of the clusters (a) $(3H)_{Zr}'$, and (b) $(4H)_{Zr}^x$. 141

Figure 6-8: The formation energy of $H_i^\bullet$, H_i', $H_O^\bullet$, and $(H_2)_{Zr}''''$ obtained without correction and with the MP correction. The fitting was performed on the uncorrected results to obtain reference values. 143

Figure 7-1: Schematic shows the simulation cell of the (101) grains (left) and the (001) grains (right). The box indicates the actual size of the DFT supercell and was doubled in z-axis for clear visualization. Green and red balls represent zirconium and oxygen, respectively. 149

Figure 7-2: (left) The stress-strain response of the (101) and (001) grains under biaxial compression. (right) The change of the energy of the ZrO_2 chemical formula in biaxially compressed (001) and (101) grains with respect to the energy at the zero strain state. 150

Figure 7-3: The relative formation energies of the predominant hydrogen and native defects with respect to the zero strain state. [Top] is the results of the (101) grains, [bottom] is the results of the (001) grains. [Left] is the defects that predominate in oxygen poor conditions, [right] is the defects that predominate in oxygen rich conditions. 151

Figure 7-4: The stress-strain response for defect-free T-ZrO_2 and for T-ZrO_2 with hydrogen and native defects. [Top] is the results of the (101) grains, [bottom] is the results of the (001) grains. [Left] is the defects that predominate in oxygen poor conditions, [right] is the defects that predominate in oxygen rich conditions. 152

Figure 8-1: The effect of alloying elements on hydrogen pickup percentage [8]. 156

Figure 8-2: Schematics show the elementary processes that can take place at the oxide/water interface. 157

Figure 8-3: Calculated Kröger-Vink diagram for hydrogen doped monoclinic zirconia at 600K. 163

Figure 8-4: The ratio between hydrogen solubility in the transition metal doped monoclinic zirconia to the hydrogen solubility in the pure zirconia. These values were obtained from the calculated Kröger-Vink diagrams at 600 K and oxygen partial pressure of 1 atm. 164

Figure 8-5: The chemical potential of electrons in the monoclinic zirconia co-doped with hydrogen and a transition metal element. The horizontal blue line shows the value of the chemical potential of electrons in pure zirconia. These values were obtained from the calculated Kröger-Vink diagrams at 600 K and oxygen partial pressure of 1 atm. 165

Figure 8-6: The zero kelvin formation energy of interstitial hydrogen as a function of the chemical potential of electrons. The defect is stable in two charge states; proton (+) and hydride ion (-). 165

Figure 8-7: Schematic showing the thermodynamic barrier to transfer a free electron from the surface of the oxide to an adsorbed proton. 166

List of Tables

Table 2-1: Comparison of the diffusion coefficients for corrosion-critical species in zirconia at 500 K from Ref. [21]. The data for H and H$^+$ are collected from zirconia scale on zircaloy. Zr^{4+} and O^{2-} diffusivities are taken from yttria doped zirconia. 27

Table 2-2: Oxygen vacancy formation energy in tetragonal zirconia from Ref. [26] 29

Table 2-3: Diffusion barriers in eV for vacancies in tetragonal zirconia along [110] and [001] directions [26]. 30

Table 2-4: Compilation of the measured stress in the zirconia scale grown on zirconium and its alloys adapted from Ref. [51]. 45

Table 3-1: Formation energies in eV of several isolated defects in tetragonal ZrO_2. These values are at zero chemical potential of electrons. 77

Table 3-2: The details of the supercells used to perform finite size scaling on the native defects of tetragonal zirconia. 92

Table 3-3: Summary of the values of the formation energies of the defects at zero chemical potential of electrons 94

Table 3-4: Crystal and magnetic structure for the oxides used in evaluating the oxygen overbinding. 95

Table 4-1: The Multiplicities ζ_k and projections λ_k for the diffusive jumps in T-ZrO_2. We report λ_k in units of the lattice constants of the conventional unit cell (a=b=5.153 Å, c=5.303 Å). 100

Table 4-2: The calculated migration energy barriers (in eV) of oxygen defects in T-ZrO_2. The crystallographic directions and the jump distances are based on the perfect conventional unit cell. DFT results from Ref. [26] are shown for comparison. For V_O^x, barriers based on both the triplet (net spin $2\mu_B$), and the singlet ($0\mu_B$) saddle points are shown. 103

Table 5-1: Comparison between the theoretical calculations and the experimental determination of the thermodynamic transition temperature between the monoclinic and tetragonal phases. . 114

Table 6-1: The chemical potential of all the species in the two limiting extremes considered in this work. Also shown the DFT energies of the reference states that sets the bounds on the chemical potentials. All energies are in eV. 123

Table 6-2: The binding energy of the thermodynamically stable hydrogen defect complexes. . 131

Table 6-3: Calculated properties for the interstitial hydrogen defects. Bader charges are shown for hydrogen only. The distance, d, is the bond length of H_2 or OH$^-$ if either of them was detected in the simulation cell. The frequency difference, $\Delta\omega$, is defined in section 6.2.3 133

Table 6-4: Calculated properties for the hydrogen oxygen vacancy complexes. Bader charges are shown for hydrogen only. The distance, d, is between two hydrogen species and does not correspond to a bond length. 137

Table 6-5: Calculated properties for hydrogen-zirconium vacancy complexes. Bader charges are shown for hydrogen only. The distance, d, is the bond length of H_2 or OH^- if either of them was detected in the simulation cell. The frequency difference, $\Delta\omega$, is defined in section 6.2.3. 140

Table 6-6: Calculated properties for the two special clusters formed between hydrogen and the zirconium vacancy. Bader charges are shown for hydrogen only. The distance, d, is the bond length of the OH^- detected in the defect. The frequency difference, $\Delta\omega$, is defined in section 6.2.3 141

Table 6-7: The details of the supercells used to perform the finite size scaling on selected hydrogen defects in tetragonal zirconia. 142

Table 6-8: Summary of the values of the formation energies of the defects on which the finite size scaling was performed. These values are at zero chemical potential of electrons and in oxygen rich conditions. Also shown the (+/-) thermodynamic transition level for the interstitial hydrogen. All energies are in eV. 144

Table 8-1: The maximum oxidation state of the 3d transition metals considered in the modeling. 159

Table 8-2: The transition metal oxides that were used as reference states to compute the chemical potential of the transition metal. 161

Table 8-3: Summary of the electrons that were treated as valence electrons for the transition metals. 162

Chapter 1 : Motivation and thesis contribution

1.1 Motivation

The *engineering* motivation to pursue the work presented in this thesis is the need to develop predictive understanding of two degradation mechanisms which zirconium alloys, and in particular zircaloy-4, experience in the nuclear reactors. These mechanisms are metal corrosion and hydrogen pickup. Figure 1-1 schematically depicts these two degradation mechanism attacking a zirconium alloy in a nuclear reactor. The need to fundamentally understand these two processes stems from the fact that these alloys are currently pushed to withstand more demanding operation regimes in the nuclear reactor. Thus it is crucial to predict the performance of zirconium alloys under these demanding conditions to ensure a safe generation of the nuclear power. Traditionally experimentation and macro-scale modeling were the tools that the nuclear industry employed in order to design, model and simulate zirconium alloys response to the above mentioned degradation mechanisms. However, several important questions that lie at the heart of understanding the corrosion and hydrogen pickup of zirconium alloys remain unanswered[*] and so were typically circumvented through empiricism. This approach is not very desirable and there is a strong motivation (especially after the infamous Fukushima accident) to replace it with the robust fundamental understanding on the level of atoms and electrons. This sets the *engineering goal* of this thesis; that is to provide a fundamental understanding for few selected processes underlying the complex phenomena of corrosion and hydrogen pickup. These selected processes are to be discussed in the subsequent section on the thesis contribution.

---

[*] Confer chapter 2 for detailed account of these unanswered questions.

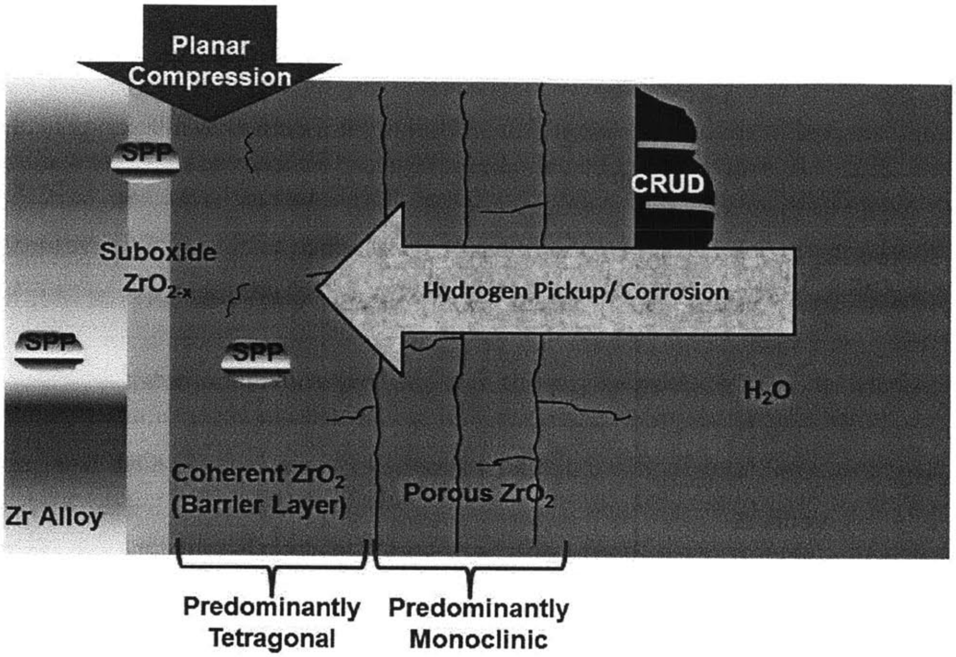

Figure 1-1: Schematic of the zirconium oxide passive layer that grows natively on zirconium alloys. SPP denotes the metallic secondary phase particles (alloying elements).

The engineering motivation we discussed above furnishes the ground for a deeper *scientific motivation*. It turns out that the medium through which the corrosion and hydrogen pickup take place is an electrically insulating layer of zirconium oxide (ZrO_2) that grows natively on zirconium alloys. Furthermore, the major players that control the thermodynamics and kinetics of metal corrosion and hydrogen pickup are the point defects of this oxide. In the nuclear reactor environment this oxide layer is exposed to a gradient of thermodynamic variables; these are the temperature, the oxygen chemical potential, and the mechanical stress. Thus, the engineering problem of understanding and predicting the corrosion and hydrogen pickup of zirconium alloys has a *scientific incarnation* which is the understanding and prediction of point defect equilibria in a metal oxide (in particular ZrO_2) under the effect of the thermodynamic forces mentioned above. The *scientific goal* of this thesis is to develop a framework to predict and understand charged defect equilibria in an insulating metal oxide and apply this framework to problems of relevance to the corrosion and hydrogen pickup of zirconium alloys. The scientific tool utilized to develop this framework is atomistic simulation using density functional theory combined with the general principles of statistical thermodynamics.

1.2 Thesis contribution

The theory of charged defects equilibria in a material with a band gap was analyzed in 1930's by Wagner and Schottky [1]. However expanding it to its full power and making useful predications out of it was accomplished in 1950's by Kröger and Vink [2]. At that time the whole theory relied on classical thermodynamic notions and utilized the concept of reaction constants† which can be determined experimentally. The fact that this theory requires an input from experiments and for almost all materials it needs an assumption‡ about the type of the underlying defects confined it its applicability to the experimental side of materials science and semiconductor physics. More recently with the advances in electronic structure theory and in the computational power, the interest in the *theoretical and predictive* understanding of charged defects emerged again especially in semiconductor physics. But this time the theory relied on statistical mechanical notions and predictions from electronic structure calculations without prior assumptions about the type of the defects. The problem is that these theoretical predictions did not account for the finite temperature effects and was presented in the form of formation energies, which make them hard to compare with experiments. Van de Walle and Neugebauer pointed out that there is equivalence between the old theory (Kröger and Vink approach) and the modern one and asserted that, in principle, one can construct the Kröger-Vink formulation starting from the modern theory of charged defects [3]. There were recent successful attempts, prior to my work, to demonstrate this equivalence and to construct the "more useful" Kröger-Vink formulation starting from electronic structure calculations [4-6]. The missing ingredient was still the account for finite temperature effects and, in my opinion, to take full advantage of the ability to predict charged defect equilibria. *Here comes the contribution of my thesis to this field.*

A framework was developed to predict the equilibria of charged defects in the limit of non-interacting defects in a material with a band gap. The framework is informed by density functional theory calculations and takes into account the finite temperature effects, in particular the phonon and electronic entropy contribution to the defect free energy of formation. The framework naturally produces the Kröger-Vink diagram of the defect equilibria which is directly

---

† These constant are related to the mass action law.

‡ Or at least a hint from experiments.

comparable to electric conductivity measurements. We applied this approach to both the tetragonal and monoclinic phases of ZrO_2 and could reproduce some of the experimental findings about their defect equilibria (without any prior assumptions). In addition, in certain thermodynamic conditions, where experiments had fallen short in resolving the nature of the predominant defect, the developed approach was able to resolve the controversy. As I stated above, I believe that the ability to predict and understand the equilibria of charged point defects has not been fully taken advantage of. In this thesis I demonstrate some of the immediate applications of this framework which address important questions related to the corrosion and hydrogen pickup of zirconium alloys. Here is a summary of these applications classified according to the engineering problem they address:

1) Corrosion related applications
    a) The predicted defect concentrations in tetragonal zirconia were combined with the migration barriers of the oxygen-related defects. We evaluated the latter utilizing the so-called nudged elastic band method [7]. The outcome was a prediction of the self-diffusion coefficient of oxygen in tetragonal zirconia in a wide range of thermodynamic conditions. On the engineering level, this computation provides a necessary input to model the growth of the oxide scale on zirconium alloys as a function of oxygen chemical potential. Scientifically, we performed a careful analysis for the predicted isobaric and constant off-stoichiometry self-diffusivities and showed that this approach predicts a spectrum of the activation barriers of self-diffusion depending on the thermodynamic conditions. This predicted spectrum provides one way to reconcile the scatter in the experimentally determined activation barriers for self-diffusion in metal oxides.
    b) Utilizing the predicted defect concentrations in both the monoclinic and tetragonal phases of ZrO_2, we constructed for the first time starting from first principles a temperature-oxygen partial pressure phase diagram for ZrO_2. This phase diagram, analogous to an Ellingham diagram, explains the role of point defects in stabilizing the tetragonal phase at temperatures lower than the atmospheric-pressure transition temperature. In relation to the corrosion of zirconium alloys, this work provides another perspective for the reason of stabilizing the tetragonal

phase at the metal/oxide interface in the nuclear reactor temperature although the monoclinic is supposed to be the thermodynamically favorable phase at this temperature. Scientifically, we showed that point defects through their configurational entropy can thermodynamically stabilize a phase below its stoichiometric stability temperature. This fact, while known experimentally and is widely used to extract metals from their ores, has not been demonstrated previously starting from first principles.

2) Hydrogen pickup related applications

    a) We applied the developed framework to model doping and co-doping in monoclinic zirconia. The motivation was an experimental observation from 1960's [8] that hydrogen pickup of zirconium alloys exhibits a volcano-like relationship when plotted against the first raw of transition metals that are used to alloy zirconium. The phenomenon has important implication in designing these alloys. In particular the peak of the volcano was found coincident with nickel and hence the latter was excluded from the design of zircaloy-4. The volcano has not been explained since then. We computed the Kröger-Vink diagram of monoclinic zirconia co-doped with hydrogen and a transition metal and provided an explanation for the volcano based on the extent to which the transition metal facilitate the solubility of hydrogen in the zirconium oxide. Deeper analysis showed that the transition metal that is able to lower the chemical potential of electrons as much as possible, is the one that lowers the formation energy of interstitial protons in the oxide and hence cause the undesirable hydrogen pickup. The same conditions also lead to inhibition of hydrogen gas evolution on the surface because of higher charge transfer barrier. This explanation equipped with the modeling approach we developed can provide a scientific basis to design hydrogen pickup resistant alloys. But even on a broader level, the fact that our approach is able to trace the chemical potential of electrons (Fermi level) as a function of doping and the thermodynamic conditions; it can have an impact on other fields such as catalysis, fuel cells and water splitting.

b) We examined the interplay between hydrogen defects in tetragonal zirconia and the planar stress that this phase experiences in the oxide scales grown on zirconium alloys. An interesting feedback loop was identified that shows that the stress can enhance the abundance of certain hydrogen defects, while these very defects tend to relax the stress. The outcome would be destabilization of the tetragonal phase of zirconia, possible initiation of cracks in the oxide due to volume change during tetragonal to monoclinic transition, and direct exposure of the underlying metal to hydrogen. This work provides a possible explanation for the mechanism through which hydrogen can get into zirconium alloys. Although in this work we did not propagate the zero kelvin results to finite temperature, it is possible to perform this in future work to show for the first time how stress (particularly non-hydrostatic) can impact the Kröger-Vink diagram of the defect equilibria.

1.3 Thesis organization

The thesis is divided into four components. **The first** is a literature review of the phenomenological observations related to the corrosion and hydrogen pickup of the zirconium alloy, zircaloy-4. This component is presented in chapter 3. **The second** component is concerned with the development of the framework to predict charged defect equilibria in a metal oxide and its application on the tetragonal and monoclinic phases of zirconia. This component is in chapter 3. **The third** component is related to the application of the developed framework to study corrosion-related phenomena and this can be found in chapter 4 on oxygen self-diffusion in tetragonal zirconia and in chapter 5 on the role of defects in the thermodynamics of the tetragonal-monoclinic phase transition in zirconia. **The last** component is related to hydrogen pickup and can be found in chapters 6, 7, and 8. Chapter 6 is a thorough analysis of the hydrogen defects in tetragonal zirconia, while chapter 7 is an examination of the interplay between these hydrogen defects and the planar stress applied to tetragonal zirconia. In chapter 8 we provide an explanation for the volcano of the hydrogen pickup based on analysis of co-doping monoclinic zirconia with hydrogen and a transition metal utilizing the approach developed in chapter 3. Finally we conclude the thesis in chapter 9 by a summary and outlook.

Chapter 2 : Literature review of waterside corrosion and hydrogen pickup of zircaloy-4

Zirconium alloys are the major structural materials employed within the fuelled region of all water cooled nuclear reactors [9, 10]. In particular Zircaloy-4 is currently in use as a fuel cladding in Pressurized Water Reactors (PWR). There is a substantial need to understand the mechanisms of the processes that degrade zirconium alloys in order to achieve higher fuel burnup and push these alloys to operation regimes where the currently used empirical models are of no predictive help.

The objective of this chapter is to review the current state of knowledge on the physical and chemical phenomena relevant to the corrosion and hydrogen pickup of Zircaloy-4 in pressurized water reactors (PWR). These are two of the most challenging degradation processes of zirconium alloys in nuclear reactors. The topic has been comprehensively reviewed in 1998 in a technical document produced by IAEA[11] and more recently in 2005 in a review paper [10] by Brian Cox. This chapter expands these excellent reviews to include the more recent literature. We also include our perspective and interpretation of the state of knowledge reported in literature, especially the contradictions on the governing unit processes in the corrosion of zirconium alloys and the factors that accelerate it.

The organization of the rest of the chapter is as follows. **First**, we discuss corrosion kinetics. In particular we discuss the electrochemical reactions that govern corrosion kinetics; the transport of oxygen, zirconium cations, and electrons in the passive oxide film and the microstructure of that film. We end this part by a summary of the controversy in literature on the origin of the transitions in the corrosion kinetics of zirconium alloys. **Second,** we examine the processes that accelerate the kinetics of zirconium alloys. These processes include: Li absorption, radiation effects, secondary phase precipitates, and CRUD-induced localized corrosion. **Finally** we discuss the current knowledge of the mechanism of hydrogen pickup and the interplay between corrosion kinetics and hydrogen pickup kinetics.

2.1 Water Side Oxidation of Zircaloy-4

In this section, we provide a description of the corrosion kinetics, the corrosion reaction as an electrochemical process, the transport processes through the oxide scale, taking into account the diffusion of point defects and their diffusion pathways, and finally the effects of the microstructure of the oxide scale on corrosion kinetics.

2.1.1 Corrosion Kinetics

The initial stage of protective zirconium alloys oxidation (including zircaloy-4) follows a cubic law up to an oxide thickness of about 2 micron [10, 12]. This stage is commonly termed the "pre-transition" stage. Such a cubic growth law is not in accordance with what one would expect on the basis of diffusion controlled oxidation[§] or a surface reaction controlled oxidation[**]. Beyond the first 2 microns, the oxide growth undergoes a transition to obey a series of cubic cycles. The duration of each of these cycles decreases with time and is less than the pre-transition cycle duration. This regime of oxide growth is typically termed "post-transition" and is well-approximated by a linear law that encompasses the underlying short cubic cycles [10-12]. Figure 2-1 from Ref. [12] schematically shows the overall oxide growth. The possible origin of the transition from the cubic law to the linear one is discussed in section 2.1.4.5 below.

[§] This would lead to a parabolic law.

[**] This would lead to a linear law.

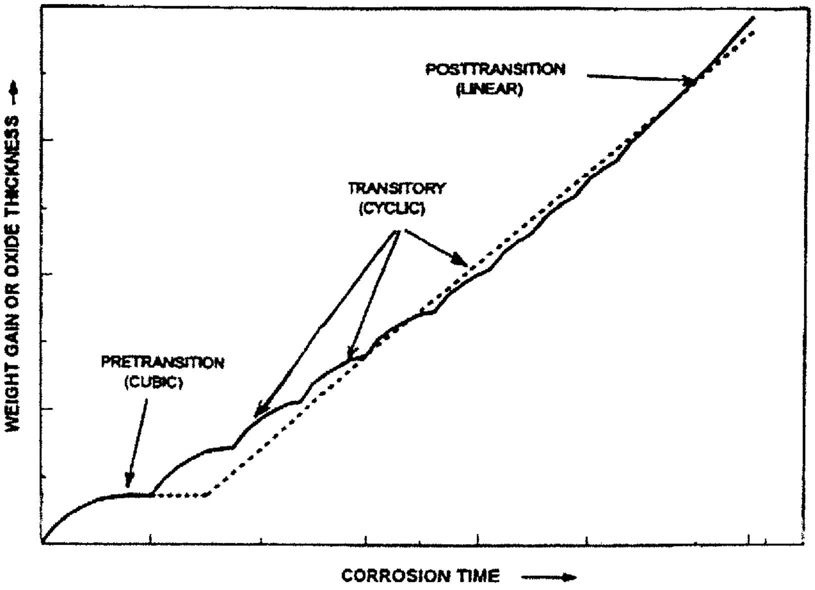

Figure 2-1: Schematic of zirconium oxidation quantified in terms of weight gain vs. time [12].

2.1.2 Zircaloy-4 oxidation as an electrochemical process

The overall waterside corrosion reaction is

$$Zr + 2H_2O \rightarrow ZrO_2 + 4H \qquad (2\text{-}1)$$

This reaction can be divided into several steps. However, there is no agreement in the literature about this break down. We report here one of the proposed reaction steps by Billot et al. [13] using Kröger-Vink notation.

1. Dissociative water adsorption at the oxide/water interface with the aid of an oxygen vacancy.

$$H_2O + V_O^{\bullet\bullet} + O_O^{\times} \rightarrow 2OH_O^{\bullet} \qquad (2\text{-}2)$$

2. Oxygen and part of the hydrogen diffuse to the grain boundaries.

3. Oxygen dissolution into the interstitial sites of the metal to form solid solution (Zr,O).

$$\begin{aligned} e' + OH^{\bullet} &\rightarrow O_O^{\times} + H_i^{\times} \\ O_O^{\times} &\rightarrow V_O^{\bullet\bullet} + O_{i(metal)}^{\times} + 2e' \end{aligned} \qquad (2\text{-}3)$$

4. Zirconium oxide (zirconia) production

$$Zr^{\times}_{Zr(metal)} + 2O^{\times}_{i(metal)} \rightarrow Zr^{\times}_{Zr} + 2O^{\times}_{O} \qquad (2\text{-}4)$$

The part of hydrogen produced by the corrosion reaction and managed to diffuse through the oxide layer, reaches the metal and remains in solution in the metal until the solubility limit is exceeded at which point zirconium hydrides precipitate. The other part of hydrogen may recombine and form hydrogen molecules that remains dissolved in water. However, there are several important mechanistic details that are not known. First, it is not known whether the proton that was produced in the corrosion reaction diffuses into the oxide layer in a correlated fashion with the oxygen ion to which it binds as a hydroxyl unit or it diffuses independently [14, 15]. Second, where does the recombination of the proton and electron to form a neutral hydrogen atom take place? And how long does the proton diffuse in the oxide layer before it discharges to become a neutral species in order to enter the metal? Third, how is it possible for the electrons to transport in a good insulator material such as zirconia to meet the protons? In the next section we examine the transport processes that take place through the zirconia layer which govern the growth kinetics.

2.1.3 Transport processes through the oxide layer

The continuous growth of the oxide layer on zircaloy-4 according to the general corrosion reaction described in the previous section is achieved by the transport of the charge carriers through this oxide layer starting from the oxide/water interface to the metal/oxide interface and vice versa. In general, the oxide growth on zirconium and its alloys is known to proceed by inward oxygen transport from the oxide/water interface to the metal/oxide interface [16, 17] while it was indicated by diffusion measurements [18, 19] that zirconium is not mobile through its oxide until very high temperatures in the range of the loss of coolant accident (LOCA). This general picture of the transport dictates that charge neutrality across the oxide has to be maintained by electron transport through the oxide from the metal/oxide interface to the oxide/water interface in a direction opposing that of the diffusion of oxygen. The latter process is known to be very slow as zirconia is a very good insulator [20] and hence it was suggested by

Cox [10] that electron transport through zirconia is the rate limiting process for the corrosion reaction of zirconium and its alloys.

The above described picture is definitely very general and lacks the mechanistic details about the nature of the diffusing species and their diffusion pathways. The mechanistic details are essential in providing the underpinnings of a predictive physics-based corrosion model. Furthermore, while hydrogen diffusion in the oxide is not necessary for the completion of the corrosion reaction, this process is inevitable and needs to be understood for two good reasons. The first is that hydrogen presence in zirconia has an effect on the corrosion kinetics as described in the hydrogen pick up section below. The second is that hydrogen diffusion through zriconia is followed subsequently by hydride precipitation in zirconium metal which has detrimental embrittlement effects. Thus, there is a need to understand the mechanistic and quantitative aspects of the transport of the corrosion related species in zirconia, including the electronic, cationic, oxygen and hydrogen related defects. In the rest of this section we review what is known about these transport processes in the literature. Before delving into the details, we present in Table 2-1 an example set of data (collected by Delgueldre et al. [21]) to provide an order-of-magnitude comparison of diffusivities concerning various species in zirconia at 500 K.

Table 2-1: Comparison of the diffusion coefficients for corrosion-critical species in zirconia at 500 K from Ref. [21]. The data for H and H^+ are collected from zirconia scale on zircaloy. Zr^{4+} and O^{2-} diffusivities are taken from yttria doped zirconia.

Species	Diffusivity (m^2s^{-1})
Zr^{4+}	10^{-20}
O^{2-}	10^{-12}
H	10^{-16}
H^+	10^{-12}

It is known that in atmospheric pressure there are three phases of zirconia; cubic, tetragonal and monoclinic as shown in Figure 2-2. The latter is the stable phase up to ~1170 ^0C [22]. The oxide scale grown on zirconium alloys contains both the tetragonal and monoclinic phases. The tetragonal phase is usually stabilized by a compressive planar stress at the metal/oxide interface and/or by alloying elements that gets incorporated in the zirconia lattice [10].

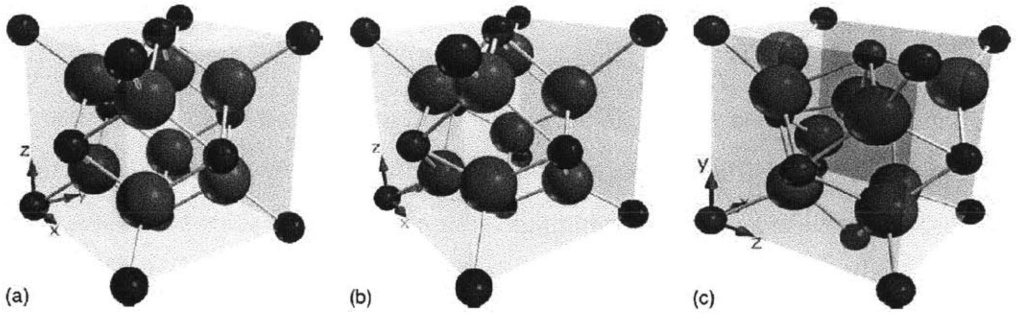

Figure 2-2: The conventional unit cells of atmospheric pressure phases of zirconia. (a) cubic, (b) tetragonal. (c) monoclinic. Zirconium ions are blue and oxygen ions are red. Figure is adapted from [23].

2.1.3.1 Oxygen transport

Oxygen transport takes place via point defects within the lattice, or via short circuit paths as dislocations, grain boundaries and the porosity that develops in the zirconia layer on zircaloy-4. We examine each of these four paths for oxygen diffusion in zirconia. Oxygen point defects form in various configurations in zirconia and they can all collectively contribute to the oxygen transport kinetics, and thus corrosion. Therefore it is important to determine the dominant oxygen defect species and their diffusion properties.

Oxygen point defects: In general there are three types of oxygen point defects that can be present in zirconia lattice; vacancies (V), interstitials (O_i) and antisites (O_{Zr}). Moreover, each of these types can be neutral or charged. One last further complication is that in monoclinic zirconia there are two crystallographic types of oxygen; three fold coordinated (O_3) and four-fold coordinated (O_4). In the case of charged defects, the charge tends to be localized on the defect and do not exhibit a bandlike character [24, 25]. Zheng et al. [24] performed comprehensive density functional theory calculations for the native point defects in monoclinic zirconia and hafnia and showed that the oxygen antisites are not thermodynamically favorable.

We are not aware of such a comprehensive study for the tetragonal phase (prior to our work presented in the next chapter). However, Eichler [26] employed density functional theory to compute the vacancy formation energy, E_f, at the valence band maximum of the perfect crystal of tetragonal zirconia and the results are summarized in Table 2-2. It was not clear which chemical potential was used as a reference in these calculations.

Table 2-2: Oxygen vacancy formation energy in tetragonal zirconia from Ref. [26]

Vacancy	E_f (eV)
$V_O^\times$	5.73
$V_O^\bullet$	2.69
$V_O^{\bullet\bullet}$	-0.76

Eichler also reported the dependence of the formation energy of the different charge states of the vacancy in zirconia as a function of the chemical potential of electrons (Fermi level ε_F). These results are shown in Figure 2-3. In the figure, the vacancy is denoted by F to express the fact that they it is actually an F-center.

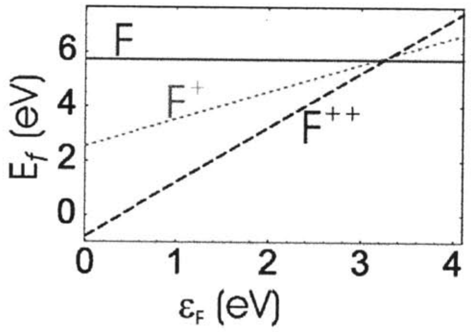

Figure 2-3: The formation energy of neutral, singly and doubly charged F-centers in zirconia as a function of the Fermi level [26].

Oxygen point defect diffusion pathways: The diffusion of oxygen species through zirconia lattice is an activated process that is achieved either by direct hopping from defect site to a nearby defect site or by some exchange mechanism in which more than one atom are involved [27]. Computing the energy barriers for such activated processes is possible through density functional theory and classical atomistic potentials. However, such evaluation for the energy barriers for the diffusion of oxygen species was not considered for the monoclinic phase of zirconia. For the tetragonal phase, only vacancy hopping was considered using density functional theory in two crystallographic directions [110] and [001] in Ref. [26] The computed energy barriers in eV are shown in Table 2-3 for the different stable charge states of the hopping vacancy.

Table 2-3: Diffusion barriers in eV for vacancies in tetragonal zirconia along [110] and [001] directions [26].

Direction	$V_O^{\times}$	$V_O^{\bullet\bullet}$
[110]	1.35	0.22
[001]	1.43	0.61

Similarly Safonov et al. employed ab initio embedded cluster calculations and found an energy barrier for the hopping of a neutral oxygen vacancy of 1.95 eV. The hopping direction was not specified in the reference [28]. The theoretical work on point defects in zirconia (and indeed on all metal oxides) always considered the formation energies of the defect in isolation from the migration barrier. Hence, the overall picture of self-diffusivity was never clearly depicted. In chapter 4 we show how this can be done and demonstrate it on the case of oxygen self-diffusion in tetragonal zirconia.

The diffusion coefficient of oxygen in zirconia was also measured experimentally. However, it should be noted, however, that in an experimental setup, the distinction between in-lattice diffusion, and diffusion through grain boundaries or any other form of extended defects (dislocations or three dimensional networks of interconnected pores) may not be possible. In such cases what is usually measured is an effective diffusion coefficient. Figure 2-4 taken from Ref. [18] summarizes the results of such measurements for oxygen diffusion in different types of zirconia at various temperatures. The collected data in this figure indicate an activation energy that ranges from 1.3 eV to 4.2 eV.

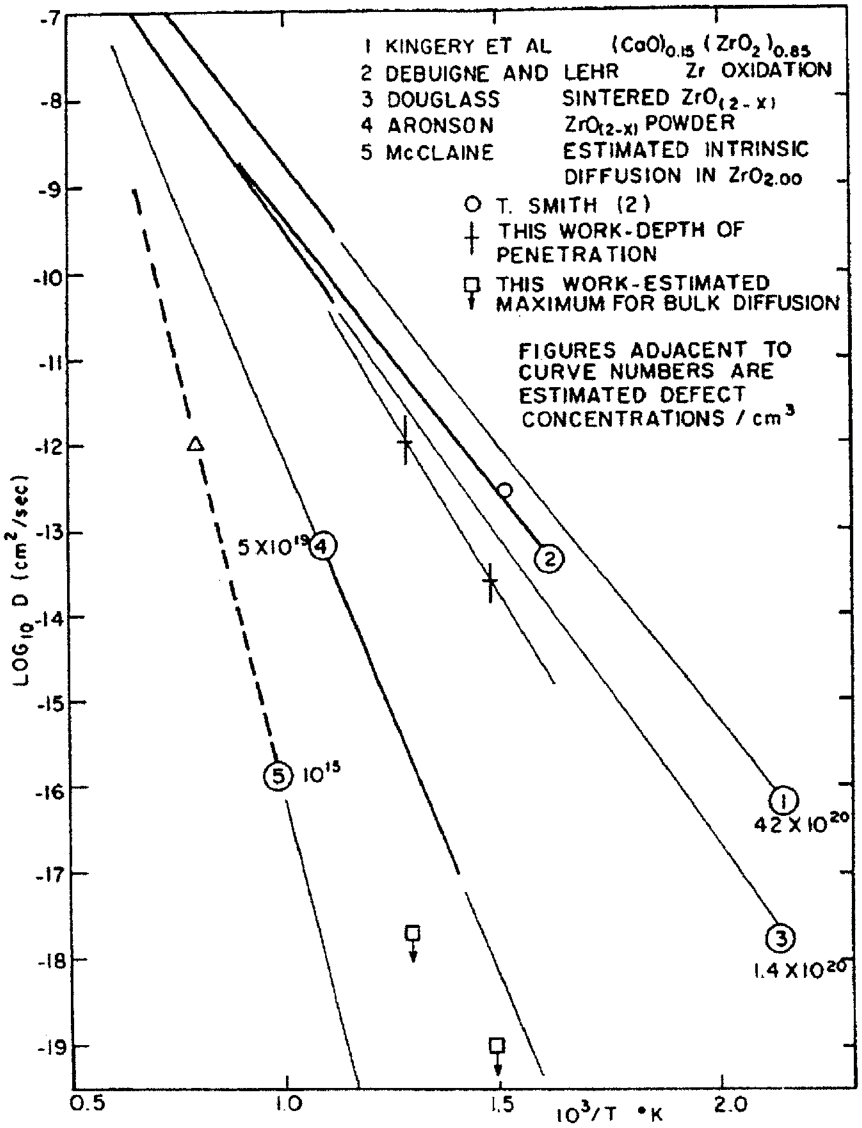

Figure 2-4: The diffusion coefficient of oxygen in various zirconia samples [18].

To distinguish between grain boundary diffusion and in-lattice (or in-crystallite) diffusion, Brossmann et al. used ^{18}O as a tracer and secondary ion mass spectroscopy profiling to measure the in-lattice and grain boundary oxygen diffusion in ultrafine grained monoclinic zirconia [29]. The grain boundaries considered in their study separate between nanocrystals of width 80-300 nm and the boundaries average width is ~ 0.5 nm. It was found that the grain boundary diffusion is 10^3-10^4 times faster than in-crystallite diffusion throughout a temperature range of 450 to 950 ^{0}C. The diffusivities were independent of the crystallite size in the range of

70-300 nm. The effective activation energies for grain boundary and in-lattice diffusion were 1.95 and 2.29 eV respectively. The authors of Ref. [29] suggest that the reduced oxygen diffusivity in pure zirconia indicate diffusion mechanism that involves both the thermal formation and migration of oxygen defects. On the other hand, the activation energy for the oxygen diffusion in a single crystal tetragonal zirconia was concluded to be 0.65 eV by Park and Olander based on oxygen tracer diffusion measurements [30]. Care should be taken when comparing these results with diffusion in the oxide scale grown on zircaly-4. The oxide scale as will be discussed in a subsequent section has what is commonly termed the sub-oxide region close to the metal/oxide interface. The chemistry and crystallography of this sub-oxide is expected to be different than zirconia. Furthermore, the large compressive planar stress that exists in actual oxide scales formed in a corrosion environment is not accounted for in such a clean experimental setup used in studying diffusion in zirconia.

It was proposed that the hydroxyl group (OH^-) can diffuse as an entity in zirconia [14]. However, Doung et al. using secondary ion mass spectroscopy found no evidence that OH^- ions are mobile species in tetragonal zirconia single crystals [31]. Since it is known that in many proton conductors, OH^- ion is rarely mobile, Chevalier et al. concluded that O^{2-} and H^+ species follow parallel but independent paths into zirconia lattice [15].

A high density of dislocations was observed in zircaloy-4 oxide scales obtained under pressurized water reactor conditions [32]. On the other hand, Otsuka et al. showed that dislocation enhances the ionic conductivity in Yttria-stabilized zirconia [33]. These two facts together led Angel to conclude that the presence of high compressive stress at the metal/oxide interface as well as irradiation can generate dislocations in the oxide scales formed on zircaloy-4 [16]. These dislocations serve as a fast migration path for oxygen species.

The generation of porosity on the oxide scale grown on zirconium and its alloys is inevitable [10]. The pores start to appear in the zirconia scales once the so-called post-transition regime of corrosion begins. Figure 2-5 from Ref. [34] shows the average radius of the pores in the oxide scale grown on zircaloy-4 as a function of the oxide thickness. Zhou et al. introduced a reasonable interpretation for the emergence of porosity in the zirconia scales as they grow which we present here [35]. The new layers of the oxide that form at the metal/oxide interface as zirconia are known to grow by the inward diffusion of oxygen ions. Due to the lattice mismatch between the oxide and the metal, the latter being smaller, the new layers of the oxide grow under compressive planar stress. This leads to the presence of various point and line defects within the crystallites of the grown oxide. With the continuous growth of the oxide, the older layers depart away from the metal and hence the compressive stress relaxes and with the action of temperature and time, the defects tend to migrate and get absorbed at the grain boundaries. The accumulation of the absorbed defects at the grain boundaries leads to the formation of these pores.

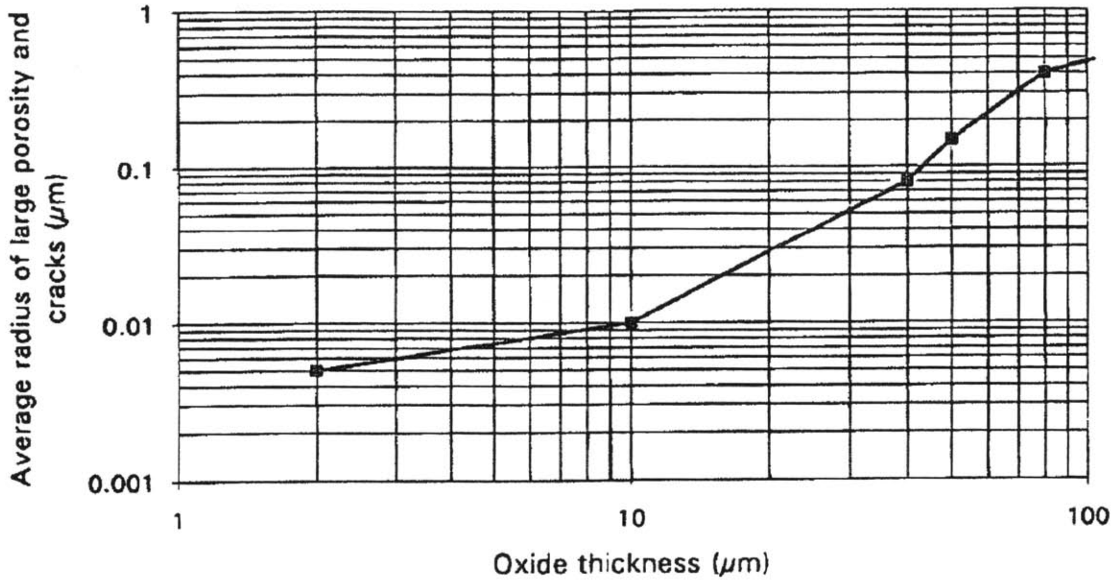

Figure 2-5: Average radius of the pores as a function of the oxide thickness evaluated by out-of-pile loop mercury measurements [34].

Regardless of the validity of this hypothesis by Zhou et al.; the generation of pores wide enough to allow the penetration of water molecules into the oxide layers, shortens the distance between the corrosion reaction products including oxygen species and the bottom of the oxide layers which is the metal/oxide interface. Not only the presence of the pores allows water diffusion, but also we expect the walls of these pores to be highly defective (at least based on the hypothesis described above) and hence the oxide/water part of the corrosion reaction gets enhanced. The origin of this enhancement is that energy barrier for water adsorption and dissociation is generally reduced in the presence of oxygen vacancies on the oxide surface [36]. In addition to this, Ramasubramanian et al. suggested that the dominant diffusion path for oxygen species in the presence of porosity will be along the walls of the pores [37]. Indeed there is an indirect support for this suggestion from the ab initio calculations in Ref. [28]. These calculations show that there is a migration pathway for the oxygen vacancy on the (001) surface of tetragonal zirconia which has an energy barrier of 1eV compared to 1.95 eV for the migration in the bulk of the crystal.

2.1.3.2 Zirconium transport

It is generally believed that zirconium cation is not mobile in its oxide at the reactor operation temperature [10, 11]. However, at elevated temperatures such as those during the course of a LOCA, the outward diffusion of zirconium from the metal/oxide interface can be significant. A classification of diffusion pathways similar to that of oxygen species can be assigned to zirconium. However, only data about the in-lattice diffusion of zirconium in zirconia is available and nothing can be said about the diffusion across or along the extended defects. Melikhova et al. showed by combining density functional theory and positron lifetime spectroscopy that zirconium vacancies exist natively in zirconia and that hydrogen can reduce their formation energies [38]. This effect of hydrogen in reducing the formation energies of zirconium vacancies in addition to another effect which is the reduction of the migration barrier for the zirconium vacancy was suggested and demonstrated experimentally[††] (see chapter 2 in Ref. [16] and the references therein.). Computer simulations using classical interatomic potential were used to show that the migration barrier of cations vacancies in the cubic phase of zirconia ranges between 3.1 and 5.8 eV [39]. The indicated numbers show that this type of diffusion is important only at high temperatures (LOCA conditions).

2.1.3.3 Electron transport

As we mentioned in the introduction to this section, it is assumed that charge neutrality through the oxide layer is achieved by electron transport from the metal/oxide interface toward the oxide/environment interface. However, since zirconia is an insulator, it is expected that this electronic transport process is slow and hence the rate limiting step. Additional support for the hypothesis that the electronic transport can be the rate limiting step is the fact that the measured potential on the metal in always negative [10] indicating that electron transport is the most

---

[††] In chapter 6 we show using density functional theory calculations that hydrogen tend to thermodynamically stable complexes with zirconium vacancies in tetragonal zirconia.

difficult process. Further support for this hypothesis comes from comparing the chemical diffusion coefficient in single crystal tetragonal zirconia with the chemical diffusion in zirconia formed on pure metal or zircaloy-4 during the course of corrosion reaction [30]. The comparison is shown in Figure 2-6 below. The three order-of-magnitude discrepancy between the tracer diffusion-based chemical diffusivity and the corrosion-based was attributed (among other reasons) to the possibility that zirconium oxidation kinetics is not controlled by anion diffusion. In other words, if the oxygen transport is as great as implied by the upper line in Figure 2-6 , the corrosion rate could be controlled instead by slow electron transport in the growing oxide film.

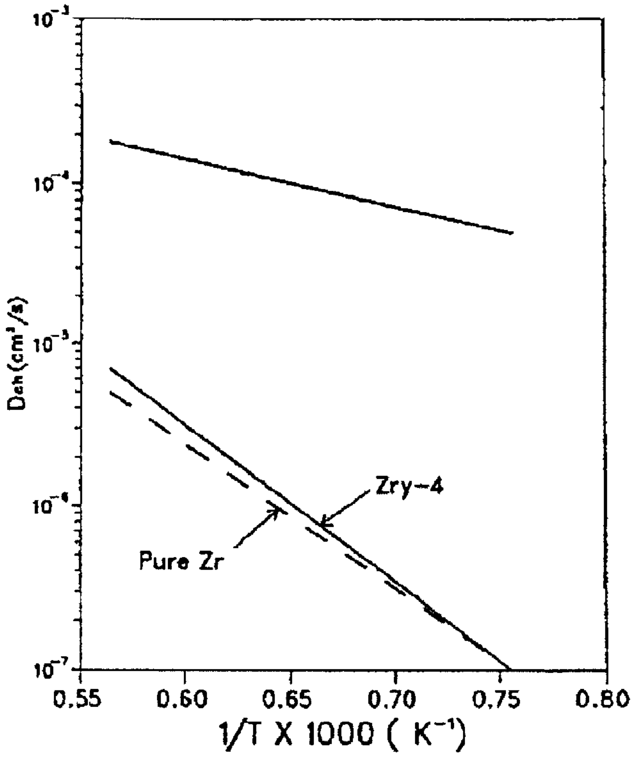

Figure 2-6: The total chemical diffusion coefficient in zirconia; the upper line is deduced from measured tracer diffusivities in single crystal tetragonal zirconia. The two lower lines are obtained from corrosion kinetic data. The figure is adapted from Ref. [30].

It is known that gamma irradiation enhances the electronic conductivity in zirconia [40]. Such enhancement can occur during the operation conditions in nuclear power plants. According to Ref. [40]; increased rates of adsorbed water dissociation on the surface of gamma irradiated zirconia were observed. This behavior was attributed to gamma-induced exciton formation within zirconia that has a band gap close to but slightly greater than the O-H bond dissociation energy. This behavior is pronounced in tetragonal zirconia compared to the monoclinic phase. It was shown using density functional theory calculations that the origin of this distinction between tetragonal and monoclinic phases is due to the fact that the exciton pair motion is not restricted in any direction in the former while it is limited only to the [010] direction in the later [41].

Additional electronic states can be introduced in the band gap of zirconia by impurities and dopants. Nishizaki et al. used first-principles molecular orbital calculations to show that hydrogen generates a new impurity states below the conduction band of zirconia which reduces its band gap [42]. Such impurity states enhance the electronic conductivity. A similar situation occurs when the secondary phase particles in the oxide dissolves and gets incorporated in the zirconia lattice. Such incorporation is associated with enhanced corrosion rates and degradation. On the other hand, if a secondary phase particle is still in the metallic state (unoxidized) and connects the zirconium metal with the oxide/water interface, it can act is a short circuit for electronic transport. However, such situation is relevant only for the early growing phase of the oxide scale after which it is improbable to find unoxidized secondary phase particle long enough to connect the metal with water.

2.1.4 Oxide phases, microstructure, stoichiometry and stresses

In this section we describe the phases that form in the passive zirconium oxide layer and the interrelationships between them and their effect on the protectiveness of the oxide. Second, we give a description of the microstructural features that arise in the passive zirconia layer. Third, we examine the stoichiometry of the oxide as a function of the distance from the metal/oxide interface to the oxide/water interface. Fourth, we discuss the stress state in the zirconia layer and its effect on the phases and the microstructural features that grow during the corrosion process. Finally we review te theories that attempt to explain the transition behavior in corrosion kinetics. This transition is the net effect of the microstructural, chemical features and the stress state in the oxide layer. Before discussing these points, we emphasize the following:

1. There is an uncertainty in the literature in terms of distinguishing between the "cause" and the "outcome". While that is common to most of the underlying processes of the corrosion of zircaloy-4, it is much more pronounced when it comes to characterizing

the oxide layer. In spite of that, it was possible recently to elucidate some of these dependencies and thus we focus more on these resolved aspects.

2. Cox emphasized in his review [10] that the experimental characterization of the oxide layers from corroded zirconium samples is difficult because of:
    a) Possible oxide cracking and zirconia phase transformation due to stress relaxation during sample preparation, which could confuse both the phase information and porosity measurements.
    b) The electrically insulating nature of zirconium oxide.

2.1.4.1 Oxide phases

In a wide range of low pressure and in a temperature range up to 1170 ^{0}C the monoclinic phase is the ground state phase of zirconia. However, stress, doping and the size of the grains of zirconia crystallites can stabilize phases other than the monoclinic.

In the bottom layer of the oxide film, which is in close vicinity to the metal matrix, monoclinic, tetragonal, cubic, metal-oxygen solid solution and amorphous phases can be detected [10, 35, 43]. The tetragonal and cubic phases can be stabilized at this interface in part due to the large compressive stresses due to the lattice mismatch between the metal and the oxide. The hypothetical pressure-temperature (P-T) phase diagram for zirconia [44] shown in Figure 2-7 suggests that a high stresses the tetragonal phase can be stabilized at reactor operation temperature. This phase diagram, however, cannot explain the presence of the cubic phase. Bouvier et al. showed that if the zirconia crystallite sizes are smaller than 30 nm, which is the case for the oxide scale on zircaloy-4, the monoclinic-tetragonal equilibrium line in the P-T diagram is strongly downshifted in temperature [45]. In addition they found that the tetragonal phase obtained in high temperature under high pressure can be quenched to room temperature, if the pressure is maintained, and it is destabilized and transforms completely to monoclinic if the pressure is released. These observations may provide an interpretation for the presence of the cubic phase, if we assume that the tetragonal-cubic equilibrium line in the P-T will follow the monoclinic-tetragonal line downshift in the P-T diagram when the crystallite sizes are small.

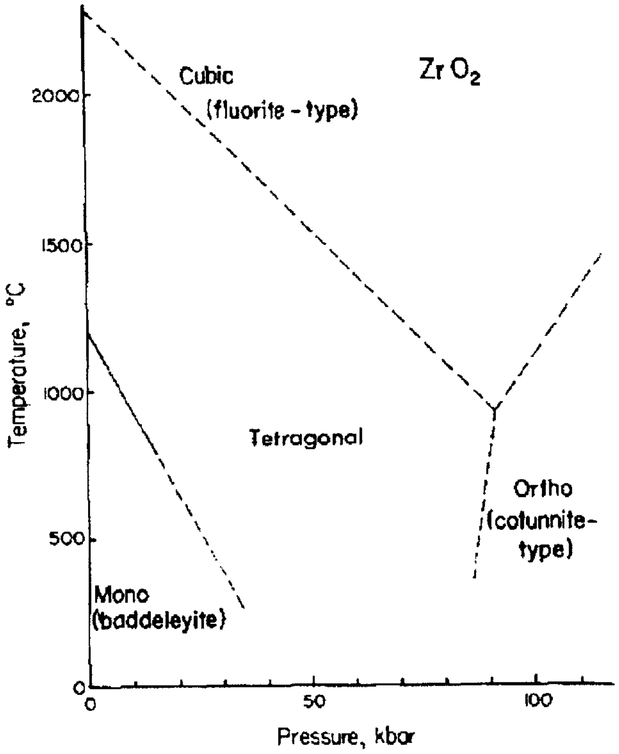

Figure 2-7: Hypothetical pressure-temperature phase diagram for zirconia [44].

The presence of an oxygen-zirconium interstitial solid solution at the metal/oxide interface is expected as oxygen has a strong affinity to dissolve in zirconium as shown in the phase diagram in Figure 2-8. In particular at 200 ^{0}C, about 28.6 atomic percent oxygen can dissolve in zirconium and the solubility increases with increasing temperature.

The presence of an amorphous zirconia phase at the metal/oxide interface is also expected because of the nature of growth of this scale. In other words, each new layer of zircnoia grows at the metal oxide/interface and since it is not possible kinetically to form the whole layer at once in its full crystalline structure, intermediate amorphous structures have to appear as a precursor before crystallization. This idea is supported by molecular dynamics simulation of the oxidation of Zr (0001) surface in oxygen gas [46].

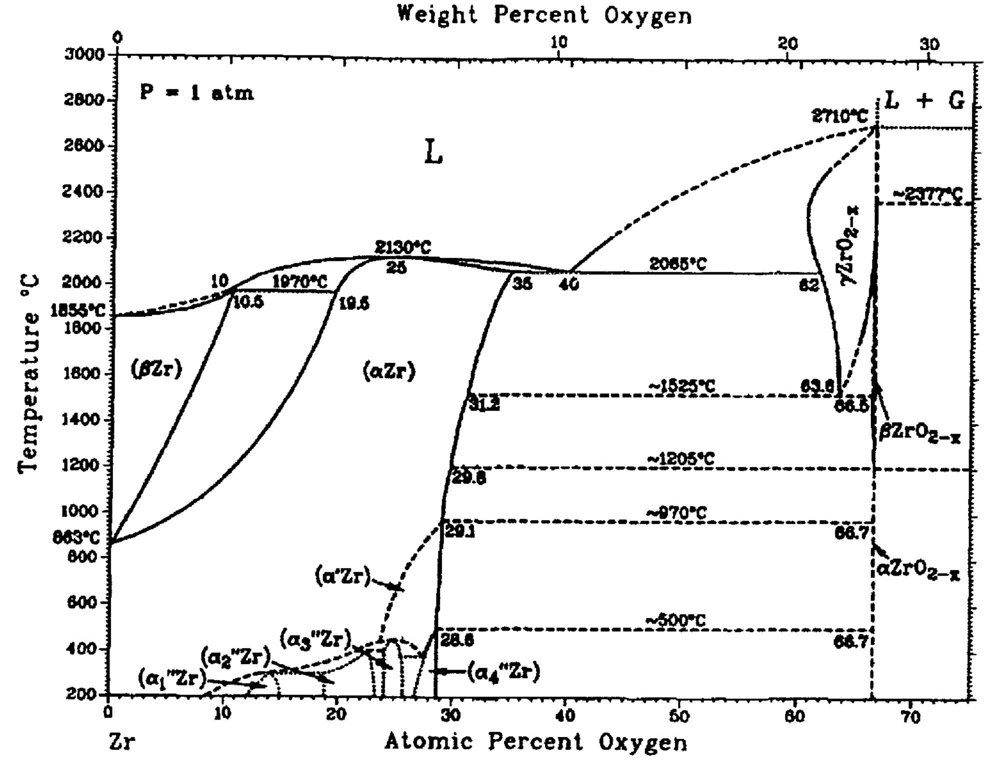

Figure 2-8: Zirconium-Oxygen phase diagram [11].

As we depart from the metal/oxide interface towards the oxide/water interface the lattice-mismatch-driven compressive stress on the oxide decreases and the monoclinic phase becomes the dominant phase with remnants of the tetragonal phase but no evidence for cubic or amorphous phases. The gradual decrease in the tetragonal phase as a function of distance from the metal/oxide interface is commonly attributed to the stress relaxation in the oxide layer as it grows. The addition of a new oxide layer at the metal oxide interface moves the older oxide layers away from that interface reducing the compressive stress on these older layers.

We conclude this subsection by discussing one of the most controversial and important issues in the literature which is the relationship between the corrosion rate and the fraction of the tetragonal phase. Some authors observed that zirconium alloys with a high tetragonal fraction near the metal/oxide interface exhibit a higher corrosion rate, whereas others observed the opposite (See Ref. [47] and the references therein). We present here two perspectives from the literature in trying to resolve this issue:

1. Qin et al. think that looking only at the fraction of the tetragonal phase is misleading and one has to consider the gradient of the compressive stress normal to the metal/oxide interface [47]. In particular, if there is large amount of the tetragonal phase at the metal/oxide interface, then this will lead to more of it being transformed to monoclinic when the stress decreases as the oxide grows. Since this phase transformation is accompanied by volume expansion, more cracks will form in the zirconia layer. On the other hand, if the compressive stress were to decrease sharply, then the tetragonal to monoclinic phase transformation would take place in the close vicinity of the metal/oxide interface breaking the oxide layer. They concluded that the optimum situation for a resistive oxide layer is having small fraction of the tetragonal phase near the metal/oxide interface and a low gradient of the compressive stress.
2. Motta et al. observed that highly oriented tetragonal grains that show (002) texture in X-ray diffraction measurements exist in all the resistant zirconia layers in the first 0.2 microns near the metal/oxide interface [43]. They claim that these particular grains are correlated with the protectiveness of the oxide. On the other hand, tetragonal grains that show (101) peak in XRD exist throughout the zirconia scale and have no correlation with protectiveness of the oxide. They deduced this observation from a comprehensive study on alloys of variable contents of alloying elements. The message of this study is that thinking in terms of tetragonal fraction is misleading and one has to consider the texture of the tetragonal grains. It is also reasonable to think that the texture and the energy minimization by accommodating a coherent compressively stressed zirconia at the metal-oxide interface are actually linked.

It is clear based on this discussion that the tetragonal fraction alone is not a suitable metric to characterize the corrosion resistance of zirconium alloys, and one has to consider simultaneously other factors such as the stress gradient and the texture of the tetragonal grains.

2.1.4.2 Microstructure

In the close vicinity of the metal/oxide interface the oxide grains have columnar shape that grows perpendicular to the interface as shown in Figure 2-9. These grains are surrounded by amorphous regions. As we depart from the metal/oxide interface the grains become equiaxed and periodic lateral cracks parallel to the metal/oxide interface start to develop. The periodicity of the lateral cracks matches the cyclic behavior in the corrosion kinetics as shown in Figure 2-10. In general the grains have a size less than 100 nm with the tetragonal grains smaller than the monoclinic grains [48, 49].

Several research groups attempted to establish coherent relationships between the grains of the different phases at the metal oxide interface. Such relationships are useful in modeling the microstructure of the zirconia scale. For example Zhou et al. showed that the cubic (c), tetragonal (t) and monoclinic grains can have the following coherent orientations relationship: (001)*m*//(110)*t* //(200)*c* [35]. Also, Motta et al. established on the basis of a comprehensive study in several alloys that form protective zirconia scale (including zircaloy-4) the following relationship that also includes the metal grains: $(10\bar{1}1)$*Zr* //(002)*t* //(020)*m* [43]. We recall that (002)*t* grains were observed only within 0.2 microns from the metal/oxide interface.

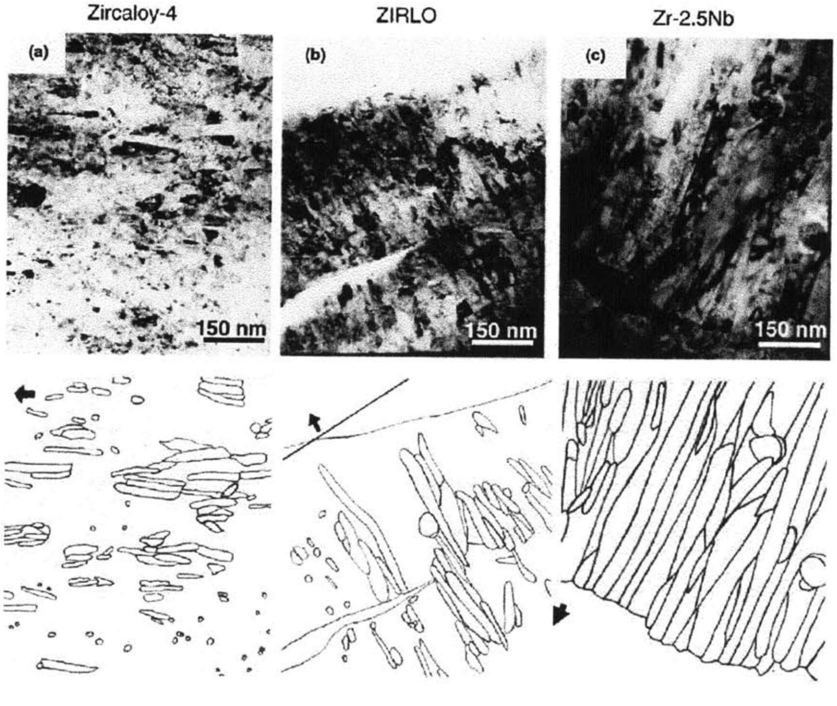

Figure 2-9: TEM images (top) and sketch of grains (bottom) of the oxide layer on (a) Zircaloy-4, (b) ZIRLO and (c) Zr-2.5Nb alloys near the metal/oxide interface in 360 ^{0}C. The arrows indicate the growth directions [48].

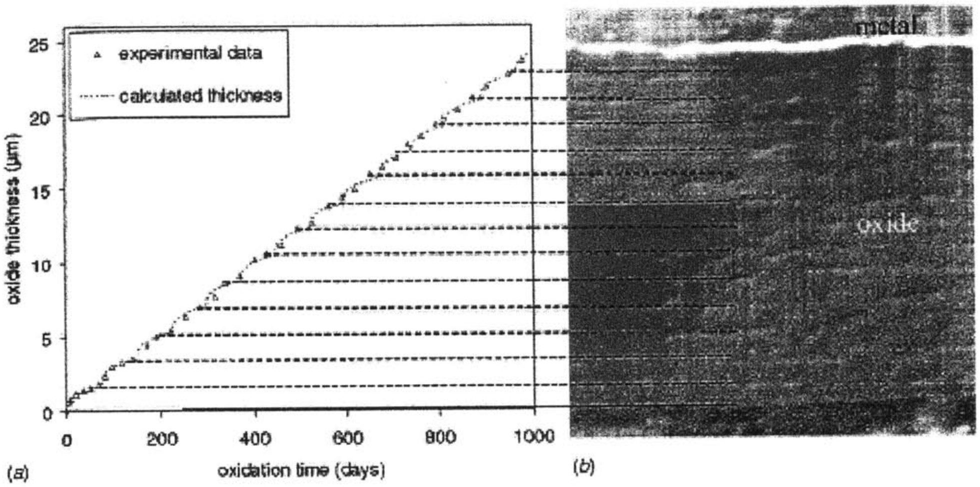

Figure 2-10: (a) Long-term reference oxidation kinetics. (b) Microscopic observation of the oxide layer of Zircaloy-4 in autoclave at 360 ^{0}C in 3.5 ppm LiOH and 1000 ppm H_3BO_3 chemistry [50].

2.1.4.3 Stoichiometry

The oxygen-to-zirconium ratio decreases smoothly from the stoichiometric oxide (66.67 atomic percent) to the metal-oxide solid solution limit (29 atomic percent) over a distance of about 0.5 micron as shown in Figure 2-11. Similar gradient in the oxygen content was established by molecular dynamics simulation for the early stage oxide phase that forms on Zr(0001) surface [46]. Of course this 0.5 micron region is above the solubility limit of oxygen in zirconium and still quite far from being considered an oxide. Yilmazbayhan et al suggested that this region is a suboxide of the form Zr_3O [48]. This chemical form can account for oxygen content of 25 atomic percent which cannot account for the smooth gradient over 0.5 micron. We think that this region may correspond to an irregular interface between the metal and the oxide in which there are metallic region interfering with oxide phases. Thus the net stoichiometry projected on a one dimensional plot may be misleading.

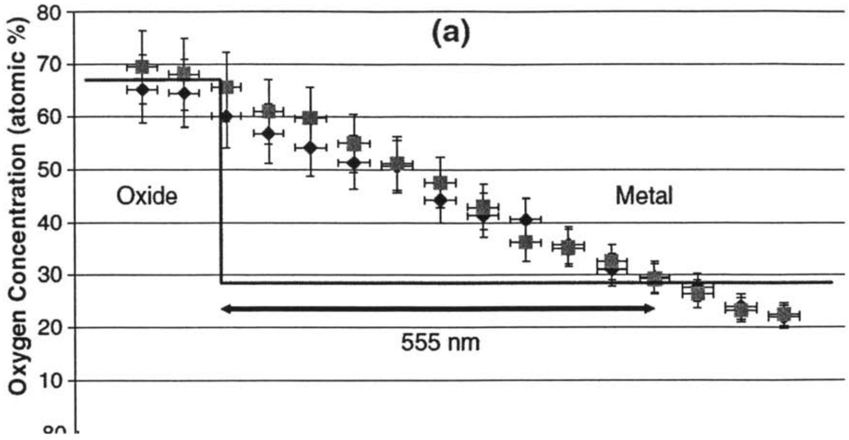

Figure 2-11: Measured oxygen content fromzircaloy-4 oxide formed in 360 ^{0}C pure water environment using EDS point spectra in TEM [48].

2.1.4.4 Stress state

The Pilling-Bedworth ratio, which relates the unit cell volume of the oxide to the unit cell volume for the untransformed metal from which it was made, is typically quoted as 1.56 for the monoclinic ZrO2/Zr system. This indicates that the volume of zirconia is greater than the volume for an equivalent number of zirconium atoms in its native HCP crystal structure. Thus, when forming an oxide layer from zirconium, the oxide is under planar compressive stress. Kim et al. measured the compressive stress as a function of the oxide thickness in the zirconia scale grown on pure zirconium metal [51]. Figure 2-12 summarizes their measurements and indicates that the stress level can reach 5 GPa in the close vicinity of the metal oxide interface.

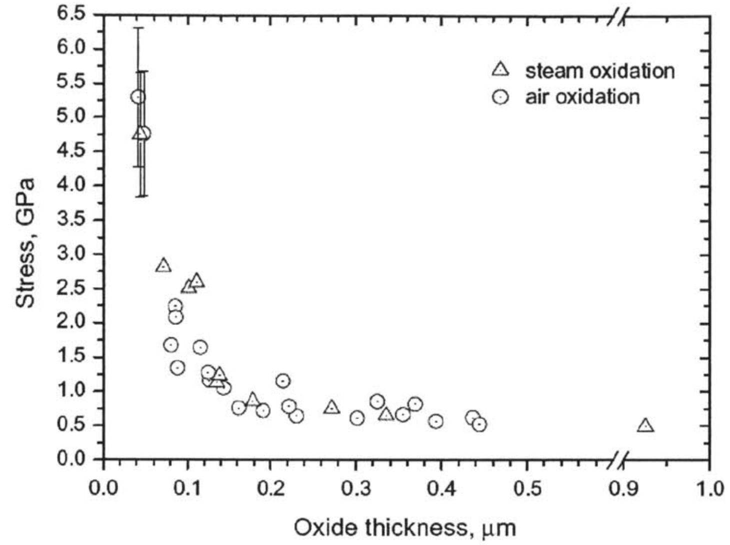

Figure 2-12: Measured stress vs. oxide film thickness [51].

It is expected that the stress level in the zirconium alloys will be slightly less than that in the pure metal because the secondary phase particles (SPP) are not oxidized immediately and hence remain in the metallic state for a period of time. The metallic SPPs are flexible compared to the oxide and can have a relaxing effect on the stress. Kim et al. compiled the previous stress measurements on the oxide scale grown on zirconium and its alloys [51]. This compilation is shown in Table 2-4 and includes the work of Kim et al. in the last row. Most of the previous measurements are in the range 0.2-2.0 GPa. It seems that the origin of these low values, which are actually very low to stabilize the tetragonal zirconia, is that these measurements were performed on thick oxides (greater than one micron) as an overall average. Apparently these previous studies could not capture the high stress level in the close vicinity of the metal oxide interface

Table 2-4: Compilation of the measured stress in the zirconia scale grown on zirconium and its alloys adapted from Ref. [51].

Measurement technique	Specimen info.	Oxidizing conditions	Stress (GPa) vs. oxide thickness (μm)	
Deflection	Zr	Chem. agent/25 °C	0.2	1.2
XRD	Zr/Zry-2	O_2/500 °C	1.2	1.9
			(2.4)	(0.4)
Curvature	Zr/Zry-2	O_2/500–700 °C	0.6 (max.)	~3.0
Deflection	Zry-2	O_2/500 °C	1.7 (max.)	~3.8
Curvature	Zr/Zry-2	Steam/400 °C	0.5–1.3	Not available
	Zr–1Nb	Steam/550 °C	0.2–0.6	
Curvature	Zry-4(pickled)	Steam/400 °C	0.9–0.2	0.5–6
	Zry-4(polished)		0.6 (max.)	~3
XRD	Zr–1.2Sn–0.2Fe	Steam/420 °C	2.0–1.5	1.8–3.6
	Zr–0.5Sn–0.2Fe		1.8–1.5	1.4–2.6
XRD	Zry-4	Steam/400 °C	0.7–0.2	1.0–2.5
Raman	Zry-4	Water/360 °C	0.7–1.3	1.0–1.6
	Zr–1Nb–0.12O		0.8–1.5	1.0–2.5
Curvature	Zr	Steam and O_2/450 °C	5.1–0.5	0.1–1.0

There are two fundamental phenomena in the corrosion for zirconium and its alloys that were attributed to stress in the literature. First, the appearance of the columnar grains close to the metal/oxide interface. Motta et al. explained that this type of growth is needed to accommodate the Pilling-Bedworth ratio in the normal direction to minimize the planar compressive stress on the oxide [43]. Second, Van Overmeere and Proost studied the very early stage (hundreds of seconds) of anodizing pure zirconium metal [52]. They showed that the tetragonal phase does not grow immediately upon oxidizing fresh metal. Instead, the monoclinic phase first is formed and after tens of seconds some of the monoclinic transforms to tetragonal and cubic phases to relax the large compressive stresses on the oxide. They observed a sudden drop in the stress upon the completion of the transformation. The same scenario can be the origin of the appearance of the cubic and tetragonal phases in the oxide scale of zircaloy-4. This early stage transition was denoted as type-I breakaway to distinguish it from type-II breakaway or what is commonly termed as the corrosion transition in the nuclear fuel cladding community which requires days to occur. The next subsection is intended to shed some light on type-II breakaway

2.1.4.5 The origin of the transition from cubic to linear growth law

In spite of the importance of understanding this transition, it remains one of the most controversial issues in the literature. All empirical corrosion models postulate certain oxide thickness at which the transition takes place. We are not aware of any model that can predict the transition without a priori postulated transition criterion. Thus, predicting the transition in corrosion kinetics is still a grand challenge for any physics-based corrosion model. Here we mention three of the most common explanations for the origin of the corrosion transition:

1. It was suggested that the transition is caused by the tetragonal or cubic to monoclinic phase transition when the stress relaxes on the tetragonal and cubic phases [53]. This stress relaxation occurs when the grains move away from the metal/oxide interface during the continuous growth of the oxide. The resulting phase transition is accompanied with large volume expansion which leads to the cracking of the oxide and accelerating the oxidation.
2. A second theory links between the formation of percolated porosity and the transition in corrosion kinetics. It is unavoidable to form porosity in the oxide scale grown on zirconium and its alloys. At some critical condition the pores percolate allowing easy penetration for water through the oxide layer and easy access to the metal/oxide interface and hence causing the transition [10]. However, the origin of the formation of porosity is not well understood. We quote, as an example, one hypothesis about the origin of the formation of porosity from Ref. [35]. Various point and line defects are present within the crystallites of the new oxide that forms at the metal/oxide interface. These defects are thought to be generated by the compressive stress at the interface. With the continuous growth of the oxide, the older layers depart away from the metal and hence the compressive stress relaxes, and with the action of temperature and time, the defects tend to migrate and get absorbed at the grain boundaries. The accumulation of the absorbed defects at the grain boundaries leads to the formation of pores.
3. The origin of the transition was also suggested to be purely mechanical. For example, Van Overmeere and Proost built a constitutive mechanical model that attribute the transition in corrosion kinetics and the formation of lateral cracks in the oxide to the arrival to a critical compressive stress value during the growth [52]. This critical stress leads to what they called buckling-induced delamination event.

2.2 Factors that accelerate the corrosion kinetics

Here we review the factors that can accelerate the corrosion process on zircaloy-4 in PWR. These include the effects of lithium and boron, secondary phase particles and CRUD induced localized corrosion. The interrelationship between accelerating corrosion and hydrogen pickup is discussed below in 2.3

2.2.1 Lithium and boron effects

About 0.5-3.5 ppm Lithium hydroxide (LiOH) is added to pressurized water reactor (PWR) primary water to control the pH value to be in the range of 7.2-7.4. Specifically LiOH is added to neutralize the effect of the boric acid ($B(OH)_3$) that is added to the primary water to control the neutronic reactivity. In such minute amounts, the LiOH is not particularly degrading for zirconium alloys. However, certain scenarios are expected to occur in PWR that can lead to locally elevating the concentration of LiOH to a level that can cause accelerated corrosion for zirconium alloys. One scenario is the formation of cracks (crevices) in the oxide layer due to delayed hydride cracking. These cracks can concentrate LiOH. Another scenario which is the most important is the concentration of LiOH in the pores of the CRUD deposited on the nuclear fuel clad. Since the current trend is to increase the burnups of the fuel in the reactor, the probability of the occurrence of these scenarios is high. We divide this section in two subsections. In the first we review the most important experimental observations regarding the potential role of LiOH in accelerating the corrosion of zirconium alloys, while in the second we present the attempts in the literature to explain the role of LiOH.

2.2.1.1 Observed phenomena related to the role of lithium hydroxide and boric acid

1- In autoclave corrosion experiments, when we compare the rate of corrosion in pure water to the rate of corrosion in lithiated water with LiOH concentration as high as 70 ppm, we find significant acceleration in the latter case. In some zirconium alloys, the pre-transition stage of corrosion is not even observable and the corrosion process starts with a linear growth rate for the oxide. Figure 2-13 from Ref. [48] demonstrates this trend.

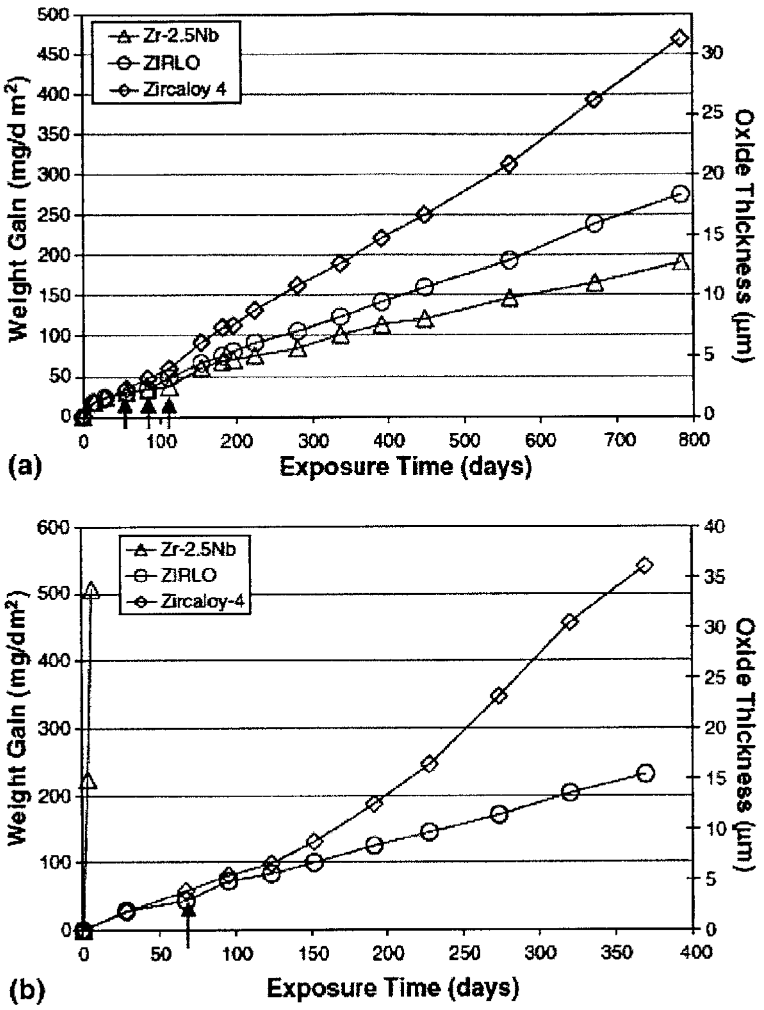

Figure 2-13: Corrosion weight gain vs. exposure time of Zircaloy-4, ZIRLO and Zr-2.5Nb in (a) 360 0C pure water (solid arrows show the transition) and (b) 360 0C lithiated water (solid arrow shows transition in ZIRLO, transition is not discernible in Zircaloy-r and Zr-2.5Nb) [48].

2- In trying to decide whether the elevated concentration of lithium or the elevated concentration of the hydroxyl groups is the origin of the observed corrosion acceleration, corrosion experiments were performed to compare between the effects of LiOH, NaOH and KOH. The accelerated corrosion was reported only in the case of lithium [54, 55]. This is a clear indication that the concentration of lithium is the major player in accelerating corrosion.

3- The enrichment factor is defined as the concentration of the Li^+ that gets into the zirconia scale to the concentration of Li^+ that was originally added to water. Enrichment factors as high as 10 were reported in autoclave corrosion experiments [55] (with no CRUD or delayed hydride cracking). When boiling of water is allowed in the corrosion experiments, the enrichment factor was found to increase with increasing the fraction of steam as shown in Figure 2-14 from Ref. [34]. However, the majority of this lithium that gets into the zirconia scale was found to be leachable upon washing by nitric acid [35] indicating that the major part of lithium was adsorbed in the pores and cracks of the oxide rather than being incorporated into its grains.

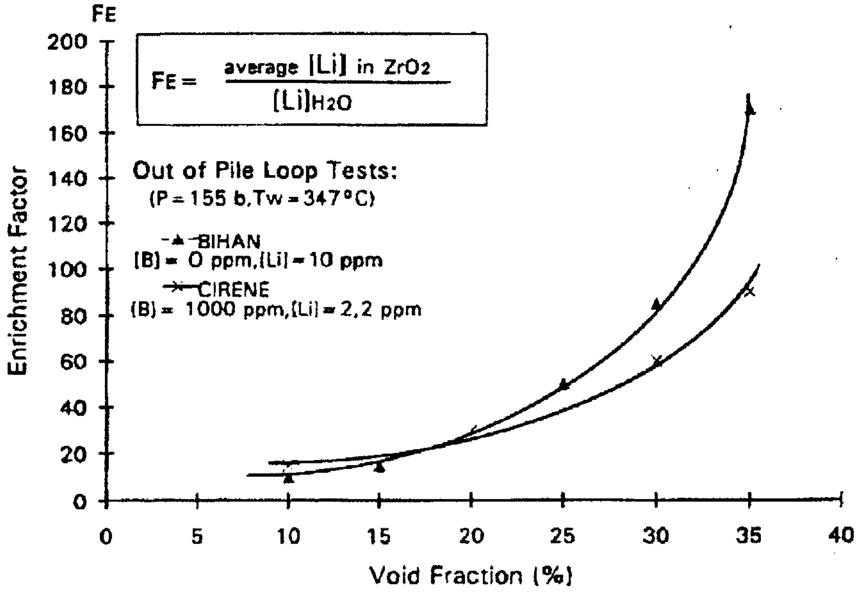

Figure 2-14: Lithium enrichment in the oxide layers as a function of void fraction in out-of-pile-loop tests [34].

4- When examining the microstructure in the zirconium alloys that suffered accelerated corrosion, it was found that at the metal oxide/interface only equiaxed grains exist [13, 55]. Away from the metal/oxide interface, the microstructure does not change that much compared to the corrosion in pure water, except that the pores and cracks are wider [35].

5- If a sample was oxidized in a LiOH environment and then switched to a new environment, the corrosion rate is adjusted quickly to that expected in the new environment [56].

6- If a sample is corroded in lithiated water in the presence of an equivalent amount of the boric acid, no acceleration is observed [13].

2.2.1.2 Hypotheses in the literature to explain the role of lithium and boric acid

First, we start with the three hypotheses about the role of lithium and then we present a hypothesis about the role of the boric acid in mitigating the detrimental lithium effects.

Explanation of the role of lithium

1- Cox suggested that the origin of the lithium-induced/-accelerated corrosion is due to preferential dissolution of tetragonal zirconia in the bottom of the pores of zirconia in which LiOH is concentrated [57]. This is to be followed by partial precipitation on the surface of the oxide scale later on. Mechanistically he suggested that once the dissolution /redeposition have occurred, the compressive stresses would be lowered and mainly monoclinic zirconia would grow, resulting in denser columnar layer. The growth of this layer will build up the compressive stresses again, increasing the tetragonal to monoclinic ratio, and leading to further increase in the oxide dissolution. It is worth noting here that some research groups found no evidence for zirconia dissolution in lithiated water [58].

2- The corrosion rate is expected to increase with increasing the number of the anion vacancies in the oxide. Thus, it was suggested that lithium in zirconia can be in a substitutional solid solution. For each Li^+ substituting Zr^{4+}, 3/2 of oxygen vacancies will form and hence the corrosion rate increases [55].

3- Perkins and Busch suggested that lithium accelerates the tetragonal to monoclinic transition which leads to the accelerated corrosion since this phase transition is associated with volume expansion [56]. Phase transformations induced by high concentration of interstitial lithium were observed in titanium oxide [59]. Furthermore, in a study for the dielectric properties of lithiated zirconia, it was suggested that lithium ions can exist in interstitial sites in zirconia [60].

Explanation of the role of boron in mitigating Li-effects

It is known from the isotopic exchange studies that Lithium can be replaced by boron [61]. Thus, it was proposed that boron existing as $B(OH)_3$ or $H_4BO_4^-$ functions as a blocking agent reducing the access of LiOH to the surface of zirconia [13]. Therefore, the presence of boron in these forms can actually serve to block the degrading effects of LiOH on zirconia surface.

2.2.2 The role of secondary phase particles (SPP)

Fe and Cr are added to zircaloy-4 to improve its corrosion resistance. The solubility of these elements in zirconium is very low and hence they precipitate an intermetallic phase of the form $Zr(Fe,Cr)_2$ which is known as the Laves phase. In general corrosion resistant precipitates in zirconium alloys are termed secondary phase particles (SPP). In a PWR relatively large SPPs (> 0.1 micron) are needed for corrosion resistance. The small particles can easily dissolve in the zirconium matrix under irradiation and hence become of no benefit for corrosion resistance. Figure 2-15 indicates this fact. Thus, the major concern in operating a PWR in a high burn-up regime is the dissolution of the SPPs in the zirconium metal which leads to accelerated corrosion. It is worth noting that the increased corrosion rate in BWR with the large SPP size is related to a phenomenon termed nodular corrosion that is not relevant to PWR environment and hence beyond the scope of this review.

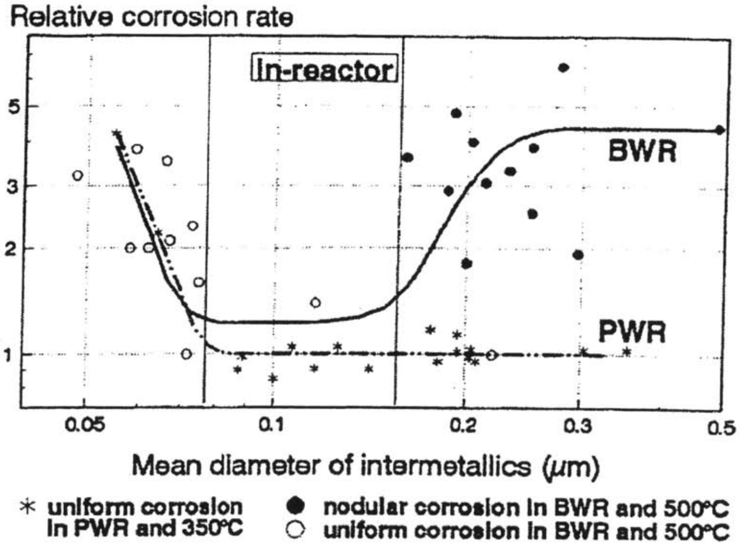

Figure 2-15: Effect of secondary phase particles size on corrosion [10].

When the oxidation front reaches an SPP, it was observed that Fe is very mobile in that case and migrate away from the SPP while chromium remains in the SPP [62]. Upon migration of iron, α-Fe, Fe_3O_4, Fe^{2+} and Fe^{3+} were detected by Mössbauer experiments [63]. The migrated iron atoms get oxidized and incorporated in the zirconia matrix and stabilize the tetragonal phase. Furthermore, upon oxidizing the remaining part of the SPP (after the migration of most of the iron content), the volume increases which induces compressive stresses in the neighboring zirconia matrix leading to stabilizing the tetragonal phase [64].

We conclude this section by highlighting a contradiction that we could not resolve from our literature review. We discuss in the next section of this chapter (2.3) that SPPs in their metallic form can act as a short circuit path for electron and hydrogen transport in zirconia. Furthermore, if the metallic SPP are exposed to water (for any reason such as a lateral crack in the oxide that leads to this exposure) then they catalytically increase the effective activity of dissociated species such as O^{2-}, OH^- and H^+ [16, 65, 66]. However, if SPPs disappear by irradiation-induced dissolution in the metallic matrix, the corrosion and the hydrogen pick-up rates becomes severely large [67]. The majority of the literature that we reviewed focuses on the adverse effects of *not*_having SPPs in the metal matrix, but when it comes to why the SPPs improve the corrosion resistance and reduce the hydrogen pick up, we found nothing significant to quote here.

2.2.3 CRUD induced localized corrosion (CILC)

CRUD[‡‡] is the corrosion products of all nickel and steel alloys in the primary loop of a PWR that gets deposited on the upper parts of the fuel cladding as a result of the subcooled boiling of the coolant. Thus CRUD is primarily made of porous nickel, iron and chromium oxides with some boron, lithium and zirconium related deposits. CRUD can accelerate the general corrosion of the cladding locally primarily by two effects, 1) thermal feedback, and 2) concentration of LiOH. In the first mechanism, the low thermal conductivity of the CRUD leads to higher clad temperature which in turn increases the general corrosion rate. The increased corrosion rate increases oxide thickness which lowers the overall thermal conduction of the clad and hence elevates the clad surface temperature leading to more and more CRUD deposits and the cycle goes on. Figure 2-16 from Ref. [11] shows a schematic for the thermal effect of CRUD.

[‡‡] It is sometimes assumed to be acronym for Chalk River Unidentified Deposits.

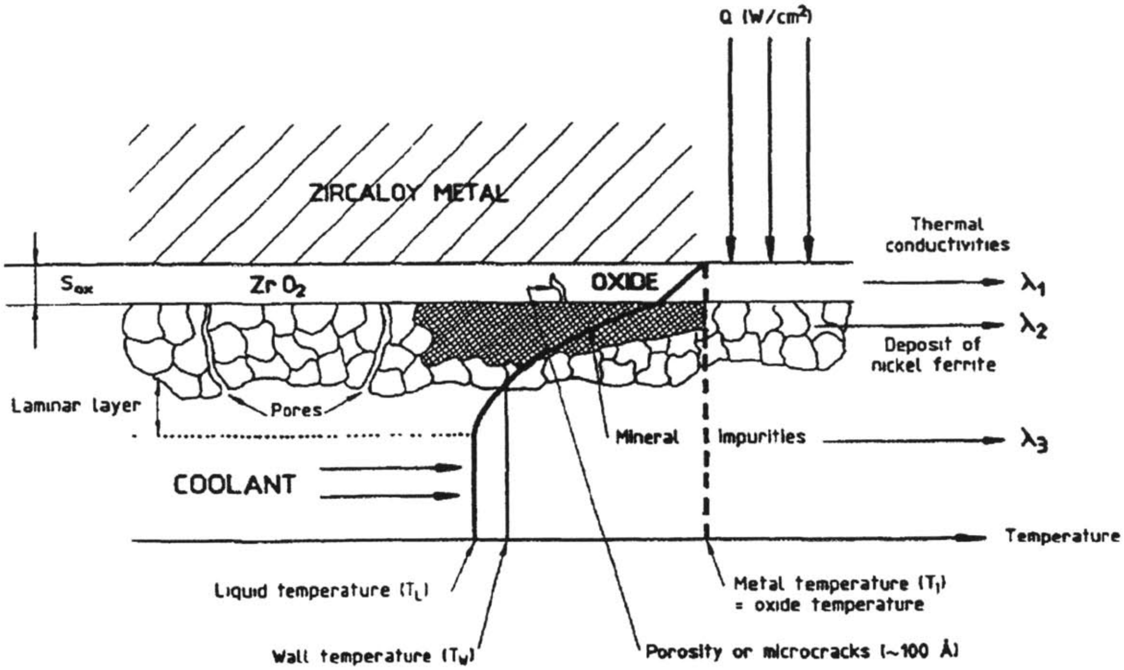

Figure 2-16: Thermal impact of CRUD deposition [11].

However, it is also believed that there are local chemical effects of CRUD that leads to what is commonly termed as CRUD Induced Localized Corrosion (CILC). The origin of the CILC hypothesis is the unexplained acceleration factor for corrosion rates in some regions of excessive subcooled boiling on the upper parts of the clad. Explaining these acceleration factors based on the thermal conductivity barriers of CRUD and zirconia failed [11]. It was suggested that the pores of the CRUD work as chimneys that enhance the boiling of the coolant. These chimneys can act as LiOH concentrators since the latter is known to be non-volatile. Thus the base of each of these chimneys has a local supersaturation of LiOH. On the other hand it was demonstrated that the intrinsic corrosion properties of Zircaloy are affected when lithium is incorporated into the lattice of the oxide [68] or into the micro-cracks of the post transition film [37]. Thus, the consequence of this local effect of concentrating lithium is increasing the corrosion rates locally and then the oxide thickens significantly leading to a later thermal activation of corrosion by the thermal feedback effect explained above. This picture has been demonstrated in some failures observed in the Saxton reactor [11]. The only missing link in this picture is what actually lithium does to accelerate the corrosion. If the latter is known, a predictive model for corrosion can be introduced to account for these local effects.

2.3 Hydrogen pickup and its relation to corrosion kinetics

Hydrogen gas is added to pressurized water reactor (PWR) coolant to reduce the corrosion of iron and nickel alloys. Furthermore it is a product of the waterside corrosion of zircaloy-4. It is well documented that hydrogen penetrates the oxide scale on zircaloy-4 reaching the metal substrate and forms solid solution with zirconium. Once the solubility limit is exceeded, zirconium hydrides precipitate which lead to embrittlement. The focus of this section is analyzing the source term for hydrogen pick up in the zirconium alloy. By this we mean the mechanism and kinetics by which hydrogen gets incorporated into the oxide, transported through it and enters the metal. This forms the first subsection of this section. The second subsection focuses on the effect of the presence of hydrogen in zirconia layer on the corrosion kinetics.

2.3.1 Hydrogen pickup and its transport

The hydrogen gas dissolved purposefully in PWR coolant does not get into the metal as was shown through oxidation studies using tritium/water mixtures (T_2/H_2O) [11]. The only remaining hydrogen source in PWR conditions is the hydrogen produced due to corrosion. What is actually produced in the corrosion reaction is protons and OH groups. The protons get neutralized by recombination with electrons forming hydrogen atoms; it is not known where exactly this reaction takes place, on/in the oxide or when proton reaches the zirconium metal or when it reaches an interphase with the SPPs. If the unoxidized interrmetallics (undissolved secondary phase particles) are still present, they may act as optimal sites for proton-electron recombination. Upon the dissolution of the intermetallics, the whole zirconia lattice can serve as the recombination medium. Part of the neutral hydrogen atoms recombines to form hydrogen gas molecules that evolve back to water and part of it penetrates through the oxide and eventually reaches the metal. The ratio of the hydrogen that reaches the metal to the total amount of hydrogen produced during the corrosion reaction is called the hydrogen pickup fraction (HPUF). For PWR condition, it is assumed to be constant. For example in the code FRAPCON-3 it is assumed to be 0.15 [69]. It should be emphasized that is not known how long the distance through which the proton migrates through the oxide scale before it recombines with an electron.

Another important point is that even when there are cracks in the oxide scale, there will always be a coherent zirconia layer at the metal oxide interface that hydrogen (in the form of a proton or a neutral atom) has to cross, so we believe that the bulk transport of hydrogen in zirconia must be taking place eventually.

As we pointed out, the unoxidized secondary phase particles act as optimal sites for hydrogen recombination with electron and moreover they act as short circuits for hydrogen diffusion. Hatano et al. performed an experiment to determine the influence of second phase particles on hydrogen transport through the oxide layer on zircaloy-4 [70]. It was determined that specimens with larger second phase particles had higher hydrogen uptake than those with smaller particles, and it was proposed that a) the second phase particles act as short-circuit diffusion paths, and b) the large particles remain unoxidized for longer, remaining as short-circuit paths for longer than the small particles. Furthermore there is a strong correlation between the hydrogen uptake percentage and the nature of the elements in the secondary phase particles. Figure 2-17 from Ref. [8] illustrates this correlation. The peak at nickel was the reason of excluding it from zircaloy-4. It was argued [11] that when the secondary phase particles dissolve into the oxide matrix, they remain as metal atoms embedded in the oxide lattice and these metal atoms cantinue to facilitate the transport of hydrogen through the oxide layer. We do not think that this argument is valid for two reasons. First, Mössbauer experminsts [63, 71] demonstrate nonzero oxidation state for the secondary phase particles elements when dissolved in the zriconia matrix. Second, in chapter 8 we will show using density functional theory calculations that neutral metal atoms either are not stable in the lattice of zirconia or have a very high formation energy.

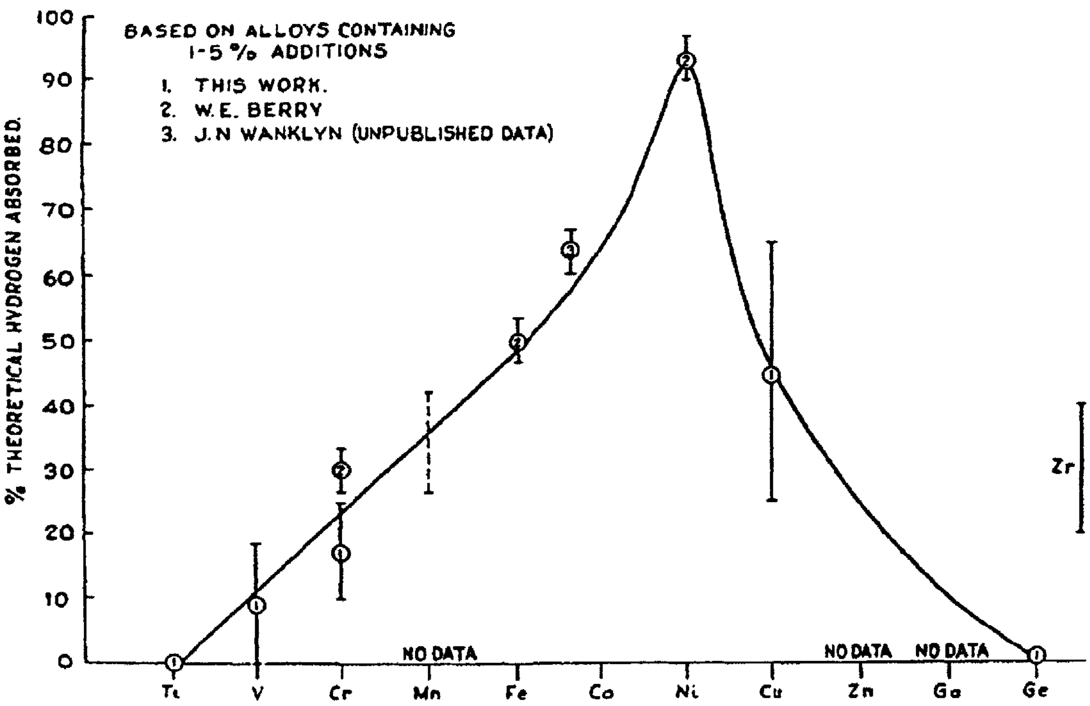

Figure 2-17: The effect of alloying elements on hydrogen pickup percentage [8].

We turn now to discuss literature data regarding the presence and diffusion of hydrogen in zirconia. Miyake et al. showed that the solubility of hydrogen in monoclinic zirconia (denoted by α-ZrO2) is in the range of 10^{-5}-10^{-4} mol H/mol oxide and decreases with increasing temperature. Figure 2-18 shows that the solubility of hydrogen in tetragonal zirconia (denoted by β-ZrO_2) is higher than in monoclinic phase (denoted by α-ZrO_2). It was observed that hydrogen diffusivity is inversely proportional to the amount of the tetragonal phase in the scale [72]. In other words, hydrogen diffuses faster in the monoclinic phase compared to the tetragonal one. In fact Duong et al. demonstrated through employing secondary ion mass spectroscopy (SIMS) on single crystals that hydrogen can diffuse in tetragonal zirconia but not in the cubic phase and extrapolated that hydrogen should diffuse faster in the monoclinic phase [31].

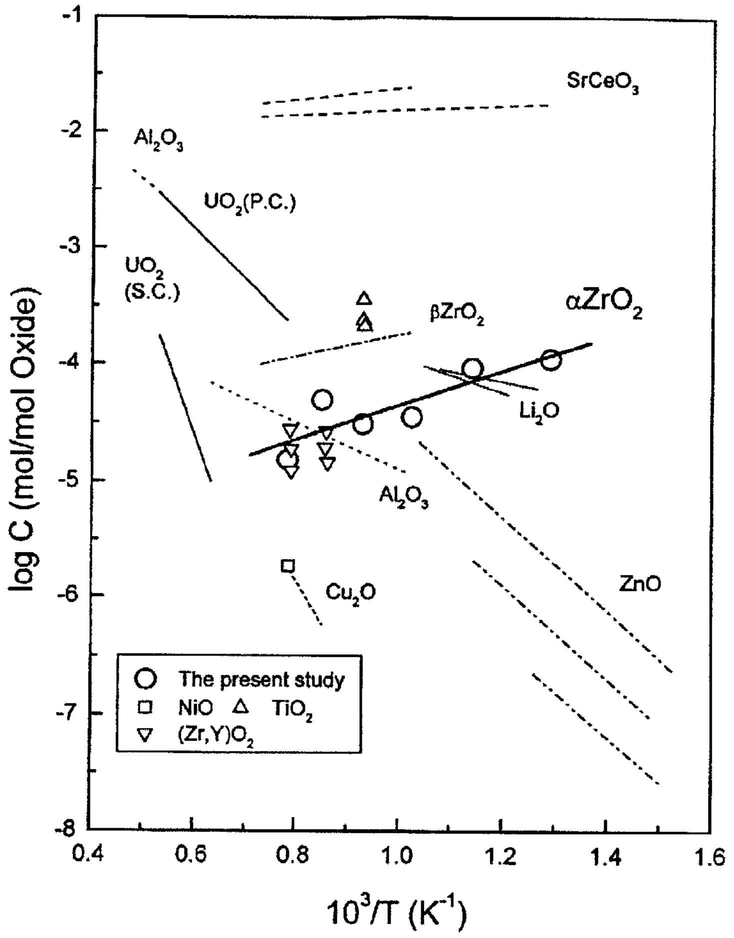

Figure 2-18: Temperature dependence of hydrogen solubility in some oxides [73].

Regarding the presence of protons in zirconia, it is believed that interstitial protons in zirconia are bonded to lattice oxygen [16]. The term "substitutional hydroxide" is frequently used to refer to this defect [16]. However, this type of defect cannot account for all the hydrogen observed in zirconia. This is due to the fact that the intensity of the O-H stretching frequencies measured by infra-red spectroscopy appears to be less than what would be necessary to account for the amount of hydrogen measured by SIMS [11, 74, 75]. The SIMS measurements indicate higher concentrations of hydrogen to be present in zirconia. Both the Infra red and the SIMS data were taken in corrosion experiments.

It is clear that there is significant uncertainty in identifying the nature of the hydrogen species that penetrates zirconia. Also, while it is admitted that there is always a coherent zirconia layer that hydrogen has to cross to reach the metal beneath, it is unclear what the diffusion mechanism is. In spite of this, we present here some mechanistic and quantitative aspects of hydrogen diffusion in zirconia.

Bulk (through lattice) diffusion in single crystal tetragonal was studied by Doung et al. They concluded that hydrogen diffuses in the form of proton in zirconia in a path that is parallel but independent from the diffusion of the oxygen anion. That means that the hydroxyl group does not diffuse as a coherent entity in zirconia. Instead they suggested that protons associate with oxygen vacancies and they jump whenever the vacancy jumps. Vacancy hopping is the mechanism by which oxygen ions diffuse and hence the description "parallel but independent". The suggested mechanism has an inherent assumption that was not discussed by the authors. They assumed that the oxygen vacancies implicitly trap electrons (F-center), otherwise it will repel the proton.

Grain boundary diffusion of protons in fluorite-based oxides has been recently studied. Confer Ref. [76] and the references therein. It was shown that zirconia and ceria in nanocrystalline forms are proton conductors below 200 ^{0}C in atmospheric environments. The smaller crystallites ~ 20 nm showed the faster conductivity. In fact the zirconia crystallites that grow at the metal/oxide interface have similar size, and it is worth considering this path for hydrogen diffusion leading to hydrogen pick up.

Khatamian and Manchaster determined that hydrogen in the oxide scale formed on pure zirconium metal diffuses with an activation barrier of 1.04 eV and a prefactor of 1.13×10^{-12} m^2/s [77]. In addition Angel estimated that at 400 ^{0}C, the hydrogen diffusivity in the metal is 7-10 orders of magnitude faster than its diffusivity on the oxide scale formed on the metal [16].

2.3.2 Effect of hydrogen on the corrosion kinetics

To the best of our knowledge, correlating the presence of hydrogen in zirconia with the corrosion kinetics has not been discussed in the literature on a sound ground except from a recent paper by Harada and Wakamatsu [78]. In their corrosion experiments in pure water on zircaloy-4, they found in inverse correlation between the oxidation (weight gain) and the hydrogen pick-up within each cycle of the corrosion kinetics cycles. At the beginning of each cycle including the very first one, the oxidation rate is slow while the hydrogen pick-up is fast. At the end of every cycle, they observed the opposite behavior, where the oxidation rate increases and the hydrogen-pickup decrease. Figure 2-19 summarizes this trend.

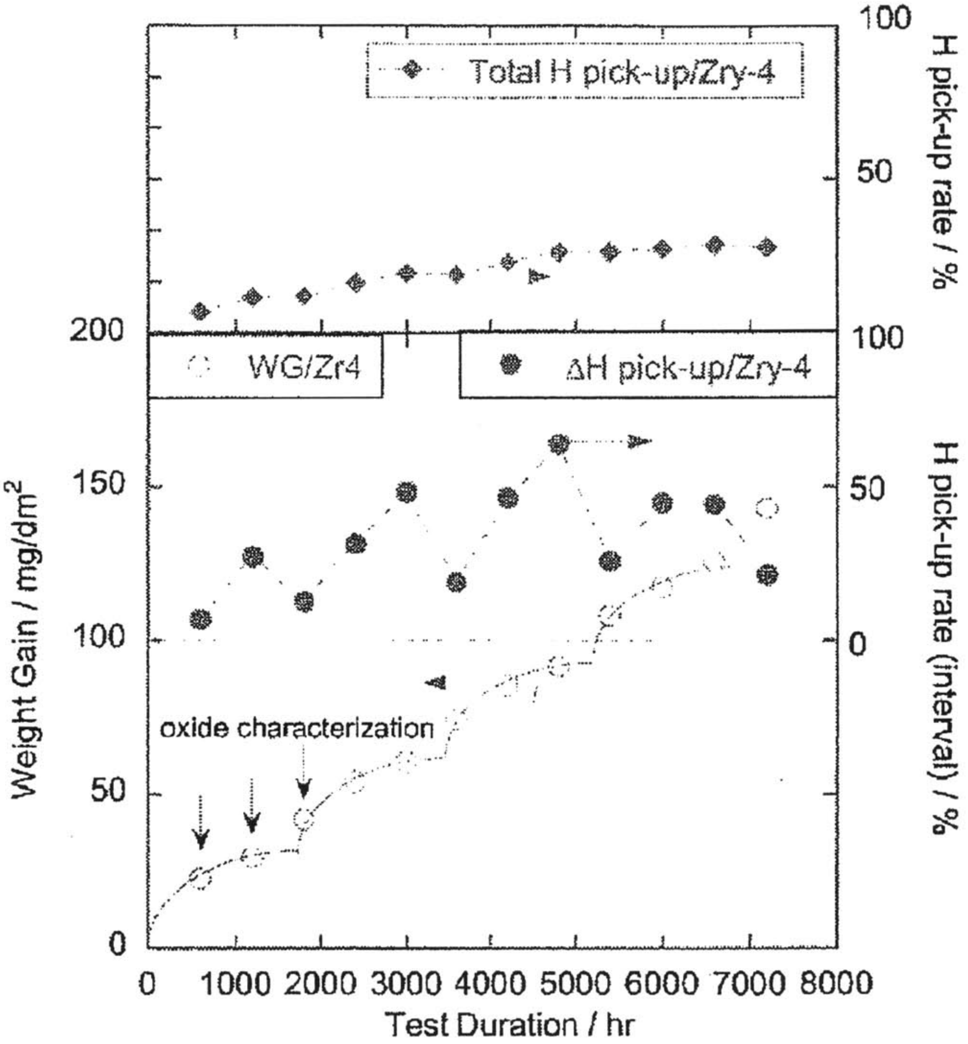

Figure 2-19: Corrosion behavior and hydrogen pick-up of Zircaloy-4 in pure water at 360 °C [78].

To interpret this behavior Harada and Wakamatsu suggested that right after the transition between two cycles, the increased corrosion rate is due to the growth of the columnar grains in the oxide and they judged that these columnar grains suppress the hydrogen ingress to the metal. Right before the transition between the two cycles, the corrosion rate is suppressed by the substoichiometric interfacial oxide layer, but the hydrogen accumulated in the oxide diffuses through the interface layer to the metal. Figure 2-20 is a schematic description of this hypothesis.

They went one step further by suggesting that hydrogen in the oxide assists the growth of the columnar grains at the beginning of each cycle. They based this suggestion on comparing the morphology of the oxide that grows in pure water corrosion experiments and the oxide scale that grows in a mixed gas environment (3% O_2 and 97% Ar). Before a cycle transition the oxide/metal interface had a wavy shape. However, after the cycle transition, the wavy interface changed into a smooth interface for the specimens corroded in water.

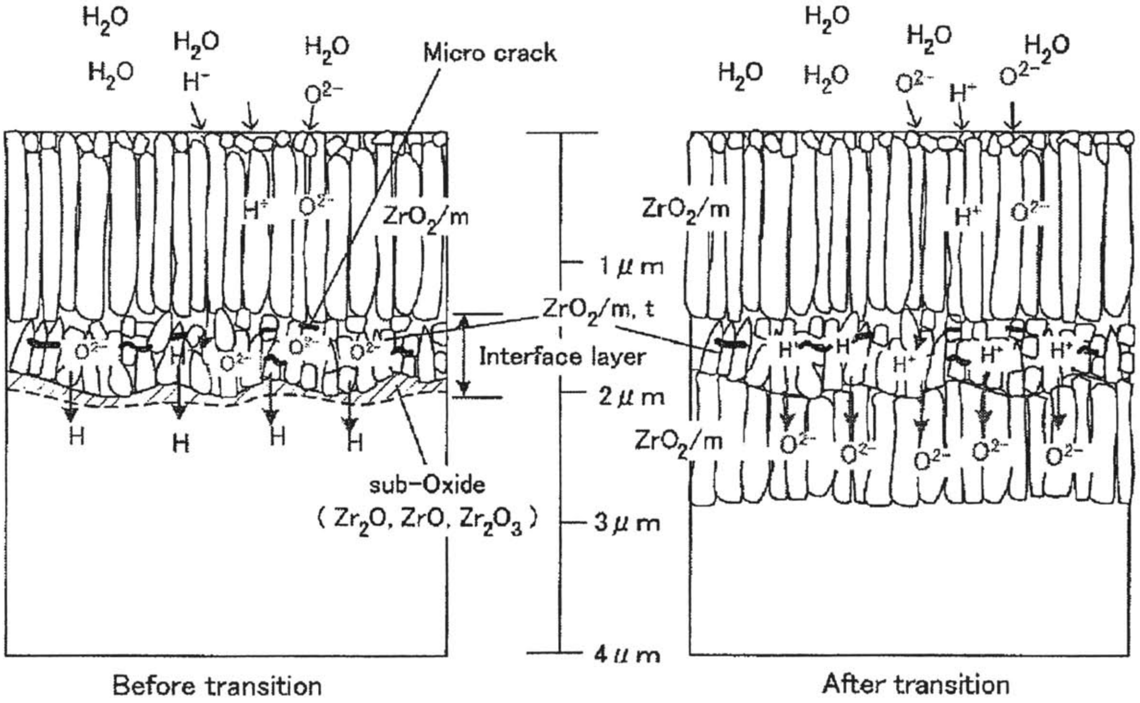

Figure 2-20: Schematic diagram of the morphology of the oxide before and after transition [78].

Chapter 3 : Modeling defect equilibria in metal oxides: Application to tetragonal and monoclinic zirconium oxide

Abstract

We present a density functional theory (DFT) framework taking into account the finite temperature effects to quantitatively understand and predict charged defect equilibria in a metal oxide. Demonstration of this approach was performed on tetragonal (T-ZrO_2) and monoclinic (M-ZrO_2) zirconium oxide. We showed that phonon free energy and electronic entropy at finite temperatures add a non-negligible contribution to the free energy of formation of the defects. Defect equilibria were conveniently casted in Kröger-Vink diagrams to facilitate realistic comparison with experiments.

For T-ZrO_2, consistent with experiments, our DFT-based results indicate the predominance of free electrons at low oxygen partial pressure ($P_{O_2} \leq 10^{-6}$ atm) and low temperature ($T \leq 1500K$). In the same regime of P_{O_2} but at higher temperatures, we discovered that the neutral oxygen vacancies (F-centers) predominate. The nature of the predominant defect at high oxygen partial pressure has been a long standing controversy in the experimental literature. Our results revealed this range to be dominated by the doubly charged oxygen vacancies at low temperatures ($T \leq 1500\,K$) and free electrons at high temperatures. T-ZrO_2 was found to be hypostoichiometric over all ranges of T and P_{O_2} mainly due to the doubly charged oxygen vacancies, which are responsible for inducing n-type conductivity via a self-doping effect. A range of 1.3 eV in the band gap of T-ZrO_2 starting from the middle of the gap towards the conduction band is accessible to the chemical potential of electrons (Fermi level) by varying T and P_{O_2} without extrinsic doping.

For M-ZrO_2, we showed that at low P_{O_2}, the predominant defect is free electrons compensated with fully ionized oxygen vacancy. This result is consistent with the experimental determination. In high P_{O_2} there is a consensus that free holes are the predominant defects, but no similar agreement on the compensator. Our approach showed that below 800K, fully ionized zirconium vacancies charge-balance the free holes, while above 800K doubly charged oxygen interstitials are the compensator.

The approach and the results related to tetragonal ZrO_2 were published in Physical Review B [79].

3.1 Introduction

In this chapter we introduce a theoretical framework to quantitatively understand and predict charged defect equilibria in a metal oxide. To facilitate realistic comparison with experiments we cast these equilibria in the convenient representation of Kröger-Vink diagrams. The framework is informed by density functional theory (DFT) total energy calculations and takes into account finite temperature effects. We demonstrate this framework on both tetragonal and monoclinic zirconium oxide (T-ZrO_2 and M-ZrO_2). As discussed in the previous chapter these are the most relevant phases for the oxide scale that grows on zirconium alloys and so understanding their defect equilibria is essential in order to develop deeper understanding of the atomic processes that control the corrosion and hydrogen pickup of zirconium alloys

Beyond the fact that zirconia is the scale that protects zirconium alloys in nuclear reactors, ZrO_2 actually) belongs to the list of the most important metal oxides due its wide usage in different technological applications [15]. In energy systems it is used in fuel cells [80], in gas sensors [81], and as a thermal barrier coating [82]. Its applications were recently extended to include usage as a gate dielectric for metal oxide semiconductor devices [83] and in biomedical applications such as hip implants [84] and dental restorations [85]. This diversity in zirconia applications is attributed to its superior properties; in particular it has high strength and fracture toughness [14], an ionic conductivity that can be significantly enhanced by doping [86] and straining [87], and high dielectric constant [83]. Thus our analysis presented here has an impact on these applications of zirconia too.

In the rest of this chapter we introduce the theoretical approach to model defect equilibria, next we present a demonstration of this approach on T-ZrO_2 and finally on M-ZrO_2.

3.2 Theoretical approach to model charged point defect equilibria in a metal oxide

This section is presented in four subsections. First, we present the relevant thermodynamics of defect formation in a metal oxide. Second, we describe the algorithm of constructing the Kröger-Vink diagram. Third, we explain how we included finite temperature effects in our calculations. Finally, we describe the needed DFT calculations.

3.2.1 Thermodynamics of the formation point defects

To understand the energetics of the formation of a point defect in a metal oxide exemplified here by ZrO_2, we appeal to the picture of a constrained grand canonical ensemble. In this picture a crystal of ZrO_2 of a fixed volume is constrained to exchange oxygen, but not zirconium, with an oxygen reservoir of a fixed temperature and oxygen chemical potential. In fact the volume does not have to be fixed but we assume that the change of volume due to the creation of point defects is negligible when these defects have dilute concentrations which is the case for ZrO_2. In this constrained ensemble, physically, the creation of all types of point defects occurs by exchanging only oxygen with the reservoir. Thus an oxygen vacancy forms by removing an oxygen atom from the crystal and inserting it in the reservoir. Conversely, incorporating an oxygen atom from the reservoir into an interstitial site in the crystal leads to the formation of an interstitial oxygen. To create a zirconium vacancy, two oxygen atoms get incorporated in the crystal in regular lattice sites representing a ZrO_2 unit formula missing zirconium cation. On the other hand creating a zirconium interstitial requires moving two oxygen atoms from the crystal into the reservoir and displacing a zirconium cation from its original lattice site to an interstitial site. In all these reactions charge neutrality has to be maintained. We elaborate on the latter condition in the next subsection. While this formalism does not rely on the traditional concepts of Frenkel and Schottky disorder, accounting for them is still amenable within this constrained ensemble as can be readily understood on the basis of the defect creation processes described above (simply by composing Frenkel or Schottky from their constituents) and as will be shown quantitatively later in this subsection. The picture described above is necessary to understand the energetics of point defect creation, however, the actual modeling of these defects in a DFT supercell is described in subsection 3.1.4. We can now define the Gibbs free energy of formation, $G^f_{D,q}$,of the defect D that has a charge q as follows:

$$G^f_{D,q} = \Delta E^{solid}_{potential} + \Delta E^{solid}_{vib} - T(\Delta S^{solid}_{vib} + \Delta S^{solid}_{elec}) + P\Delta V \pm \mu_D, \qquad (3\text{-}1)$$

where $\Delta E_{potential}^{solid}$, ΔE_{vib}^{solid}, ΔS_{elec}^{solid}, ΔS_{vib}^{solid}, ΔV are the differences in potential energy, vibrational energy, electronic entropy, vibrational entropy, and volume between the defected and perfect crystals. P is the pressure, T is the temperature, and μ_D is the chemical potential of the species D. As discussed above the change in volume is negligible and hence the $P\Delta V$ term can be set to zero. The term $\Delta E_{vib}^{solid} - T\Delta S_{vib}^{solid} = F_{vib}^{solid}$ represents the phonon contribution to the free energy of formation of the defect. This contribution is significantly enhanced with temperature. The term $-T\Delta S_{elec}^{solid}$ is also enhanced with the temperature and adds a non-negligible contribution to the free energy of formation of the defect. Subsection 3.1.3 addresses these finite temperature effects. It is worth noting that the convention is to exclude the configurational entropy of the defects from the definition of the Gibbs free energy. However, the contribution of this entropy is still accounted for implicitly when computing the concentrations of the defects as described in the next subsection. Indeed defects are stabilized in crystals at finite temperature mainly due to the configurational entropy [88]. Finally, we define the term $\Delta E_{potential}^{solid} \pm \mu_D$ as the formation energy of the defect and denote it by $E_{D,q}^{f}$. Next we describe the details of the latter term.

The formation energies of oxygen and zirconium defects can be computed as follows:

$$E_{O,q}^{f} = E_{defected} - E_{perfect} \pm \frac{1}{2}\mu_{O_2} + q(E_{VBM} + \mu_F) + E_{MP}, \tag{3-2}$$

$$E_{Zr,q}^{f} = E_{defected} - \frac{N \mp 3}{N} E_{perfect} \mp \mu_{O_2} + q(E_{VBM} + \mu_F) + E_{MP}, \tag{3-3}$$

where the top signs are for vacancies and the bottom signs are for interstitials. $E_{defected}$ is the DFT energy of the supercell that contains the defect. $E_{perfect}$ is the DFT energy of the perfect supercell. μ_{O_2} is the chemical potential of oxygen. E_{VBM} is the energy of the valence band maximum in the perfect supercell. μ_F is the chemical potential of electrons (or the Fermi level) relative to the valence band maximum and hence it can take values from 0 to the width of the band gap in the perfect crystal. E_{MP} is the Makov-Payne correction for the multipole interactions between the periodic images of the charged defects [89]. We considered only the leading term of the Makov-

Payne correction which accounts for the monopole-monopole interaction. This term scales as $1/L$ where L is the length of the supercell (~ 10.3 Å in our simulations) and is considered to be the dominant term for charged defects in ionic crystals [89, 90]. Higher order terms are not considered here as their contribution is expected to be smaller because (1) the leading term of the neglected part of the correction scales as $1/L^3$; (2) All terms are scaled by the high dielectric constant of tetragonal zirconia which is 39.8 [91] and for monoclinic zirconia is 20 [92]. Further details about the computation of formation energies and the accuracy of the Makov-Payne correction are given in section 3.5 .

The chemical potential of oxygen, μ_{O_2}, is defined as follows [93]:

$$\mu_{O_2}(T, p_{O_2}) = E_{O_2}^{DFT} + \mu_{O_2}^0(T, P^0) + k_B T \ln(\frac{p_{O_2}}{P^0}), \tag{3-4}$$

where, $E_{O_2}^{DFT}$ is the total energy of an isolated oxygen molecule as computed by DFT, p_{O_2} is the partial pressure of the oxygen gas, and k_B is Boltzmann constant. $\mu_{O_2}^0(T, P^0)$ is the difference in chemical potential of O_2 between $T=0$ K and the temperature of interest at the reference pressure P^0 which is typically taken as 1 atm. The term $\mu_{O_2}^0(T, P^0)$ was obtained from thermo-chemical tables [94]. It is important to note that equation (3-3) implicitly indicates that the chemical potential of zirconium, μ_{Zr}, is defined as:

$$\mu_{Zr} = E_{ZrO_2}^{DFT} - \mu_{O_2}, \tag{3-5}$$

where $E_{ZrO_2}^{DFT}$ is the DFT energy of the unit formula of ZrO_2 in the perfect crystal of zirconia. As mentioned in the beginning of this subsection, it is still possible to account for the traditional concepts of Frenkel and Schottky disorder. The formation energy of composite defects such as Frenkel pair or Schottky defect becomes the sum of the individual formation energies of the components of the composite defects as can be readily seen from equations (3-2), (3-3).

3.2.2 Construction of the Kröger-Vink diagram

The basic idea that governs the Kröger-Vink diagram is that at a given temperature and oxygen partial pressure, the concentration of ionic and electronic defects should sum up to achieve charge neutrality in the bulk of the ionic crystal. This statement can be expressed in mathematical terms as follows:

$$\sum_{D,q} q[D^q] + p_v - n_c = 0, \qquad (3\text{-}6)$$

where $[D^q]$ is the concentration of a point defect D of charge q, p_v is the concentration of holes in the valence band, n_c is the concentration of electrons in the conduction band, and the summation is taken over all charged defects. The concentration of a point defect D with charge q was derived by Kasamatsu et al. [5] by minimizing the Gibbs free energy of the defected crystal and hence accounting for the configurational entropy. The expression is:

$$[D^q] = n_D \frac{\exp(-\frac{G^f_{D,q}}{k_B T})}{1+\sum_{q'} \exp(-\frac{G^f_{D,q'}}{k_B T})}, \qquad (3\text{-}7)$$

where n_D is the number of possible sites for the defect D in the lattice per chemical formula of ZrO_2 and thus the concentration is given in units of number of defects per chemical formula. The functional form of the concentration of a point defect is similar to the Fermi-Dirac distribution, although no quantum mechanical considerations were accounted for in the derivation. The assumption $G^f_{D,q'} >> k_B T$ for all charges q' leads to neglecting the summation in the denominator and obtaining the familiar Boltzmann-like expression for a point defect concentration. However, we are not adopting this assumption as it breaks down at high temperature and/or extreme oxygen partial pressure conditions. Special care needs to be taken in applying the summation in equation (3-7) This is a summation over the charge states of the defect that compete for the same site in the lattice. As an illustration for this subtle point we consider the case of oxygen interstitial defects in tetragonal zirconia in the charge states -2,-1,0. As will be shown in section 3.2 below, the charge states -1 and 0 compete for the <110> dumbbell site while the -2 charge state favors an octahedral site. Thus, in computing the concentration of the charges -1,0 the summation in the expression has to run over those two charges, while for -2, the summation includes only -2 because there is no other charge states that compete for the same site. Indeed, the negative U-behavior of the oxygen interstitial led to a further simplification which is excluding the -1 charge state at all.

The concentration of electrons in the conduction band and holes in the valence band is given by applying Fermi-Dirac statistics to the electronic density of states [95] as follows:

$$n_c = \int_{E_{CBM}}^{\infty} g_c(E) \frac{dE}{1+\exp(\frac{E-\mu_F}{k_B T})},$$
$$p_v = \int_{-\infty}^{E_{VBM}} g_v(E) \frac{dE}{1+\exp(\frac{\mu_F - E}{k_B T})}, \tag{3-8}$$

where $g_c(E)$, $g_v(E)$ are the density of electronic states in the conduction band and valence band per volume of the chemical formula ZrO_2, respectively. E_{CBM} is the energy of the conduction band minimum.

With the above expressions, the construction of the diagram at a fixed temperature proceeds by examining a wide range of the oxygen partial pressure. At each value of the later, there is only one value for the chemical potential of electrons, μ_F, that achieves the charge neutrality condition. This value of the electron chemical potential has to satisfy two constrains, otherwise we designate the oxygen partial pressure under examination as inaccessible. The first constraint is that the electron chemical potential has to have a value between the valence band maximum and the conduction band minimum. The second is that the formation energies, $E^f_{D,q}$, of all the defects have to be positive because a negative value of the formation enthalpy indicates that the crystal is not stable at these values of the electron chemical potential and a phase transition or phase separation would take place at such values to avoid instabilities in the crystal. A final constraint that we applied to the overall construction of the Kröger-Vink diagram is limiting the search for accessible thermodynamic conditions (T, P_{O_2}) to an off-stoichiometry, x, in ZrO_{2+x}, in the range $|x| < 0.065$. These extrema of the values of x corresponds to the extrema of the actual off-stoichiometry modeled in our DFT supercells. We regard this range of x as the range in which the assumption of non-interacting defects holds. Typical off-stoichiometries of undoped ZrO_2 fall within the limit of non-interacting defects that we specified. On the other hand, this does not hold for other metal oxides that exhibit higher off-stoichiometries such as CeO_2 and UO_2.

It should be emphasized at this stage that the temperature, the oxygen partial pressure and the electron chemical potential are not independent variables. Indeed, specifying two of them is, in principle, enough to determine the third.

3.2.3 Finite temperature effects

A major challenge that confronts bringing the DFT calculations (at 0 K) closer to the realm of experimental conditions is capturing the finite temperature effects. Ignoring these effects can lead to results that are far from being quantitative [96]. The major difficulty in capturing these effects is that they are typically very expensive computationally. In our modeling of defect equilibria in tetragonal zirconia we found out that the free energy of phonons and the electronic entropy have important quantitative contribution. This is the case especially because the undoped T-ZrO_2 is stable at very high temperatures. In this subsection we examine these finite temperature effects. For monoclinic zirconia we only considered the phonon free energy and discarded the electronic entropy (to reduce the computational cost).

We illustrate these finite temperature effects on the neutral oxygen vacancy in T-ZrO_2 as an example here (The same approach and analysis are applicable to all the other defects to monoclinic zirconia of course). The creation of this defect is associated with a change in the vibrational free energy of the system, ΔF_{vib}, that can be written as:

$$\Delta F_{vib} = F_{vib}^{defected} + F_{vib}^{O} - F_{vib}^{perfect} \tag{3-9}$$

The vibrational free energy of the oxygen atom in the gas phase, F_{vib}^{O}, is already included in the chemical potential term for the oxygen atom in the gas phase, μ_O. What is typically neglected in defect calculations are the vibrational free energies of the perfect crystal, $F_{vib}^{perfect}$, and the defected crystal, $F_{vib}^{defected}$. We accounted for these two terms within the harmonic approximation as follows:

$$F_{vib}^{solid} = Nk_BT\int_0^\infty g(\omega)\ln\left[2\sinh\left(\frac{h\omega}{4\pi k_BT}\right)\right]d\omega, \tag{3-10}$$

Where N is the number of degrees of freedom, ω is the phonon frequency, $g(\omega)$ is the phonon density of states, h is Planck's constant.

Similarly a change in the electronic entropy occurs in the system upon creating a neutral oxygen vacancy as follows:

$$\Delta S_{elec} = S_{elec}^{defected} + S_{elec}^{O} - S_{elec}^{perfect} \tag{3-11}$$

The electronic entropy for the oxygen atom in the gas phase, S_{elec}^{O}, is already accounted for in the chemical potential term for the oxygen atom, μ_O. However, it is common to neglect the electronic entropies of the perfect crystal, $S_{elec}^{perfect}$, and the defected crystal, $S_{elec}^{defected}$. In fact the electronic entropy for a wide band gap perfect crystal is negligible. However, if a point defect was introduced in the crystal and this defect subsequently introduced electronic states in the band gap, then the electronic entropy contribution of these states can be significant [97] The electronic entropy for a solid crystal was calculated as follows [95, 98]:

$$S_{elec}^{solid} = -k_B\int_{-\infty}^{\infty} g(E)[f\ln f + (1-f)\ln(1-f)]dE, \tag{3-12}$$

where $g(E)$ is the electronic density of states and f is the Fermi-Dirac distribution which is a function of temperature, energy and the chemical potential of electrons. It is worth noting that all the temperature dependence of S_{elec}^{solid} is embedded in the Fermi-Dirac distribution since we neglected the temperature dependence of the electronic density of states. An accurate determination of the temperature dependence of $g(E)$ is still beyond the current computational capabilities. However, in the Results and Discussion section we present Kröger-Vink diagrams calculated at different band gaps and thus indicating how the reduction of the band gap, which is the main impact of temperature on $g(E)$ [99], can alter the defect equilibria.

In Figure 3-1(a), we plotted the correction to the free energy of formation of the neutral oxygen vacancy due to the phonon vibrational contribution in the solid ($F_{vib}^{defected} - F_{vib}^{perfect}$) and the electronic entropy contribution in the solid ($-T(S_{elec}^{defected} - S_{elec}^{perfect})$). Both the temperature and oxygen partial pressure dependence of these corrections are also shown in the figure. It is clear that phonons add a significant quantitative correction to the free energy of formation especially at the very high temperatures. This correction is further amplified by the exponential dependence of the defect concentration on the free energy of formation. Within the assumptions adopted here, the phonon correction is independent of the variation of P_{O_2} on an isotherm. Quantitatively the correction due to the change of the electronic entropy of the solid is not as significant as that of phonons. However on an isotherm, this correction exhibits an interesting dependence on P_{O_2} that originates from the $-TS_{elec}^{defected}$ term. As will be shown in section 3.2 , at $P_{O_2} = 1$ (atm) the chemical potential of electrons μ_F is located almost at the middle of the band gap. Then by lowering P_{O_2} it starts moving up towards the conduction band edge. Once μ_F reaches a value of about 2.6 eV (i.e. coincident with the defect state shown in Figure 3-1(b)) it resonates with a defect-induced state in the band gap and as a result the electronic entropy is enhanced and this leads to the minima observed in Figure 3-1(a). The role of electronic entropy in defect equilibria is not well-studied particularly in non-metal systems. The insights that we demonstrated here conveys an important message that whenever a defect state arises in the band gap within the reach of μ_F, the electronic entropy contribution should be assessed carefully.

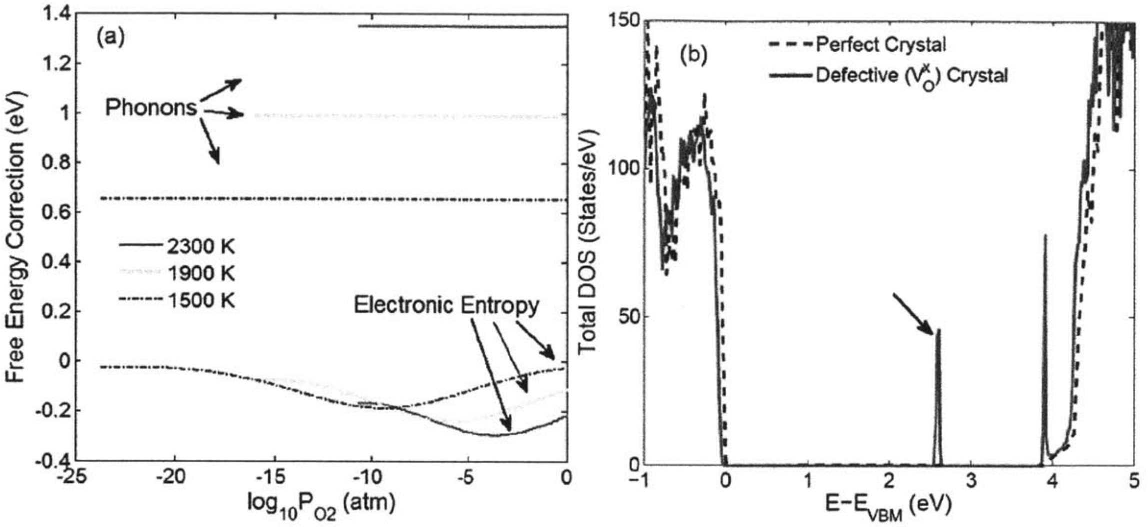

Figure 3-1: (a) Corrections to the free energy of formation of the neutral oxygen vacancy due to the change in the phonon vibrations and the electronic entropy in the solid. (b) The total electronic density of states (DOS) for tetragonal ZrO_2 in a perfect supercell and in a supercell with a neutral oxygen vacancy. The arrow in (b) indicates the electronic state in the gap due to the neutral oxygen vacancy that enhances the electronic entropy of the defect. The position and magnitude of the resonance (in (a)) between μ_F and the defect state (in (b)) depends on temperature and oxygen partial pressure.

3.2.4 Density functional theory calculations

Density functional theory calculations were performed using the projector-augmented plane-wave method [100] as implemented in the Vienna Ab-initio Simulation Package (VASP) [101-104]. Exchange-correlation was treated in the Generalized Gradient Approximation (GGA), as parameterized by Perdew, Burke, and Ernzerhof (PBE) [105, 106]. In this work we chose to apply standard PBE instead of a hybrid functional that incorporates a fraction of the exact exchange interaction for the following reasons. First, typical practice of using hybrids requires a precise knowledge of the band gap in order to choose a fraction of the exact exchange that reproduces the priorly known band gap. In the case of ZrO_2 the reported values of the band gap are widely scattered [107, 108] to be useful while choosing the exact exchange fraction. Second, zirconium oxide is not among the family of strongly correlated metal oxides [109] and hence standard PBE is able to reasonably describe this system. Third and most importantly, the picture that hybrid functionals can act as *the* norm, to which the errors in standard PBE predictions can be referenced, has been recently challenged by Ramprasad et al [110]. Those authors demonstrated that while standard PBE underestimates quantities such as the valence band width and the formation energies with respect to accurate experimental determination, hybrid functionals overestimate these quantities. Fourth, a major goal in the current work is to emphasize the contribution of finite temperature effects (in particular phonons and electronic entropy) to the defect equilibria in metal oxides. At the temperatures of interest in this work, these effects can be more dominant compared to any error due to standard PBE band gap issues. In addition, evaluating these finite temperature effects using hybrid functionals is too expensive computationally and is not anticipated to be more accurate than standard PBE as they tend to overestimate the vibrational frequencies [111].

For zirconium the $4s^2\ 4p^6\ 4d^2\ 5s^2$ electrons were treated as valence electrons. For oxygen the $2s^2\ 2p^4$ electrons were treated as valence electrons. These electrons were represented by a set of plane waves expanded up to a kinetic energy cutoff of 450 eV. The error in the total energy with respect to calculations performed using a kinetic energy cutoff of 600 eV was found to be less than 5 meV per chemical formula. Bulk point defect calculations were performed in a supercell that is $2\times2\times2$ of the conventional unit cell. The later has 4 zirconium cations and 8 oxygen anions for both tetragonal and monoclinic zirconia. A $2\times2\times2$ Monkhorst-Pack k-point mesh was used to perform reciprocal space integrals. The error in the total energy with respect to calculations performed with a $6\times6\times6$ k-point mesh was found to be less than 1 meV per chemical formula. Gaussian smearing with a smearing width of 0.05 eV was used to accelerate the convergence of the electronic structure. All ionic relaxations were considered converged when the forces on all ions were less than 0.01 eV/Å. For computational efficiency, all calculations were done initially by seeking a net zero magnetic moment solution and after convergence, spin polarized calculations were performed on the pre-converged structure.

Single defects were introduced in the super cell one a time. No defect-defect association was considered as the equilibrium concentrations of all defects in undoped tetragonal zircnoia are expected to be dilute. We considered oxygen vacancies with charge states from 0 to 2+, oxygen interstitials with charges from 2- to 0, zirconium vacancies with charges from 4- to 0 and zirconium interstitials with charges from 0 to 4+. Antisites were not considered here as they are expected to have high formation energies in particular for zirconia[24] and in general for all binary ionic materials due to electrostatic considerations [112]. During phonon calculations the electronic structure was sampled using $2\times2\times2$ Monkhorst-Pack k-point mesh for T-ZrO_2 but

$1\times1\times1$ for M-ZrO_2. The monoclinic structure is very asymmetric and it is very expensive computationally to go beyond the gamma point sampling in the phonon calculations of this phase.

To calculate the concentration of free electrons and holes and to quantify the contribution of electronic entropy to the free energy of formation of the point defects, the electronic density of states were calculated for the perfect and defected. In these calculations for the tetragonal phase a finer k-point mesh of $7\times7\times7$ centered at the Γ point was used in combination with the tetrahedron method with Blöchl corrections [113]. However, for monoclinic zirconia the electronic entropy was not evaluated but the density of states for the perfect crystal was calculated to evaluate the electron and hole concentrations using a $6\times6\times6$ centered at the Γ point again in combination with the tetrahedron method with Blöchl corrections.

DFT calculations were also performed to account for phonons within the harmonic approximation. According to the symmetry of the supercell, certain atoms in certain directions were displaced twice, backward and forward, a distance of 0.004 Å for T-ZrO_2 and 0.008 Å for M-ZrO_2 and the electronic ground state was calculated. This allowed, utilizing a central finite difference, the construction of the Hessian matrix and the determination of the vibrational frequencies of the system. The code Phonopy [114] was then used to calculate the phonon density of states using 15x15x15 k-point sampling centered at the gamma point.

3.3 Defect equilibria in tetragonal zirconium oxide

This section is presented into four subsections. In the first subsection we discuss the dependence of the formation energies of the charged point defects on the electron chemical potential. In the second subsection, we present our calculated Kröger-Vink diagrams and compare them with conductivity measurements from the literature. In particular, the slopes of the calculated defect concentrations in the Kröger-Vink diagrams are found consistent with the slopes of the total conductance in the conductivity measurements from literature. Hence, our prediction of the predominance of free electrons at low P_{O_2} is consistent with prior experimental conclusion. A key contribution of our DFT-based results is the finding that the doubly charged oxygen vacancies are the dominant defects in the high P_{O_2} regime, where the prior experiments had fallen short of revealing the type and charge state of the predominant defect. In the third subsection we discuss the variations of T-ZrO_2 off-stoichiometry and electron chemical potential with the thermodynamic conditions. T-ZrO_2 was found to be hypostoichiometric in the entire T and P_{O_2} range. Furthermore, the chemical potential of electrons has access to a range of 1.3 eV of the band gap of T-ZrO_2 by a self-doping effect mainly from the doubly charged oxygen vacancies. Finally, we discuss our key observations related to the atomic and electronic structure of the point defects.

3.3.1 Defect formation energies at 0K

Figure 3-2 (a,b,c) is a plot of the formation energies at 0 K (excluding the zero point energy) for all the defects we considered as a function of the electron chemical potential. Part (d) of the figure summarizes the thermodynamic transition levels between the dominant charge states of each defect as extracted from (a,b,c). An important note needs to be clarified for this figure. The formation energies were allowed to take negative values in Figure 3-2. This is not be confused with the fact that the Gibbs free energy of a defective crystal is more negative than that of a perfect crystal at finite temperature [112] since what we plotted in Figure 3-2 is indeed the formation enthalpy of the defects neglecting the pressure-volume term. The enthalpy of formation for a point defect is a positive quantity [88, 112] and this was taken care of while constructing the Kröger-Vink diagram as pointed out in the Theoretical and Computational Approach section.

As was shown previously for T-ZrO_2 by Eichler [26], we found that the oxygen vacancies exhibit negative-U behavior with a U value of –0.037 eV. This behavior indicates that the singly charged vacancies are not stable with respect to the disproportionation reaction into neutral and doubly charged vacancies. We also found out that oxygen interstitials exhibit negative-U behavior with a U value of -0.838 eV. Although the negative-U behavior indicates that the intermediate charge state is never stable thermodynamically, signatures of this banned charge state were observed in electron spin resonance spectra [115] in the context of studying hydrogen defects in wide band gap oxides. This was explained by metastability due to sufficient isolation of the charged defect [115]. However, there is no transparent way to quantify the concentration of the defects that are in a metastable charge state and at any case it is expected that this concentration is less than what would be calculated based on their formation energies. Thus, to simplify the analysis we will assume that the disallowed charge states, $V_O^{\bullet}$ and $O_i^{/}$, always have negligible concentration. If under any circumstances their concentrations increases to a non-negligible level, once equilibrium is reached the majority of these defects will undergo the disproportionation reaction and hence their concentration drops to a very low level again.

The quadruply charged is the predominant zirconium vacancy throughout most of the band gap compared to the other charge states as in part (b) of Figure 3-2. This can be understood on the basis that this is the only charge state for zirconium vacancies that does not lead to the formation of the O^- ion as will be explained in subsection 3.2.4. While O^- is favorable to O^{2-} in the gas phase, the Madelung potential in an ionic crystal favors the O^{2-} ion [116], thus $V_{Zr}^{////}$ is the predominant. On the other hand, zirconium interstitials have in general high formation energies compared to all other native defects as shown in Figure 3-2 (c). Part (d) of the same figure depicts the thermodynamic transition levels of all the native defects. A thermodynamic transition level indicates the value of the electron chemical potential at which the dominant charge state of a defect changes from a value to another. These levels are amenable to experimental determination. Deep levels in the band gap can be measured by deep-level transient spectroscopy (DLTS) experiments, while shallow levels can be determined through temperature dependent Hall measurements [3]. This diagram in Figure 3-2 (d) is more relevant to studying zirconia as a gate dielectric material compared to the traditional Kröger-Vink diagram that is more common in ceramics literature. Furthermore, the thermodynamic transition levels can directly correspond to a separation between two regions in the Kröger-Vink diagram as will be discussed in the next subsection 3.2.2

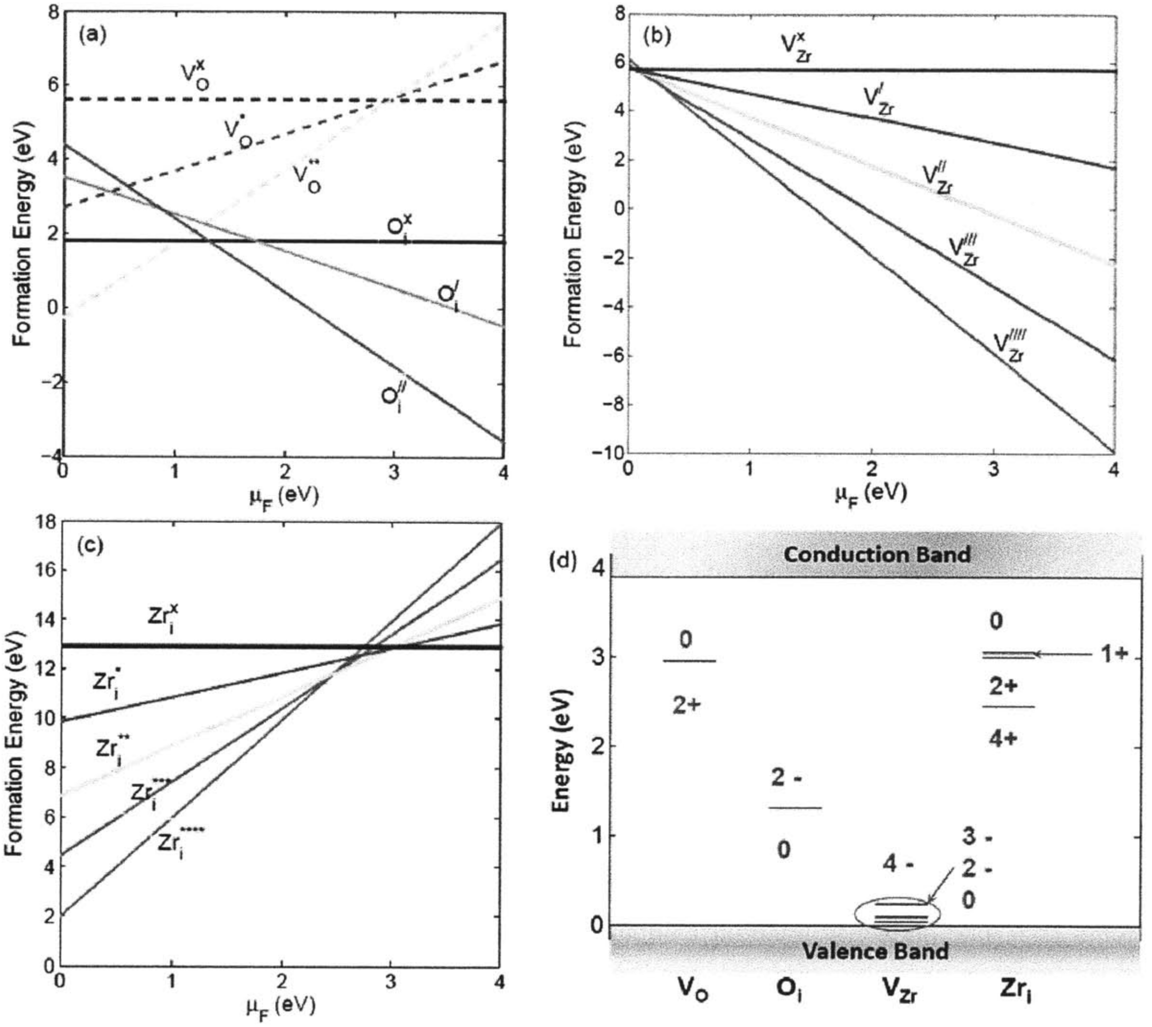

Figure 3-2: Defect formation energies as a function of the electron chemical potential. (a) Oxygen defects. (b) Zirconium vacancies. (d) Zirconium interstitials. (d) The thermodynamic transition levels for the native defects determined from (a,b,c).

We turn now to compare our results of the formation energies with the values available in the literature. The detailed comparison is in Table 3-1. Our results for the oxygen vacancy formation energies are in a good agreement with the DFT calculations of Eichler [26] and of Ganduglia-Pirovano et al [117]. We also have a reasonable agreement with the embedded cluster Hartree-Fock and B3LYP-DFT calculations of Safonov et al [28]. We are not aware of any published electronic structure calculations of defects other than oxygen vacancies in undoped tetragonal zirconium oxide. However, the study of Dwivedi et al. [91] using classical interionic potential considered all fully ionized defects of T-ZrO_2. The predictions of this potential are far from being reasonable and this is expected since a simple pair potential with a fixed charge for each ion is not able to reproduce the complex charged defect structures of zirconium oxide. To the best of our knowledge, the only experimental value of a defect formation energy for undoped tetragonal ZrO_2 is that of the $V_{Zr}^{////} + 2V_O^{\bullet\bullet}$ Schottky defect determined by Wang and Olander [118] They performed a thermodynamic analysis for the thermogravimetric measurements of Xue [119] and obtained a value of 4.12 eV, while we obtained a DFT value of 5.53 eV for the same defect. Although such quantitative discrepancy is common between DFT and experimentally derived formation energies, it is worth mentioning that Wang and Olander relied in their analysis on the assumption that quadruply charged zirconium vacancies has to be the predominant native defect at high oxygen chemical potential to simplify the charge neutrality equation in this regime. The nature of the predominant defect in tetragonal ZrO_2 at high oxygen chemical potential is a long standing controversy in the literature [119, 120], hence such an assumption is definitely questionable. Furthermore, in their analysis, Wang and Olander obtained negative entropy of formation for that particular defect, a result that they suspected in their concluding remarks. We will discuss more the potential origins of discrepancy between DFT calculations and experiments in the next subsection.

Table 3-1: Formation energies in eV of several isolated defects in tetragonal ZrO_2. These values are at zero chemical potential of electrons.

	V_O^x	$V_O^\bullet$	$V_O^{\bullet\bullet}$	$O_i^{//}$	$V_{Zr}^{////}$	$Zr_i^{\bullet\bullet\bullet\bullet}$
This work	5.62	2.68	-0.29	1.79	6.11	1.96
PW91-DFT [26]	5.73	2.55	-0.76	-	-	-
PW91-DFT [117]	5.41-5.92	-	-	-	-	-
Embedded cluster HF and B3LYP DFT [28]	6.1	-	-	-	-	-
Classical potential [91]	-	-	15.62	-10.42	85.04	-67.41

3.3.2 Defect equilibria at finite temperature

In this subsection we discuss the equilibria of the electronic and point defects of tetragonal ZrO_2 utilizing Kröger-Vink diagrams. We further compare our results with the experimental results in the literature that attempted to explain the defect equilibria in tetragonal ZrO_2. We found that our results are consistent with experiments in terms of the predominant defect at low T ($\leq$ 1500K) and low P_{O_2} ($\leq 10^{-6}$ atm). In this regime, both experiments and our calculations confirmed the predominance of electrons followed by the doubly charged oxygen vacancies. There is also consistency between our computational results and experiments in terms of predicting the increase of electronic transference number by elevating the temperature. However, prior experiments could not resolve the type and the charge of the predominant defect at high P_{O_2}. Our DFT calculations were able to uncover the nature of this defect and we found it to be the doubly charged oxygen vacancies at low temperatures and free electrons at high temperatures. Confidence in our conclusions is enhanced by the agreement between the slope of the predominant defect concentration in the calculated Kröger-Vink diagrams and the slope of conductance as a function of P_{O_2} in conductivity experiments [120].

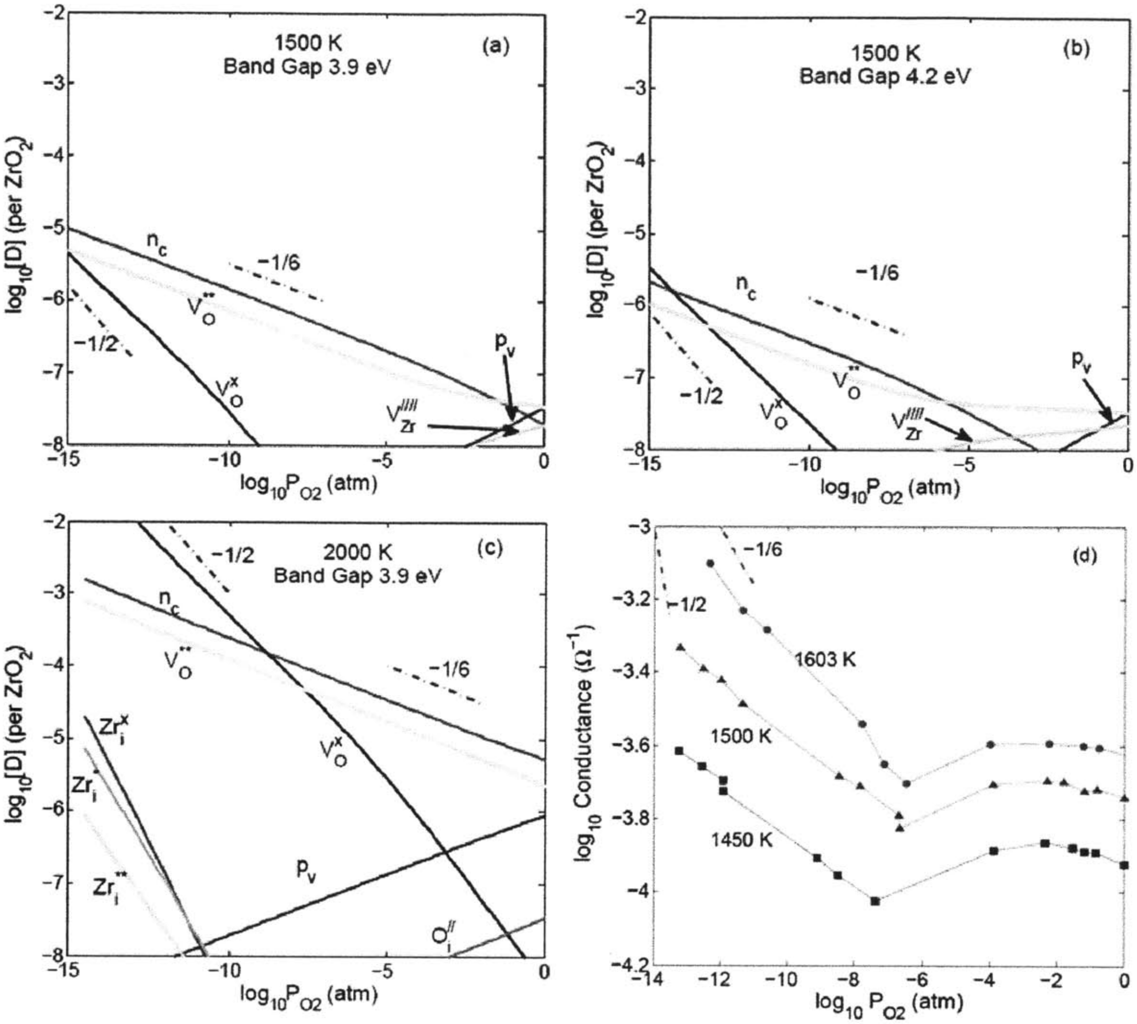

Figure 3-3: Calculated Kröger-Vink diagram for tetragonal ZrO_2 at (a) 1500 K using the DFT predicted band gap of 3.9 eV, (b) 1500 K using the experimental band gap of 4.2 eV, (c) 2000 K using the DFT predicted band gap. (d) Conductivity measurements on tetragonal zirconia by Kofstad and Ruzicka [120]. In a,b,c only the defects that have concentrations greater than 10^{-8} are shown. The dash-dot lines in a,b,c,d are guide for the eye showing the (-1/2) and (-1/6) slopes.

Figure 3-3 (a,c) shows the calculated Kröger-Vink diagrams at 1500 K and 2000 K, respectively using the DFT band gap of 3.9 eV. Part (b) of the figure is the calculated diagram at 1500 K using the experimental value of 4.2 eV [107] and part (d) is a reproduction of the conductivity measurements of Kofstad and Ruzicka [120]. In our calculated diagrams we show only the defects that have concentrations greater than 10^{-8} per ZrO_2 chemical formula. Moreover, we limit the horizontal axis to a range of P_{O_2} that extends from 1 (atm) to 10^{-15} (atm) unless there is no value for the electron chemical potential in the band gap that achieves both charge neutrality and positivity of all formation energies. We chose those two representative temperatures for our calculated Kröger-Vink diagram because they represent two distinct classes, i.e. the low temperature behavior is exemplified by the diagram at 1500K and the high temperature behavior is represented by the one at 2000K. The distinction between the two behaviors is the predominant defect at each regime of P_{O_2} as detailed below. Before discussing the details of the diagrams, we introduce the notation *log₁₀[D]* for log₁₀ of the defect concentration.

3.3.2.1 The Kröger-Vink diagram at 1500 K

The diagram at 1500 K using the DFT band gap in Figure 3-3(a) can be divided into two regions. The first is a high P_{O_2} region that extends from 1 atm up to $10^{-1.4}$ atm in which the doubly charged oxygen vacancies are the predominant defect. In this region charge compensation mainly takes place through the creation of quadruply charged zirconium vacancies and free electrons. The slope of *log₁₀[D]* for the predominant defect in this region is slightly negative but close to zero. This region is characteristic for ionic materials that predominantly form Schottky defects around the stoichiometric composition [88]. The second region extends from $10^{-1.4}$ atm up to 10^{-15} atm and the predominant defects here are the free electrons followed by the doubly charged oxygen vacancies. Charge compensation mainly takes place among these two types of defects and hence their *log₁₀[D]* have a slope of (-1/6) as predicted by applying the law of mass action. This behavior of the concentrations leads to an n-type electric conductivity. It is worth noting that the *log₁₀[D]* of neutral oxygen vacancies grows with a slope of approximately (-1/2) by lowering P_{O_2} in this region until it becomes comparable to the concentration of free electrons. The slope of the *log₁₀[D]* of this defect is roughly independent of the P_{O_2} as it does not participate in achieving charge neutrality. The calculated diagram at 1500 K using the experimental value of 4.2 eV for the band gap is shown in part (b) of Figure 3-3. The same qualitative features described above still apply to this diagram. The major difference is that extending the band gap expands the horizontal region down to $10^{-5.7}$ atm. This is in a better agreement with conductivity measurements shown in part (d) of the figure and discussed below. Increasing the band gap adds a penalty to the process of creating free electrons and holes. Hence the region in which free electrons predominates is delayed until a pressure as low as $10^{-5.7}$ atm is achieved.

3.3.2.2 The Kröger-Vink diagram at 2000 K

Figure 3-3(c) shows the calculated Kröger-Vink diagram at 2000 K using the DFT band gap. The first distinction to note here compared to the lower temperature diagram, is that there are more defects that have concentrations greater than 10^{-8} and this is anticipated as the concentration is temperature activated. Second, there is no region in which $log_{10}[D]$ of the predominant defect has a horizontal slope. This is an indication of an off-stoichiometric composition and indeed it is hypostoichiometric as we elaborate more in the next subsection. However, the diagram can still be divided into two regions. The first region extends from 1 atm to $10^{-8.8}$ atm. In this region the free electrons are predominant followed by the doubly charged oxygen vacancies. Charge compensation takes place mainly among these two types of defects and hence the (-1/6) slope for both of them. It is evident in this region that doubly charged oxygen interstitials have higher concentration compared to quadruply charged zirconium vacancies. This indicates that if tetragonal ZrO_2 were stable at P_{O_2} higher than 1 atm and can approach stoichiometric composition at 2000 K, then it would be an ionic compound in which the intrinsic region around the stoichiometric composition is dominated by oxygen Frenkel pairs. This is a significant difference compared to the finding at 1500 K where the intrinsic region around the stoichiometric composition is dominated by Schottky defects. The second region in the Kröger-Vink diagram at 2000 K extends from $10^{-8.8}$ atm to roughly $10^{-14.5}$ atm. The border between the first and second region is due to the thermodynamic transition level for oxygen vacancies from charge state 2+ to 0 as shown in part (d) of Figure 3-3. As discussed above we did not find a value for the chemical potential of electrons that achieves both charge neutrality and positivity of the formation energies of all defects at pressures lower than $10^{-14.5}$ atm. In this region the neutral oxygen vacancies predominates with $log_{10}[D]$ slope of approximately (-1/2). It is also noticeable that the concentrations of three charge states of zirconium interstitial grow in this region by lowering P_{O_2} but still below the concentrations of oxygen and electronic defects in this region.

3.3.2.3 Comparison with experiments

To compare our theoretical results with the experimental findings in the literature, we show in Figure 3-3(d) the conductivity measurements of Kofstad and Ruzicka [120]. On an isotherm, the defect motilities are constant. Therefore, the $\log_{10}$ of the total conductance of a metal oxide exhibits a slope with P_{O_2} that is governed by the $log_{10}[D]$ slope of the predominant defect. This is what justifies the comparison between our DFT calculated concentrations and the conductivity measurements. The conductivity measurements in Figure 3-3(d) are in a reasonable agreement with our calculated Kröger-Vink diagram at 1500K in terms of exhibiting a slightly negative slope that is very close to zero at high P_{O_2}. At lower P_{O_2} the slope of the $\log_{10}$ of the conductance changes to roughly (-1/6). It is important to note that according to these conductivity measurements, the first horizontal region extends down to 10^{-4} atm and then the (-1/6) starts somewhere between 10^{-6} and 10^{-7} atm depending on the temperature. This is more consistent with our calculated Kröger-Vink diagram using the experimental band gap of 4.2 eV.

The trends exhibited by the conductivity measurements shown here are also obeyed by the conductivity measurements of Vest and Tallan [121]. In addition, thermogravimetric measurements by Xue [119] reproduced the (-1/6) slope at low P_{O_2}. Thus, there is a firm agreement that at low P_{O_2} the predominant defect is free electrons followed by doubly charged oxygen vacancies. However, the experimental efforts could not resolve the nature of the predominant defect at high P_{O_2}. Kofstad and Ruzicka whose results are reproduced in Figure 3-3 (d) suggested that at high P_{O_2} both oxygen vacancies and interstitials are predominant. Authors of Ref. [121] could not deduce the predominant defect at high P_{O_2}. The thermogravimetric measurements of Xue [119] at high P_{O_2} exhibited a positive slope that can be fitted well by either +1/6 ($O_i^{//}$ predominant) or +1/5 ($V_{Zr}^{////}$ predominant) slopes but the latter was chosen to conform to the classical potential predictions of Ref. [91]. As we mentioned above the results of this classical potential are highly unphysical and cannot be used as a support of the nature of charged defects. We believe that the reasonable agreement between our DFT results and the conductivity measurements of Ref. [120, 121] provides a solid ground to propose that this defect is the doubly charged oxygen vacancies at high P_{O_2}.

There is another aspect in which our DFT calculations are consistent with the experiments. We showed that at low temperatures (with respect to the range of stability of T-ZrO_2) the electronic conductivity predominates in the region of low P_{O_2}. At higher temperatures, the electronic conductivity predomination starts at high P_{O_2} and extends over a wide range of P_{O_2}. Measurements of the electronic and ionic transference numbers are consistent with this finding [121, 122].

3.3.2.4 Origins of the gap between theory and experiment

Beyond the finite temperature effects (which we demonstrated in subsection 3.1.3 and incorporated into our analysis), there are several other challenges that obstruct improving the level of agreement between theory and experiments for determining the nature and concentrations of defects at a given thermodynamic state. On the experimental side, impurities are unavoidable and those can significantly affect the conductivity measurements. For example the conductivity measurements of Guillot and Anthony [123] could not resolve the nature of the intrinsic predominant defects in T-ZrO_2 because of the interfering role of impurities. Moreover to the best of our knowledge all the experiments on T-ZrO_2 to understand its defect equilibria were performed on polycrystalline samples. Grain boundaries and the associated space charge zones can significantly affect defect equilibria [112]. Not only the presence of grain boundaries, but also the size of the grains themselves can alter the equilibria [124]. The current DFT computational limits do not allow realistic calculations for charged defect energies at grain boundaries. Another factor that is pertinent to undoped T-ZrO_2 is that it is thermodynamically stable at very high temperatures, which poses limitations on the feasibility and accuracy of the measurements. On the theoretical side, the well-known DFT problem of underestimating the band gap has an exponentially amplified impact on determining the concentration of free electrons and holes, and hence on the overall equilibria of the charged defects. As shown in Figure 3-3 (a,b) applying a rigid shift of 0.3 eV to the conduction band improved the agreement with the conductivity measurements. Applying rigid shifts to the conduction band to match the experimental band gap is a common practice [25, 125]. However, the spread in the experimentally determined band gap values, as in the case of T-ZrO_2 [107, 108], makes it difficult to choose one of these values with confidence. Furthermore, the well-known GGA-DFT issue of over-binding the oxygen molecule introduces an error of about 1.36 eV when using the PBE functional as estimated by Wang et al. [126] by fitting the formation enthalpy of simple non-transition metals to the experimental values. This over-binding impacts the accuracy of determining the chemical potential of oxygen. The outcome of applying such correction is introducing a positive shift to the oxygen molecule energy. Hence, it becomes more favorable to create defects that lead to incorporate more oxygen gas into the solid which are oxygen interstitials and zirconium vacancies. This simultaneously reduces the concentration of oxygen vacancies and zirconium interstitials. In other words, the concentration of the negatively charged point defects increases and the concentration of the positively charged point defects decreases. This, in turn, reduces the concentration of free electrons and increases the concentration of free holes to maintain charge neutrality. Furthermore, the actual value of the correction depends strongly on the DFT simulation parameter. In section 3.6 we evaluate this correction following the approach in Ref. [126] but using the same simulation parameters used in the defect calculations. A value of 1.22 eV was obtained.

3.3.3 Off-stoichiometry and electron chemical potential

The temperature and the oxygen partial pressure are the thermodynamic independent variables that determine the defect concentrations in the stress-free undoped T-ZrO_2 as discussed in the previous subsection. Two other important observables that are determined by T and P_{O_2} are the sample off-stoichiometry, x, and the chemical potential of electrons, μ_F. The former is an integral quantity that represents the collective defect equilibria and can be measured in thermogravimetric experiments [119]. The latter is a fundamental quantity that affects the transport and transfer of electrons, and can be measured in electrochemical impedance spectroscopy experiments [127]. In our DFT calculations, the calculated defect concentrations can be used to compute x and the charge neutrality condition determines the value of μ_F. In this subsection we discuss the relations among T- P_{O_2} -x- μ_F on the basis of our DFT calculations.

Figure 3-4(a,b,c) depicts the relations among T- P_{O_2} -x- μ_F for stress-free undoped T-ZrO_2. Part (a) of the figure shows that the off-stoichiometry of a T-ZrO_2 sample is almost independent of P_{O_2} for several orders of magnitude, and then at a very low P_{O_2} the off-stoichiometry decreases significantly. The P_{O_2} at which |x| (hypostoichiometry here) sharply increases is reduced with increasing the temperature.

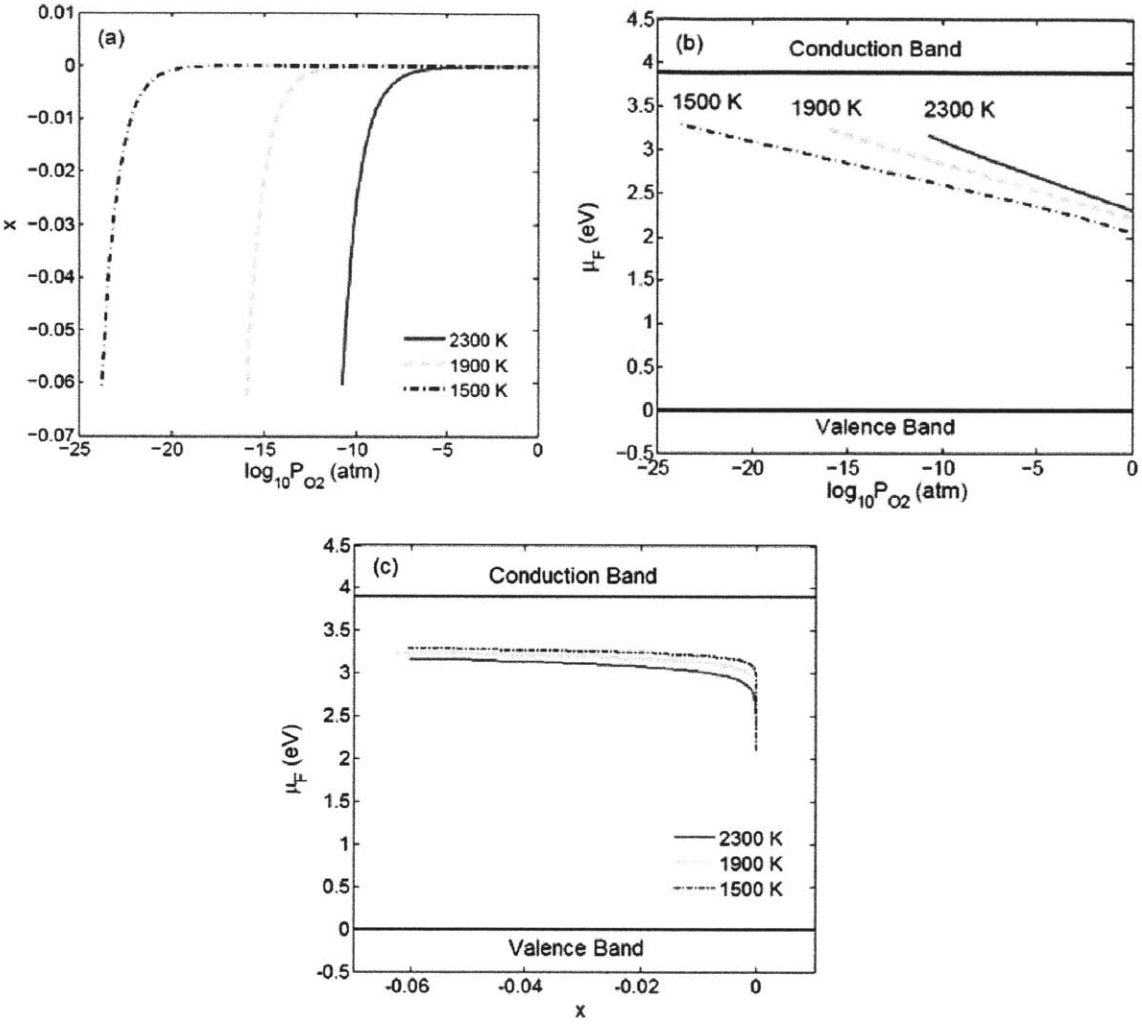

Figure 3-4: (a) Off-stoichiometry in ZrO_{2+x} as a function of the oxygen partial pressure, P_{O_2}, at different temperatures. The dependence of the electron chemical potential, μ_F, on the oxygen partial pressure at different temperatures (b), and on the off-stoichiometry, x, at different temperatures (c).

As shown in the resulting Kröger-Vink diagrams, oxygen vacancies are responsible for the observed off-stoichiometry. This plot indicates also that T-ZrO_2 is always hypostoichiometric in the T-P_{O_2} range considered here, and this is consistent with the experimental results of Carnigila et al [128]. Part (b) of Figure 3-4 shows that at 1 (atm), the chemical potential of electrons μ_F is close to the middle of the DFT calculated band gap. By lowering P_{O_2}, we find that μ_F moves towards the conduction band minimum within a range of about 1.3 eV. This is a self-doping effect due to the native defects particularly the doubly charged oxygen vacancies and consistent with the n-type conductivity identified in the previous subsection. Finally in part (c) of the figure, we plotted the two dependent variables μ_F and x. Close to the stoichiometric composition, μ_F is very sensitive to very small changes in x. A very small change to a hypostoichiometric composition leads to a jump in the electron chemical potential towards the conduction band and then μ_F levels off by further decrease of x. The value of x at which μ_F levels off in part (c) of the figure corresponds the value at which the sharp decrease in the off-stoichiometry takes place in part (a). It is evident from part (c) that the lower the temperature, the greater the maximum achievable electron chemical potential by self-doping.

The chemical potential of electrons in the bulk of a metal oxide controls the transport of electrons [129]. Furthermore the transfer of electrons across interfaces is governed by the matching of μ_F across the interface. These two issues are of great importance in corrosion, catalysis, gate dielectrics and dye-sensitized solar cells among other applications. We demonstrated here that our theoretical approach for defect equilibria in the bulk of a metal oxide consistently determines the value of μ_F according to the surrounding thermodynamic conditions. While we did not address here determining the variations of μ_F across an interface, we believe that our determination for μ_F in bulk zirconia sets a necessary boundary condition needed for the accurate determination of its variations at interfaces with the same approach described here [130, 131].

3.3.4 Defect atomic and electronic structures

So far our discussion of the point defects was based on the energetics. However, we believe that it is also important to elucidate the atomic and electronic structure of the defect. This is because the atomic and electronic characteristics of each defect provide a signature to help in detecting it experimentally. Moreover, these characteristics are needed to understand the transport kinetics of the point defects and their effect on the mechanical properties of the material, and thus, can be important for future work concerned with these defects. In this subsection we describe our key observations related to the atomic and the electronic structures of the major defects that we assessed in the analysis presented above, starting with vacancies and ending with interstitials.

Several experiments and DFT calculations confirmed that oxygen vacancies in all phases of zirconium oxide have the ability to trap electrons forming F-centers [25, 26, 117, 132]. Our calculations are consistent with these prior reports as we observed electron localization on the vacant oxygen site for both V_O^x and $V_O^\bullet$. The ground state for the two electrons localized in the V_O^x defect is singlet. It is energetically very unfavorable for zirconium cations to get reduced to the oxidation state 3+ and hence the electrons get trapped in the vacant site. On the other hand, we observed in our calculations that all zirconium vacancies except $V_{Zr}^{////}$ lead to the formation of the antimorph of the F-center, namely the V-center. In a V-center, a hole gets trapped in an oxide ion that is the nearest neighbor of a cation vacancy. This means that each of the zirconium vacancies other than $V_{Zr}^{////}$ is a cluster of point defects. For example, a more accurate notation for V_{Zr}^x would be $(4O_O^\bullet V_{Zr}^{////})^x$, however, we kept the former as a simplified notation throughout this chapter. As we showed in the previous subsections the V-centers associated with all zirconium vacancies except $V_{Zr}^{////}$ always have a minute concentration.

Our calculations indicate that for the charge states 0 and -1, the <110> split dumbbell is the energetically most favorable structure of the interstitial oxygen. The lengths of the dumbbells are 1.47Å and 1.99 Å respectively larger than our calculated bond length for the oxygen molecule which is 1.23 Å. Examination of the charge the density shows that the charge is almost evenly distributed on the two ions of the dumbbell. Moreover, for the charge state 0, there is a very distinct feature that appears in the phonon density of states which is a characteristic peak at a frequency of 939 cm^{-1}. While this peak is at a frequency much higher than any vibrational mode in the crystal, it is still much lower than 1560 cm^{-1}, our calculated vibrational frequency for the oxygen molecule. On the other hand for the charge state -2 the octahedral site is the most favorable. The strong columbic repulsion does not allow the doubly charged interstitial oxygen ion to have a dumbbell or a crowdion configuration.

3.4 Defect equilibria in monoclinic zirconium oxide

In this section we discuss first the 0K calculated formation energies and then the calculated Kröger-Vink diagrams at finite temperature.

3.4.1 0K formation energies

Figure 3-5 shows the calculated native defect formation energies for monoclinic ZrO_2 (M-ZrO2) as a function of the chemical potential of electrons, μ_F. The latter was allowed to take values between 0 which corresponds to the edge of the valence band maximum and 3.5 eV which is our calculated band gap of M-ZrO_2 using standard PBE functional. The chemical potential of oxygen was set to represent 600K and 1 atm indicating the oxygen rich part of the oxide scale grown in zirconium alloys in the water cooled nuclear reactor. For each defect we exhibit the dominant charge states only. Per ZrO_2 unit formula there are two nonequivalent oxygen sites. One is three fold coordinated and is denoted here by O3 and the other is four fold coordinated and hence the notation O4. In these thermodynamic conditions, $V_{Zr}^{////}$ predominates for most of the values of μ_F as shown in the figure.

We found the oxygen interstitials to exhibit negative-U behavior consistent with GGA calculations of both [25] and [24]. However, oxygen vacancies whether in O3 or O4 are normal positive-*U* defects consistent also with the GGA calculations of Foster et al. [25] and the hybrid functional (HSE) calculations of Lyons et al. [133] but contrary to the finding of Zheng et al. [24]using standard PBE functional. This means that there is a possibility for a magnetic defect to exist in monoclinic ZrO_2 which is $V_O^{\bullet}$, but as we show in the finite temperature subsection below, this only takes place in extreme temperature and oxygen partial pressure[§§].

[§§] The issue of defect-induced magnetism is still under debate for ZrO2 phases. See for example [134] J. Zippel, M. Lorenz, A. Setzer, G. Wagner, N. Sobolev, P. Esquinazi, M. Grundmann, Phys. Rev. B, 82 (2010) 125209.

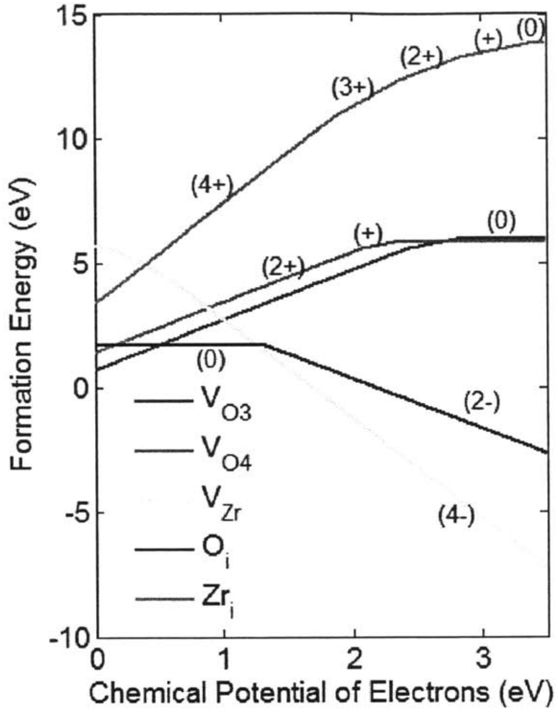

Figure 3-5: Native defect formation energies in monoclinic ZrO_2 as a function of the chemical potential of electrons. The chemical potential of oxygen was set to represent 600K and 1 atm.

3.4.2 Defect equilibria at finite temperature

First we discuss the calculated Kröger-Vink diagram at 1200 K as this sets the ground to compare with experimental attempts to understand the defect equilibria in M-ZrO_2. Next we discuss the Kröger-Vink diagram at 600K which is more relevant to the nuclear reactor operation temperature.

3.4.2.1 The Kröger-Vink diagram at 1200K

Using the correction for O_2 molecule binding energy outlined in section 3.6 at the end of this chapter, we calculated the Kröger-Vink diagram for pure monoclinic zirconia. The result is shown at 1200 K in Figure 3-6. The diagram shows that monoclinic zirconia is amphoteric; exhibiting p-type behavior at high P_{O_2} where free valence band holes are compensated by fully ionized oxygen interstitials, and n-type conductivity at low P_{O_2} where free electrons are compensated by fully ionized oxygen vacancies fist and then at very low P_{O_2} the compensation is by singly charged oxygen vacancies. The transition pressure from p-type to n-type happens to be at 10^{-10} atm at this particular temperature. There is a consensus in the experimental literature on the compensating ionic defect at low P_{O_2}. Both electric conductivity [121, 135] and thermogravimetric [119] measurements suggested $V_O^{\bullet\bullet}$ to be predominant at low P_{O_2} consistent with our results.

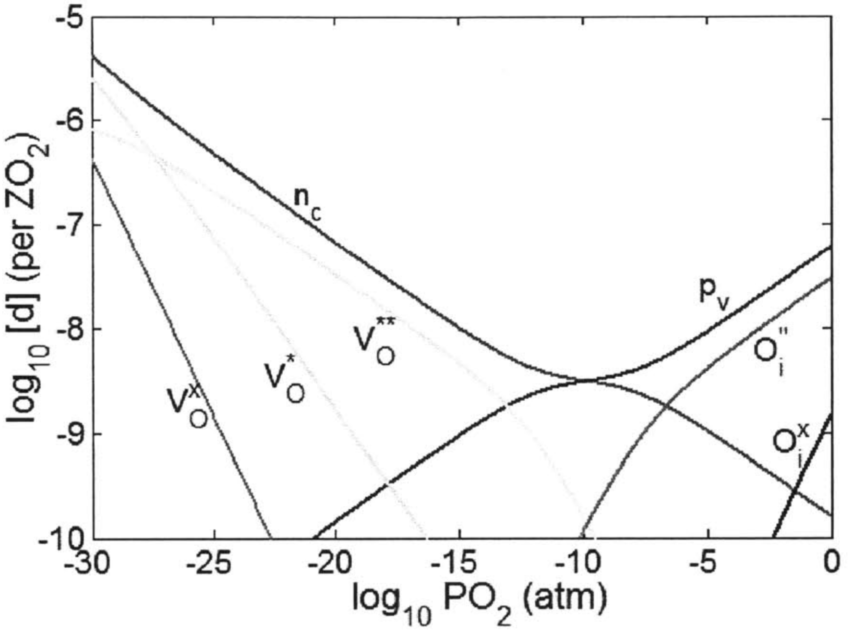

Figure 3-6: Calculated Kröger-Vink diagram for undoped monoclinic zirconia at 1200K.

There is no agreement in the literature on the high P_{O_2} predominant ionic defect. While the experiments of Ref. [119, 121] suggested $V_{Zr}^{''''}$ to be the compensator for the valence band holes, the electric conductivity measurements of Kumar et al. [135] suggested singly charged oxygen interstitials to be the compensator. Our modeling indicate that at high temperature the compensator is O_i'' and low temperature the compensator is $V_{Zr}^{''''}$ and the transition temperature happens to be at 800K.

3.4.2.2 The Kröger-Vink diagram at 600 K

Figure 3-7 shows the calculated the Kröger-Vink diagram at 600K. The equilibria are slightly more complicated here but the amphoteric nature of the oxide is still preserved. At high

P_{O_2} (1-10-8 atom) the free holes are compensated by fully ionized zirconium vacancies. Then from 10^{-8} to 10^{-20} at the fully ionized oxygen interstitials compensate the free holes. At still lower P_{O_2} the compensation mechanism changes to be mutual between free electrons and free holes. Finally the n-type behavior is recovered at very low P_{O_2} where free electron are compensated with fully ionized oxygen vacancies. At such lower temperatures and for undoped zirconia, it is not possible to experimentally determine the underlying defect equilibria and hence our results are more of a prediction in such low temperatures.

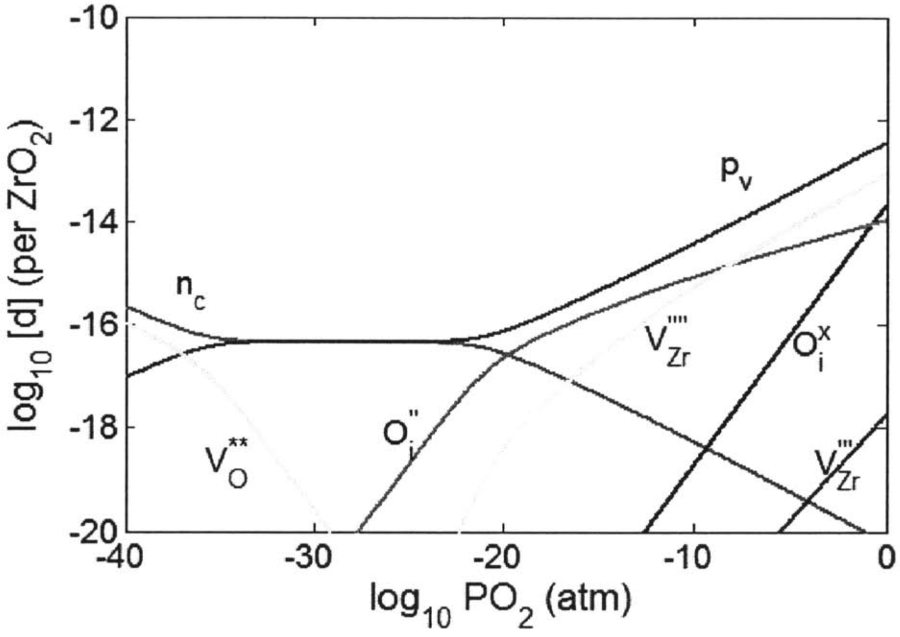

Figure 3-7: Calculated Kröger-Vink diagram for undoped monoclinic zirconia at 600K.

3.5 The accuracy of the Makov-Payne correction

The leading term of the Makov-Payne (MP) correction was shown to overshoot the formation energies of charged defects in some cases [136]. To assess whether this the case for zirconia, we performed a test for this correction scheme on 3 selected defects ($V_O^{\bullet\bullet}, V_{Zr}^{////}, O_i^{//}$) in tetragonal zirconia. Our rationale behind the choice of these defects is that the first is the most predominant; the second represents the highest possible charge state, while the last represents the category of interstitials. As detailed in Ref. [136], the test is conducted by performing finite size scaling correction to the formation energies of the defects and regarding the obtained results by this scheme as the “reference” values. Then the error in MP corrected values in the 2x2x2 super cell used in our work can be evaluated based on the reference values obtained from finite size scaling. While finite size scaling is more robust, it is too expensive computationally and impractical when it comes to studying very large number of defects as in our work. As we demonstrate here, the simple MP correction performs reasonably, especially for the highest charge state ($V_{Zr}^{////}$) and thus it was adopted throughout this work for all the defects.

To perform finite size scaling on the three selected defects, we calculated the formation energies using 4 supercells for each defect. Table 3-2 summarizes the relevant details for each supercell.

Table 3-2: The details of the supercells used to perform finite size scaling on the native defects of tetragonal zirconia.

Number of T-ZrO_2 conventional unit cells	1x1x1	2x2x2	3x3x3	4x4x4
Number of atoms	12	96	324	768
k-points	4x4x4	2x2x2	2x2x2	2x2x2
Kinetic energy cutoff	450 eV			

For each defect the reference formation energy E_{∞}^{f} (which is essentially the energy that would be obtained if the supercell size is infinite) is obtained by fitting the 4 supercell results using the following equation [136]:

$$E^{f}(L) = E_{\infty}^{f} + \frac{a}{L} + \frac{b}{L^{3}}, \qquad (3\text{-}13)$$

where $E^{f}(L)$ is the uncorrected formation energy of the defect calculated from a supercell of length L which is defined as the cubic root of its volume. E_{∞}^{f}, a, and b are obtained from the fitting. In the following figure, we present the uncorrected, MP-corrected and the fitted equation for the formation energies (at zero chemical potential of electrons) for the selected defects. The first thing to observe from the figure is that the MP correction does not overshoot the formation energy even for the smallest supercell (12 atoms). Second the analytic form of the above equation fits well the DFT data indicating the correct dependence on L and the adequacy of two L-dependent terms (no higher orders are needed).

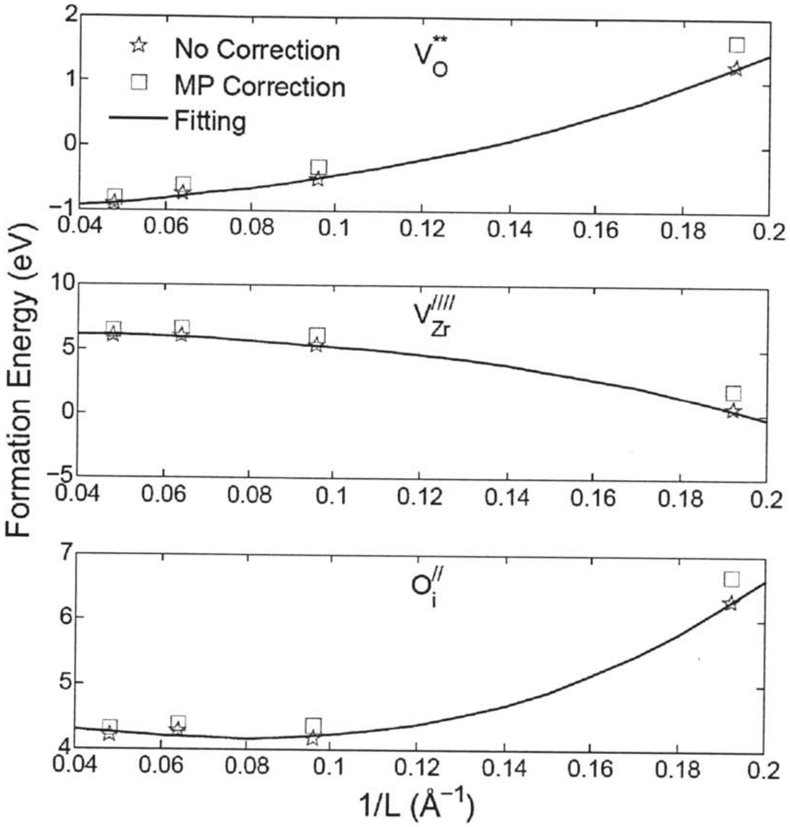

Figure 3-8: Scaling of the relaxed defect formation energy energies. The fitting is according to equation (3-13) using the four points that have no correction.

In Table 3-3 we summarize the "reference" formation energies (E_∞^f) along with the MP-corrected and the uncorrected values in units of eV. The error in the latter two was calculated with respect to E_∞^f. Clearly the MP correction is performing reasonably well and significantly improves the raw uncorrected result and brings it closer to the "reference" value for the highest charge state ($V_{Zr}^{////}$). Moreover adding the MP correction yields better results compared to the raw uncorrected results except for the doubly charged oxygen vacancy.

Table 3-3: Summary of the values of the formation energies of the defects at zero chemical potential of electrons

	Reference value obtained by finite size scaling	Raw results without correction (error)	Makov-Payne results (error)
$V_O^{\bullet\bullet}$	-1.16	-0.52 (0.64)	-0.33 (0.83)
$V_{Zr}^{''''}$	6.29	5.27 (-1.02)	6.06 (-0.23)
$O_i^{''}$	4.62	4.16 (-0.46)	4.35 (-0.27)

3.6 Correcting the O_2 molecule overbinding

For the simulation parameters and DFT functional used throughout this work, we fit a correction for O_2 molecule overbinding following the approach outlined in Ref. [126]. As discussed by Wang et al. [126] this error is not limited to the strongly correlated transition metal oxides, but it is also relevant to non-transition metal oxides (even semiconductor oxides). Table 3-4 summarizes the oxides that were used in the fitting and the evaluation of the overbinding. These particular oxides were chosen as they are related to the study presented in chapter 8 on the effect of 3d transition metals on zirconium alloys hydrogen pickup. Figure 3-9 shows the comparison between the calculated formation energies using DFT and the experimental formation enthalpies at room temperature taken from Ref. [94, 137]. As shown in the figure a shift of 1.22 eV is needed to bring the best line fit for the calculated values to the line that corresponds to the perfect matching with the experimental enthalpies. The shift we obtained is close to the value of 1.36 evaluated by Wang et al. [126] and the small difference is due to the difference in the set of oxides used and most importantly due to the different simulation parameters (such as the kinetic energy cutoff and k-space sampling).

Table 3-4: Crystal and magnetic structure for the oxides used in evaluating the oxygen overbinding.

Reference Oxide	Crystal Structure of the Oxide	Magnetic Structure
ZrO_2	$P2_1/c$ (baddeleyite)	-
Sc_2O_3	$Ia\bar{3}$ (bixbyite)	-
TiO_2	$P4_2/mnm$ (rutile)	-
V_2O_5	$Pmmn$	-
Cr_2O_3	$R\bar{3}c$ (corundum)	Antiferromagnetic
MnO_2	$P4_2/mnm$ (rutile)	Antiferromagnetic
MnO	$Fm\bar{3}m$ (rock salt)	Antiferromagnetic
Fe_2O_3	$R\bar{3}c$ (corundum)	Antiferromagnetic
CoO	$Fm\bar{3}m$ (rock salt)	Antiferromagnetic
NiO	$Fm\bar{3}m$ (rock salt)	Antiferromagnetic
Cu_2O	$Pn\bar{3}m$	-
ZnO	$P6_3mc$ (wurtzite)	-
NbO	$Pm\bar{3}m$	-
SnO_2	$P4_2/mnm$ (rutile)	-

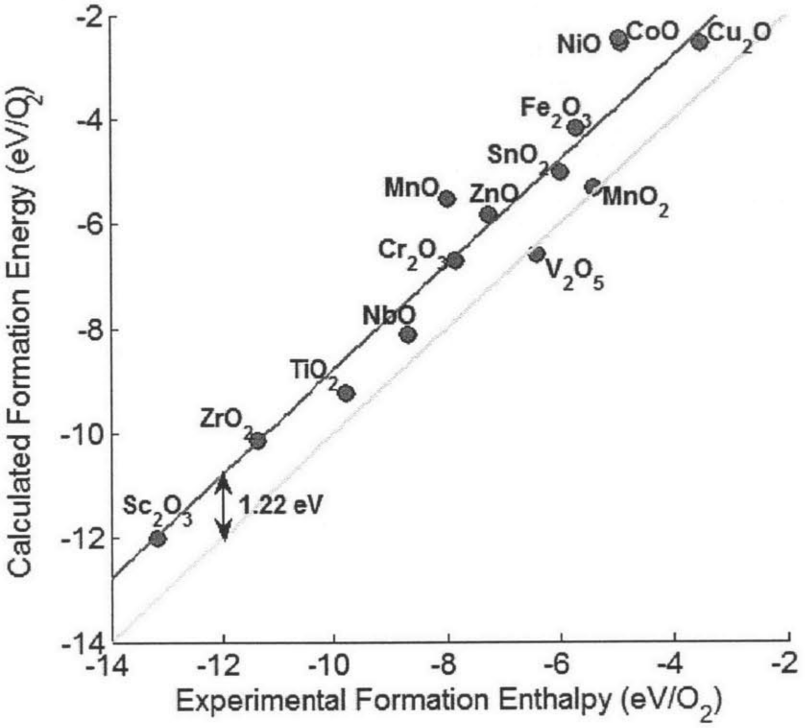

Figure 3-9: Comparison between the calculated formation energy per O_2 for some transition metal oxides and the corresponding formation enthalpies. The latter are adapted from Ref. [94, 137]. The best fit for the computed formation energies is shifted by 1.22 eV from the line that corresponds to the perfect agreement with the experimental enthalpies.

Chapter 4 : Predicting self-diffusion of oxygen in tetragonal zirconium oxide from first principles

Abstract

Theoretical prediction of self-diffusion in a metal oxide in a wide range of thermodynamic conditions has been a long standing challenge. Here we establish that rigorously combining the formation free energies and migration barriers of all charged oxygen defects as calculated by density functional theory within the random walk diffusion theory framework is a viable approach to predict oxygen self-diffusion in metal oxides. We demonstrate this approach on tetragonal ZrO_2 by calculating oxygen self-diffusion as a function of temperature and oxygen partial pressure or alternatively temperature and off-stoichiometry. Arrhenius analysis on the isobaric (or constant off-stoichiometry) self-diffusivities yields a spectrum of effective activation barriers and prefactors. This provides reconciliation for the wide scatter in the experimentally determined activation barriers and prefactors for many oxides.

4.1 Introduction

In this chapter we extend the framework of predicting defect equilibria in metal oxides to account for defect diffusion kinetics as epitomized in the *self-diffusion coefficient*. Self-diffusivities in metal oxides are critical to model processes such as corrosion, crystal growth, sintering and diffusional creep [88]. For zirconium alloys, modeling the growth of the oxide layer requires knowledge of the stoichiometry dependent self-diffusivity of oxygen in the oxide scale. Since the tetragonal phase (T-ZrO_2) is the one that is in the vicinity of the metal it is desirable to obtain the self-diffusivity of oxygen in this phase of the zirconia. Although grain boundary diffusion could be more important to determine, developing the capability to predict the in-lattice bulk diffusion is more reasonable starting point especially that such prediction from first principles is not well-analyzed in the literature as we discuss below.

Experimental determination of self-diffusivities and identifying the mediating defect is a challenging task, and for many oxides there is no consensus neither on the effective activation barriers nor the mediating defect [88, 138]. Theoretical work focused on computing the formation and/or the migration energies of the defects [138-140] However, extending the formation energies to defect concentrations as a function of thermodynamic conditions, which is nontrivial for a metal oxide, and combining them with migration barriers to obtain self-diffusivities has not been accomplished satisfactorily. For example, earlier work had to assume the domination of a certain defect to compute self-diffusivities as a function of the concentration of that particular defect [141]. Recently, self-diffusivity due to neutral oxygen defects in SiO_2 were obtained starting from DFT calculations without prior assumptions about the predominant defect [142]. However, for most oxides charged defects prevail, and their varying and competing concentrations as a function of temperature leads to phenomena such as the non-Arrhenius behavior on diffusivity isobars, which we demonstrate also in this chapter. In Ref. [140] oxygen charged defects were included in computing the isothermal self-diffusivity of oxygen in ZnO. However, the resulting diffusivity was presented as a function of both oxygen and electron chemical potentials. Those results have some validity when the variation in electron chemical potential is due to dopants in dilute solid solutions. However, these two variables are in fact not independent for a fixed composition and at a fixed temperature. Resolving the dependence of electron chemical potential on temperature (T) and oxygen partial pressure (P_{O_2}), enables evaluating the diffusivity as a function of (T) and (P_{O_2}) which are independent variables .

In this chapter, we focus on the diffusion of oxygen since the growth of the oxide scale on Zr alloys proceeds through oxygen diffusion, although the approach is also applicable to cation diffusion. Without prior assumptions about the dominant defect, we employed random-walk diffusion theory, to combine the herein computed migration barriers of oxygen defects with their previously determined concentrations (cf. chapter 3) to obtain oxygen self-diffusivity as a function of T and P_{O_2}. To compare our results to experiments in which oxide off-stoichiometry was fixed [30], we recast the calculated diffusivity in the form of a function of temperature and off-stoichiometry. By performing Arrhenius analysis on both the isobaric and the constant off-stoichiometry diffusivities, two spectra of effective activation barriers and prefactors emerge, providing an explanation for the wide scatter in effective activation energies and prefactors documented in the literature [138, 140].

4.2 Theoretical and computational approach

From random-walk diffusion theory [88, 140], the one-dimensional self-diffusivity of a defect d, is given by

$$D = \frac{1}{2}[d]\sum_{k}\zeta_k \lambda_k^2 \Gamma_k^d, \tag{4-1}$$

where $[d]$ is the defect concentration and the summation is taken over all the crystallographic directions, k, that has a nonzero projection on the one dimension under investigation. For each crystallographic direction k, ζ_k is its multiplicity, λ_k is the length of its projection on the one dimension of interest, and Γ_k^d is the jump frequency of the defect d in the direction k.

In a constant volume ensemble, Γ_k^d is given by [143]

$$\Gamma_k^d = \upsilon_k^d \exp(\frac{-E_k^d}{k_B T}), \tag{4-2}$$

where k_B is Boltzmann constant. For the defect d that jumps in the direction k, υ_k^d and E_k^d are the attempt frequency and the migration energy barrier, respectively. The migration entropy is carried by the term υ_k^d which is taken as 5 THz in this work. By adopting the vectors [100], [010], [001] as a basis for the conventional unit cell of T-ZrO$_2$ and calculating D for each defect in the directions of the basis vectors, we obtained a diagonal diffusivity tensor. Table 4-1 summarizes the multiplicities and projections for the diffusive jumps in T-ZrO$_2$. One needs to not that [100] and [010] are equivalent. Figure 4-1depicts the relationship between the conventional and primitive cells of tetragonal zirconia.

Table 4-1: The Multiplicities ζ_k and projections λ_k for the diffusive jumps in T-ZrO$_2$. We report λ_k in units of the lattice constants of the conventional unit cell (a=b=5.153 Å, c=5.303 Å).

Jump	[100]		[001]	
	ζ_k	λ_k (in units of a)	ζ_k	λ_k (in units of c)
Vacancy				
$<100>$	2	1	-	-
$<001>$	-	-	2	1
$<110>$	2	1	-	-
$<\bar{1}10>$	2	1	-	-
$<101>$	2	1	4	1
$<\bar{1}01>$	2	1	4	1
$<111>$	8	1	8	1
Interstitial				
2.44 Å	$4\times(2/3)$	1/2	$4\times(2/3)$	1/2
2.10 Å	$4\times(2/3)$	1/2	$4\times(2/3)$	1/2

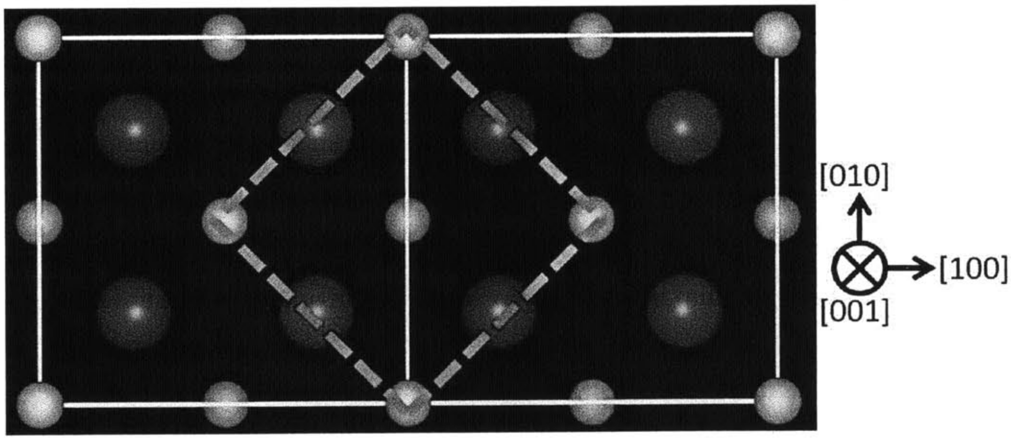

Figure 4-1: Two tetragonal zirconia conventional cells projected on the (001) plane are depicted with their boundaries shown in continuous white line. One primitive cell (projected on the same plane) is also shown with its boundary in dashed blue. The crystallographic directions on the right belong to the conventional cell. Both cells share the [001] vector. Green (small) balls represent zirconium ions and red (large) balls represent oxygen ions. The chemical formula of the conventional cell is (Zr$_4$O$_8$), while that for the primitive cell is (Zr$_2$O$_4$).

The trace of the diagonal diffusivity tensor is the quasi-isotropic self-diffusion coefficient of the defect. By summing the self-diffusivities of all oxygen defects, we obtain the oxygen self-diffusivity, D_O. Including correlation effects to obtain tracer-diffusivity introduces a negligible correction [88, 140]. and is beyond the scope of this work. In what follows all diffusivities are understood as *self.*

In a metal oxide the defect concentration depends on P_{O_2} and so does the defect self-diffusivity. In chapter 3, we determined the P_{O_2} dependence of defect concentrations utilizing the charge neutrality condition. Here, we evaluated the migration barriers for oxygen defects, and combined their concentrations and migration barriers as indicated in equations (4-1) and (4-2). The oxygen defects considered are $V_O^{\bullet\bullet}$, V_O^x, and O_i''. The singly charged vacancy and interstitial were deemed disallowed by the negative-U behavior and the neutral oxygen interstitial, O_i^x,was found to have very low concentration and hence these defects are not considered here.

The migration barriers were calculated using the climbing-image nudged elastic band method [7] using 3-5 intermediate images. DFT total energies were calculated using the projector-augmented plane-wave method [100] as implemented in the VASP package [101-104]. Other details of the computational method are the same as in chapter 3. The experimental [107] band gap of 4.2 eV was adopted in our calculation of defect concentrations because of better consistency with conductivity measurements in T-ZrO$_2$ as shown in chapter 3.

4.3 The migration barriers of oxygen defects

Table 4-2 summarizes the calculated migration barriers and the corresponding jump distances for all the oxygen vacancies and interstitials considered. For $V_O^{\bullet\bullet}$and V_O^x, we considered all the possible and distinct diffusive jumps within the conventional unit cell. Seven distinct jumps were identified as shown in the table. The DFT results of Eichler [26] who considered the migration of $V_O^{\bullet\bullet}$and V_O^x in only the $<100>$and $<001>$ are in agreement with our calculations.

The V_O^x is an F-center with two electrons localized on the vacant site as shown in chapter 3. Its ground state is singlet. The diffusive jump of an F-center involves two simultaneous events, namely, the jump of a neighboring oxide ion to the vacant site and the transport of the two electrons of the F-center to the new vacant site. For some diffusive jumps, we discovered that the migration barrier is lowered when the two electrons of the F-center form a triplet state (net spin $=2\mu_B$) at the saddle point. In evaluating the overall oxygen diffusivity, we used the lowest migration barriers found for V_O^x along each direction.

Fully ionizing the F-center leads to the formation of $V_O^{\bullet\bullet}$. For the shortest diffusive jumps (along <100> and <001>), the migration barrier of $V_O^{\bullet\bullet}$ is significantly less than that of V_O^x. This is consistent with a common trend identified for the diffusion of F-center in oxides [83] and was explained by the columbic repulsion between the localized electrons and the oxide ion during the hop of V_O^x.

The interstitial O_i'' occupies the octahedral site in the conventional unit cell, eight-fold coordinated by lattice oxygen as shown in chapter 3. We found the migration barrier for the direct diffusive jumps of O_i'' to be very high (> 5eV). Instead, this defect migrates by the interstitialcy mechanism, where the migrating interstitial replaces one lattice oxygen which is then pushed to the next interstitial site. Because of the tetragonal distortion of the oxygen columns in T-ZrO_2, four of the lattice oxygens that coordinate O_i'' are at a distance of 2.44 Å and the other four are at 2.10 Å, hence two distinct interstitialcy migration barriers exist as shown in Table 4-2

Table 4-2: The calculated migration energy barriers (in eV) of oxygen defects in T-ZrO$_2$. The crystallographic directions and the jump distances are based on the perfect conventional unit cell. DFT results from Ref. [26] are shown for comparison. For V_O^x, barriers based on both the triplet (net spin $2\mu_B$), and the singlet ($0\mu_B$) saddle points are shown.

<table>
<tr><th></th><th colspan="7">Jump distance along the given crystallographic direction</th></tr>
<tr><th>Defect</th><th>$<100>$
2.64 Å</th><th>$<001>$
2.65 Å</th><th>$<110>$
3.64 Å</th><th>$<\bar{1}10>$
3.64 Å</th><th>$<101>$
3.30 Å</th><th>$<\bar{1}01>$
4.13 Å</th><th>$<111>$
4.51 Å</th></tr>
<tr><td>$V_O^{\bullet\bullet}$</td><td>0.38</td><td>0.58</td><td>2.64</td><td>3.82</td><td>4.32</td><td>1.79</td><td>3.70</td></tr>
<tr><td>$V_O^{\bullet\bullet}$
Ref.[26]</td><td>0.22</td><td>0.61</td><td>-</td><td>-</td><td>-</td><td>-</td><td>-</td></tr>
<tr><td>$V_O^x(2\mu_B)$</td><td>1.59</td><td>1.24</td><td>2.83</td><td>2.90</td><td>2.16</td><td>3.76</td><td>3.88</td></tr>
<tr><td>$V_O^x(0\mu_B)$</td><td>1.48</td><td>1.65</td><td>3.11</td><td>3.39</td><td>2.34</td><td>3.96</td><td>2.91</td></tr>
<tr><td>$V_O^x(0\mu_B)$
Ref. [26]</td><td>1.35</td><td>1.43</td><td>-</td><td>-</td><td>-</td><td>-</td><td>-</td></tr>
<tr><td></td><td colspan="4">Interstitialcy (2.44 Å)</td><td colspan="3">Interstitialcy (2.10 Å)</td></tr>
<tr><td>O_i''</td><td colspan="4">1.41</td><td colspan="3">0.28</td></tr>
</table>

4.4 Analysis of the self-diffusivity of oxygen in tetragonal zirconia

By combining the migration barriers and the concentrations, we obtained the self-diffusivity of each defect and the total oxygen self-diffusivity, D_O, as a function of T and P_{O_2}. We consider the range 1500 K $\leq T \leq$ 2300 K, in which T-ZrO$_2$ is thermodynamically stable without doping. Figure 4-2 (a,b) is a reproduction of the previously calculated concentrations of all electronic and ionic defects in T-ZrO$_2$ at 1500 K and 2000 K (cf. chapter 3). Figure 4-2 (c,d) shows the calculated diffusivities at the same temperatures. Part (c) is at 1500 K and represents the low T behavior ($T \leq$ 1700K), while pat (d) is at 2000 K and represents the high T behavior. The criterion for this temperature classification is the number of different slopes that $\log D_O$ exhibits as a function of $\log P_{O_2}$. For T-ZrO$_2$ these slopes of $\log D_O$ conform mainly to those of $\log D$ of $V_O^{\bullet\bullet}$ since this defect predominates within a wide range of T and P_{O_2} and also has a low migration barrier along <100>. The exception is at very low P_{O_2} where the contribution of V_O^x to total diffusivity becomes significant.

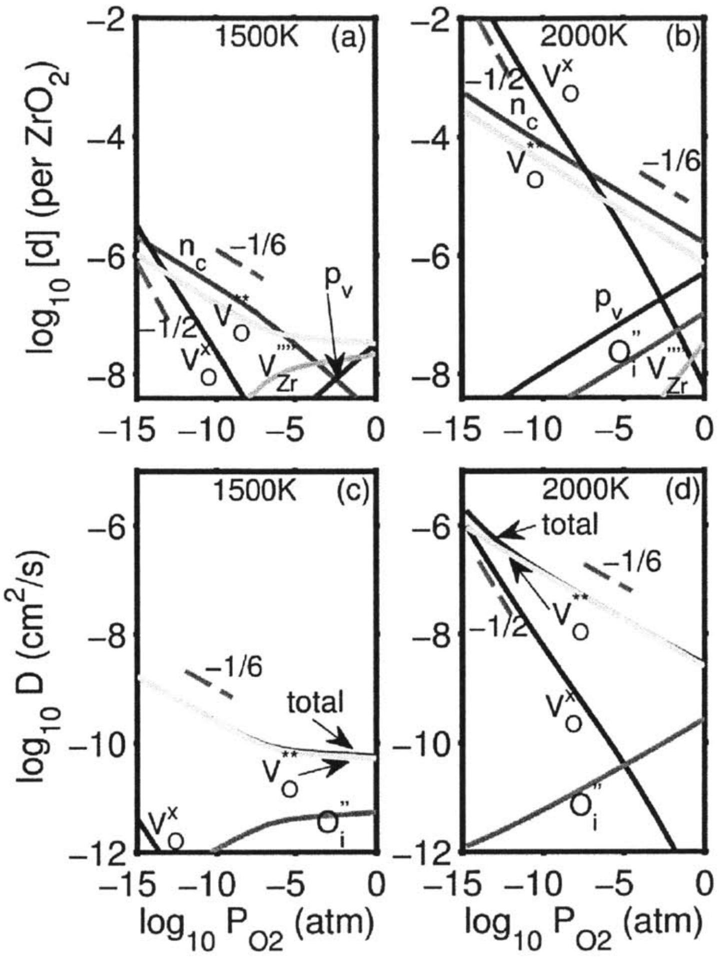

Figure 4-2: (a) and (b) are reproduction of the previously calculated concentrations of electronic and ionic defects at 1500 K and 2000K from chapter 3. Zirconium interstitials are not shown for clarity. Ionic defects are denoted by Kröger-Vink notation, while n_c an p_v denote conduction band electrons and valence band holes, respectively. (c) and (d) depict the calculated self-diffusivities for oxygen defects and the total oxygen self-diffusivity as a function of P_{O_2} at 1500 K and 2000 K.

The low T behavior as in Figure 4-2 (c) is characterized by two main regimes of P_{O_2}. In the high P_{O_2} regime, $V_O^{\bullet\bullet}$ is mainly charge-balanced by the zirconium vacancies, $V_{Zr}^{''''}$. Hence, $\log[V_O^{\bullet\bullet}]$ and consequently $\log D_O$ are roughly independent of P_{O_2} as expected based on the law of mass action combined with the charge neutrality condition ($[V_O^{\bullet\bullet}] \approx 2[V_{Zr}^{''''}]$). In the low

P_{O_2} regime free electrons charge-balance $V_O^{\bullet\bullet}$. Thus, both $\log[V_O^{\bullet\bullet}]$ and $\log D_O$ exhibit a (-1/6) slope in accordance with the new charge neutrality condition ($2[V_O^{\bullet\bullet}] \approx [e']$) and the law of mass action. At very low P_{O_2}, the (-1/6) slope of $\log D_O$ is modified by the contribution of V_O^x. The latter defect is neutral and except for a small electronic entropy contribution (cf. chapter 3), its concentration is not affected by the charge neutrality condition. It follows that $\log[V_O^x]$ has always a (-1/2) slope. In Figure 4-2 (c), V_O^x contribution is not shown as we limited the P_{O_2} axis to 10^{-15} atm to facilitate the comparison with part (d) of the figure. At high temperatures as in Figure 4-2 (d), the zero slope region at high P_{O_2} disappears and the (-1/6) slope for both $\log[V_O^{\bullet\bullet}]$ and $\log D_O$ dominates for most of P_{O_2} values. At very low P_{O_2}, the contribution of V_O^x to diffusion changes the slope of $\log D_O$ to be a weighted average between (-1/6) and (-1/2).

The gradual transition from the low T to the high T behavior is illustrated in Figure 4-3(a), which depicts the isothermal D_O as a function of P_{O_2}. In order to perform Arrhenius analysis and extract an effective activation barrier, we plot in Figure 4-3(b) the isobaric D_O as a function of $1/T$. The hallmark of Figure 4-3(b) is the non-Arrhenius behavior on high P_{O_2} isobars, which do not lend themselves to identifying one effective diffusion barrier over the entire temperature range. The explanation of such non-Arrhenius behavior resides in the different mechanisms of charge neutralization as a function of temperature in T-ZrO_2 introduced above. To rationalize this, imagine an isobaric (e.g. $P_{O_2}=1$ atm) cooling experiment. At high temperatures (T>1700K), $V_O^{\bullet\bullet}$ is charge-balanced by free electrons. Upon cooling, the concentration of $V_O^{\bullet\bullet}$ decreases in an Arrhenius fashion until about 1700 K, below which the charge neutralization mechanism changes to involve cation vacancies such that $[V_O^{\bullet\bullet}] \approx 2[V_{Zr}^{''''}]$. Further cooling continues to decrease $[V_O^{\bullet\bullet}]$ in an Arrhenius fashion but with $(-\partial \log[V_O^{\bullet\bullet}]/\partial(1/T))$ having a value less than the corresponding one at the higher temperatures. This leads to the overall non-Arrhenius behavior over the entire range of temperatures considered here. The low P_{O_2} isobars, on the other hand, have one charge neutrality mechanism ($2[V_O^{\bullet\bullet}] \approx [e']$) for all temperatures shown and hence they conform to the Arrhenius behavior.

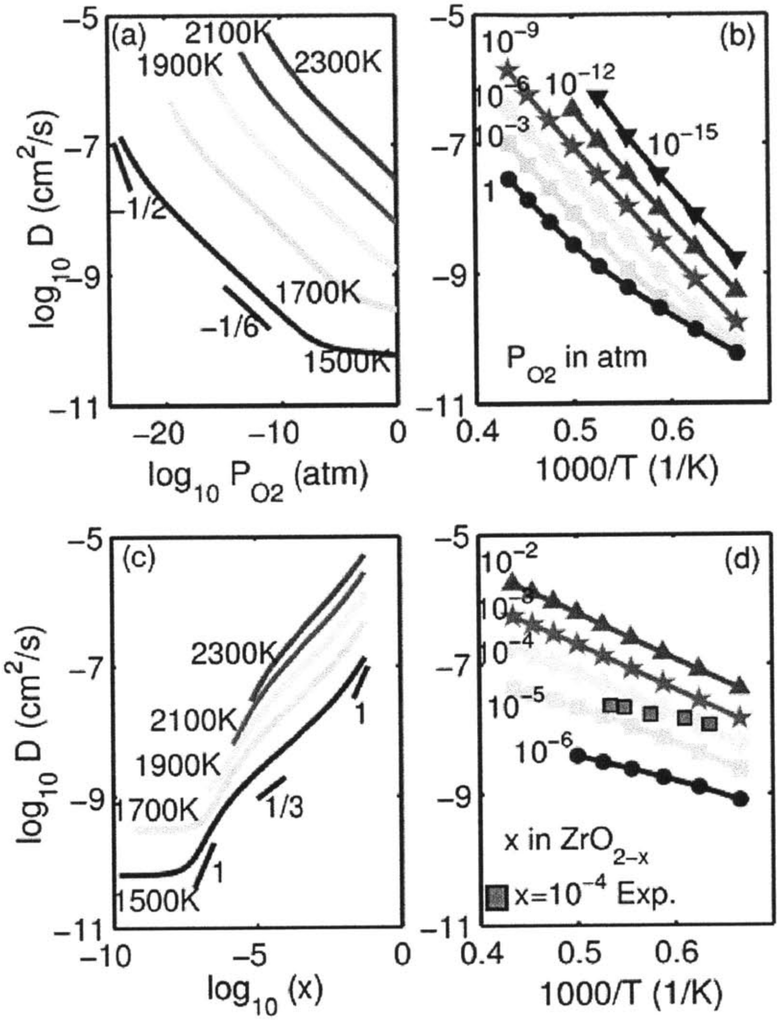

Figure 4-3: (a) Isothermal oxygen self-diffusivities as a function of P_{O_2}. (b) Isobaric oxygen self-diffusivities as a function of $1/T$. (c) Isothermal oxygen self-diffusivities as a function of the off-stoichiometry, x, in T-ZrO$_{2-x}$. (d) Constant off-stoichiometry oxygen self-diffusivities as a function of $1/T$. The experimental data shown in (d), adapted from Ref. [30], are self-diffusivities obtained by scaling the measured tracer-diffusivities by the appropriate correlation factor (of about 0.69) determined in Ref. [30].

To the best of our knowledge, the only experiments in the literature to determine oxygen diffusivity in single crystal undoped T-ZrO$_2$ were performed at constant off-stoichiometry, *x, by* Park and Olander [30]. Maintaining constant off-stoichiometry in the experiments allows probing the migration barrier of the dominant defect that causes the given off-stoichiometry, decoupled from the temperature dependence of the concentration of that defect. To compare with these experiments and to understand the variation of diffusivity with an experimentally accessible quantity, x, we plot in Figure 4-3(c) the isothermal oxygen diffusivities as a function of log$x$ and in Figure 4-3 (d) the oxygen diffusivities at constant off-stoichiometry as a function of *1/T*. The experimental data from Ref. [30] are also shown in part (d) of the figure.

Close to stoichiometric composition and at low T where $V_O^{\bullet\bullet}$ is charge-balanced by $V_{Zr}^{''''}$, $\log D_O$ is roughly independent of x (Figure 4-3(c)). This zero slope region is absent at high T. As the degree of off-stoichiometry increases, the slope of $\log D_O$ increases toward a value of 1 at all temperatures. The value of 1 is what is expected based on equation (4-1) when the off-stoichiometry is attributed solely to $V_O^{\bullet\bullet}$ ($x \propto [V_O^{\bullet\bullet}]$) which is approximately the case when $V_O^{\bullet\bullet}$ is the predominant ionic defect and simultaneously neutralized by free electrons. By continuous deviation from stoichiometry on an isotherm, the slope of $\log D_O$ decreases toward a value of 1/3. In this range of x, V_O^{x} predominates concentration-wise but diffusion is still mainly due to $V_O^{\bullet\bullet}$ because of its much lower migration barrier (see Table 4-2). Thus, the predomination of V_O^{x} leads to the proportionality relation of $x \propto [V_O^{x}] \propto P_{O_2}^{\frac{1}{2}}$, and the fact that $V_O^{\bullet\bullet}$ controls the total oxygen diffusivity leads to, $D_O \propto [V_O^{\bullet\bullet}] \propto P_{O_2}^{\frac{1}{6}}$. Combining these two proportionalities produces $D_O \propto x^{\frac{1}{3}}$, explaining the 1/3 slope. Beyond the 1/3 region, further departure from stoichiometry results in a monotonic increase of the slope of $\log D_O$ toward a value of 1 indicating that $[V_O^{x}]$ reaches to values high enough to surpass the impact of the low migration barrier of $V_O^{\bullet\bullet}$ and hence self-diffusion is dominated by V_O^{x}.

In the experiments of Ref. [30] shown in Figure 4-3 (d) the P_{O_2} was adjusted at each temperature to achieve a stoichiometric composition of T-ZrO_2. However, the inevitable presence of aliovalent cationic impurities in the samples leads to off-stoichiometric composition by $x=10^{-4}$. The level of quantitative agreement in our calculated diffusivity in pure T-ZrO_{2-x} at $x=10^{-4}$ and the measured values in the impurity-containing samples is reasonable. On the other hand, it is not surprising that the experimental data have a different slope (lower effective barrier). The reason is that in the experiments the off-stoichiometry is solely due to $V_O^{\bullet\bullet}$ which is needed to charge-balance the aliovalent impurity cations, while in the simulation of undoped T-ZrO$_{2-x}$ the off-stoichiometry is due to both $V_O^{\bullet\bullet}$ and V_O^x. By consulting Table 4-2 and noting that the easiest migration pathway for V_O^x has a higher barrier than that of $V_O^{\bullet\bullet}$, the different slope of the experimental data compared to simulation can be readily understood.

Using the marked points in Figure 4-3(b), (c) (or similar ones for the not shown isobars and constant x lines), we fit the isobaric and constant off-stoichiometry diffusivities to the Arrhenius relation, $D_{tot} = D_0 \exp(-E_{eff}/k_B T)$. Thus, we obtained an effective activation barrier, E_{eff}, and a prefactor, D_0, as a function of P_{O_2} in Figure 4-4(a) and as a function of x in Figure 4-4(b). For the non-Arrhenius isobars we fit a single activation barrier and prefactor to facilitate the comparison with the Arrhenius ones.

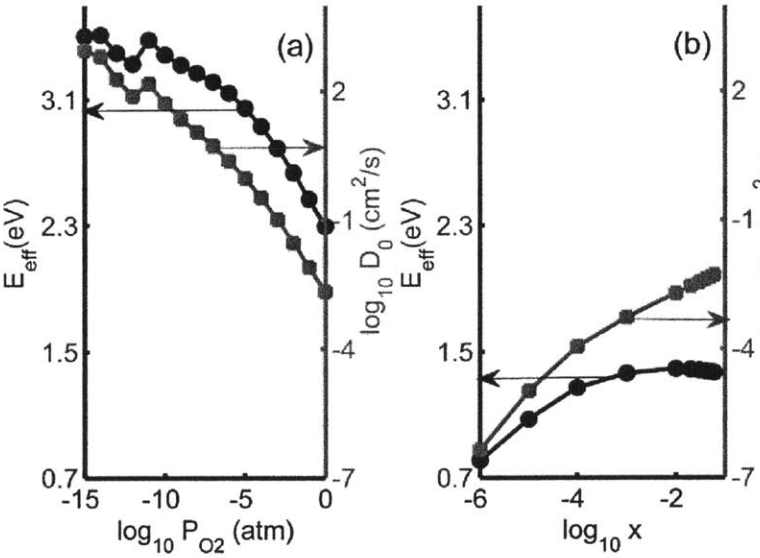

Figure 4-4: The effective activation barrier, E_{eff} (blue circles), and effective prefactor, D_0 (red squares), for oxygen diffusion in T-ZrO$_{2-x}$ as a function of (a) P_{O_2}, and (b) x.

A diffusion barrier evaluated at constant P_{O_2} (Figure 4-4(a)) represents both the formation and the migration of the defects. As P_{O_2} decreases, the oxygen chemical potential decreases, the chemical potential of electrons (Fermi level) increases, and $[V_O^x]$ gradually dominates over $[V_O^{\bullet\bullet}]$. The first factor decreases the formation energy of both vacancies, the second increases the formation energy of $V_O^{\bullet\bullet}$, and the last factor increases the average migration barrier for oxygen. The second and third factors win and we observe in Figure 4-4(a) an increase in the effective activation barrier as P_{O_2} decreases. Moreover, the non-Arrhenius behavior on the high P_{O_2} isobars is reflected in the figure by lowering the effective barrier at high P_{O_2} more than what would be expected by extrapolating from low P_{O_2}.

On the other hand a diffusion barrier evaluated at constant x (Figure 4-4(b)) represents primarily the migration barriers of the defects. Since oxygen in T-ZrO$_2$ diffuses mainly through $V_O^{\bullet\bullet}$ and V_O^x, the effective diffusion barrier at constant x is a weighted average of the migration barriers of these two defects. Close to stoichiometric compositions, $V_O^{\bullet\bullet}$ is predominant and the effective diffusion barrier is relatively low as in Figure 4-4(b). By continuous departure from stoichiometry, V_O^x gradually predominates and the effective diffusion barrier consequently increases until it reaches about 1.4 eV conforming to the lowest migration barrier for V_O^x. Ironically in Figure 4-4 (a,b) the highest values for oxygen diffusivity are coincident with the highest activation barriers emphasizing the importance of the prefactor (affected by the defect concentration) in deciding the magnitude of the overall diffusivity.

4.5 Conclusion

In conclusion, we presented a framework based on random walk diffusion theory to predict self-diffusion in metal oxides, informed by first principles based calculations of defect formation and migration energies. We demonstrated the approach on oxygen diffusion in tetragonal zirconia and validated our results with prior experimental results. Defect concentrations evaluated through charge neutrality condition are combined with defect mobilities within the random-walk diffusion theory. The resultant self-diffusivity is, as expected, a function of two independent thermodynamic variables, either (T, P_{O_2}) or (T, x). Performing Arrhenius analysis on isobaric or constant x diffusivities yields a spectrum of activation barriers and prefactors. We believe that the systematic analysis presented here can reconcile the scatter in the measured self-diffusion activation barriers in many metal oxides such as the 1.9-3.3 eV scatter for zinc diffusion in ZnO [138] or the 0.9-1.3 eV for oxygen diffusion in UO$_2$ [144].

Chapter 5 : The role of defects in the thermodynamics of monoclinic-tetragonal phase transition in zirconium oxide

Abstract

Theoretical consideration of the transition temperature between solid phases focused on the free energy of the perfect crystals of these phases. Here we demonstrate that point defects through their configurational entropy can significantly change the thermodynamic transition. In particular we construct a temperature-oxygen partial pressure phase diagram for zirconia by considering the free energy of the defected tetragonal and monoclinic crystals. The tetragonal phase is shown to admit more defects compared to the monoclinic phases and hence it can be stabilized at temperatures lower than the perfect crystal transition temperature. The latter effect takes place at low oxygen partial pressure. This provides another perspective on the stabilization of the tetragonal phase close to the metal/oxide interface in zirconium alloys.

5.1 Introduction

The tetragonal to monoclinic phase transition plays a crucial role in the transition of the corrosion kinetics of zirconium alloys. As discussed in chapter 2, it is hypothesized in the literature that relieving the planar compressive stress on tetragonal zirconia by the continuous growth of the oxide scale is responsible for inducing the thermodynamic driving force for the phase transition to take place. The implicit assumption here is that planar compressive stress is the stabilizer for tetragonal zirconia in the low temperature[***] of the nuclear reactor. In spite of being a reasonable assumption, there could be other reasons for the stabilization as well. For example, when the alloying elements such as iron and chromium gets oxidized, they get incorporated into zirconia as cations having oxidation state lower[†††] than that of zirconium and so they provide a means to stabilize the tetragonal phase. Here we present another perspective on the stabilization of the tetragonal phase close to the metal/oxide interface. This oxygen poor part of the oxide is rich of defects and in particular oxygen vacancies. We will show in this chapter that ease of creating oxygen vacancies in the tetragonal phase (compared to the monoclinic) phase in the oxygen poor part of the oxide provides a thermodynamic stabilization

---

[***] Low with respect to the stress-free transition temperature (~1440K).

[†††] Confer chapter 8 for detailed analysis of the oxidation states of the alloying elements.

through the configurationally entropy of these defects. In other words, the defects provide a rout for supercooling the tetragonal phase below its perfect-crystal transition temperature. We demonstrate this by constructing a temperature-oxygen partial pressure phase diagram for ZrO_2 based on the on the Helmholtz free energy of the tetragonal and monoclinic phases. For the perfect crystal, the phase diagram collapses into a temperatures-only phase diagram which indeed was computed previously for ZrO_2 [145-147] using density functional theory (DFT). The addition we present here, is that we superimpose the contribution of the defects to the free energy which is dominated by their configurationally entropy, and calculate for the first time a T-P_{O_2} for ZrO_2. To the best of our knowledge, such a temperature-activity diagram has never been theoretically constructed for any material starting from first principles. However, the key underlying idea that the thermodynamic stability of a metal oxide depends on both the temperature and the oxygen activity has been widely used in extracting metals from their ores and is typically depicted in the form of the so-called Ellingham diagrams [148].

The backbone for this work is the calculated Kröger-Vink diagrams for the tetragonal and monoclinic phases presented in chapter 3 as they provide the input concentrations of the defects as a function of T and P_{O_2}. In the rest of the chapter, we summarize the theoretical and computational approach and present the calculated phase diagram.

5.2 Theoretical and computational approach

The point defects in a crystal are stabilized through their configurational entropy which lowers the total free energy of the crystal. If we denote the Helmholtz free energy per chemical formula (ZrO_2) of the perfect crystal by F^0 and denote the same quantity of the defected crystal by F, then the contribution to the free energy of the defected crystal is given by:

$$F - F^0 = \sum_{d,q} [d^q] F^f_{d,q} - TS_{conf}, \tag{5-1}$$

Where $[d^q]$ is the concentration of the defect d whose charge is q. $F_{d,q}$ is the Helmholtz free energy of formation of the defect with charge q, and S_{conf} is the total configurational entropy of the defects. A derivation for how to compute S_{conf} in the limit of non-interacting defects is given in [5]. To perform this computation all what is needed is the concentration of the point defects which were determined for both the monoclinic and tetragonal phases in chapter 3.

To construct the T-P_{O_2} phase diagram, we considered a range of temperatures between 1300-1800K and a range of oxygen partial pressure between 1-10^{-30} atm. At each point of the phase diagram, we computed the Helmholtz free energy of both the defected tetragonal and monoclinic phases according to equation (5-1). The phase that has the lower free energy was deemed to be the one that this stable at this point of the diagram. At any point of the diagram (especially at low P_{O_2}), if any of the phases has a defect that has a negative formation energy, then we designate this point of the diagram is "unexplored zone". More about this zone will be discussed in the subsequent section.

In this study we did not apply any correction to the defect energies except for the Makov-Payne correction. In other words, no band shifts or correction for the over binding of the O_2 molecule was considered for this study. The purpose was to remove any empiricism especially that we are not after accuracy in this study; instead we would like to highlight the major role that the defects can play in changing the thermodynamic stability of metal oxides.

All the calculations details are the same as in chapter 3 except one point related to equation (3-4). This equation relates the chemical potential of oxygen and its partial pressure and it requires as an input the reference value $\mu^0_{O_2}(T,P^0)$. In chapter 3, we used the values of $\mu^0_{O_2}(T,P^0)$ tabulated in the thermochemical tables [94]. The resolution of this tabulation is 100K which is not convenient for the construction, so we appealed to the statistical mechanical formulation for an ideal di-atomic molecules (see for example [149] for the theoretical treatment and [150] for an example application to defects in metal oxides) as shown in the following equation:

$$\frac{\mu^0_{O_2}(T,P^0)}{k_B T} = \ln\left(\frac{P^0 \lambda^3}{k_B T}\right) - \ln\left(\frac{2I k_B T}{\sigma \hbar^2}\right) + \frac{1}{2}\hbar\omega_0 + \ln\left[1 - \exp\left(\frac{-\hbar\omega}{k_B T}\right)\right] \qquad (5\text{-}2)$$

where as before k_B is Boltzmann constant and P^0 is a reference pressure which is taken 1 atm. λ is de Broglie thermal wavelength, I is the moment of inertia of the O_2 molecule, σ is a symmetry factor which is 2 for O_2 molecule, $\hbar$ is the reduced Planck's constant, and ω is the DFT calculated vibrational frequency of the O2 molecule which was found to be 1560 cm^{-1}. A comparison between the prediction of equation (5-2) and the thermochemical tables is shown in Figure 5-1. It is clear that the agreement is good at low temperatures, but at high temperatures the predictions of equation (5-2) deviate due to the assumptions of harmonic and rigid-rotator molecule which are not accurate at high temperature.

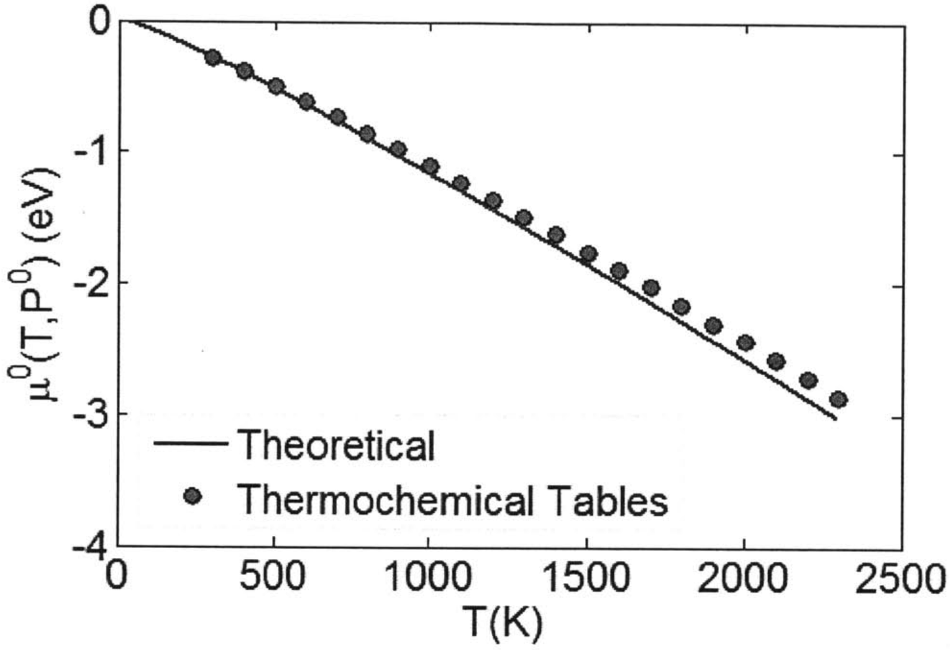

Figure 5-1: Comparison between the theoretical calculation of the reference chemical potential of the O2 molecule using the statistical mechanical formulation of ideal di-atomic molecules and the tabulated values from thermochemical tables [94].

5.3 The tetragonal-monoclinic phase transition temperature

In Table 5-1 we present a comparison between our calculated value for the tetragonal-monoclinic transition temperature based on the Helmholtz free energy of the perfect crystal and previous theoretical calculations. In addition we show in the table two experimental reports for the transition temperature representing the lower limit 1395 K and the upper limit 1478K. The value we obtained using a GGA (Generalized Gradient Approximation) functional and the harmonic approximation is 1790K which is too high than the experimental report. The main reason behind this disagreement is that at such high temperatures anharmonic effects are very important to get accurate results. In Ref. [147] the authors used a GGA functional as well, but they improved by treating lattice vibrations using a quasi-harmonic approximation and obtained a value of 1350K close to the experimental determination. This supports what we asserted above that the missing ingredient is to take into account the anharmonicity of phonons. We believe that the reasonable agreement between prior LDA calculations (reported in the table) combined with the harmonic approximation and the experimental determination is fortuitous. Explicit treatment of the anharmonic effects is needed to obtain physically justified accurate results. However, as we stated above our goal here is not to achieve the highest possible accuracy, instead highlighting the role of the defects is what we seek.

Table 5-1: Comparison between the theoretical calculations and the experimental determination of the thermodynamic transition temperature between the monoclinic and tetragonal phases.

	Energy Cutoff (eV)	Zr Valence Electrons	DFT functional	Approximation	Transition Temperature (K)
Ref. [145]	494.5	4	LDA	Harmonic	1560
[146]	800	4	LDA	Harmonic	1560
[147]	500	12	GGA-PW91	Quasi-Harmonic	1350
This work	450	12	GGA-PBE	Harmonic	1790
Experiment Ref. [151]	-	-	-	-	1478
Experiment Ref. [152]	-	-	-	-	1395

Figure 5-2 shows that main result of this chapter; that is a temperature-oxygen partial pressure phase diagrams based on considering the Helmholtz free energy of the tetragonal and monoclinic phases of zirconia. At high P_{O_2} where the concentration of all defects is negligible (cf. the Kröger-Vink diagrams in chapter 3), the transition temperature does not change compared to the result based on the perfect crystal free energy which is 1790K. As P_{O_2} is reduced the concentrations of the defects and in particular oxygen vacancies increase. However, it turns out that the tetragonal phase admits more defects compared to the monoclinic phase and hence the configurational entropy of these defects lowers the free energy of the tetragonal phase. The net effect is that there is a region of the diagram below 1790 K where the tetragonal phase is stabilized by the configurational entropy of its oxygen vacancies.

The region of the diagram designated as "unexplored zone" requires more analysis if one desires to elucidate the phases that dominate in it. By more analysis we mean taking into account the cubic phase of zirconia, the solid solution of oxygen dissolving in zirconium metal and any zirconium sub-oxide. Indeed even the boundary between the region of the tetragonal phases and the "unexplored zone" should not be considered strictly correct. Close to that boundary the concentration of the defects increases significantly to the extent that the dilute limit assumption does not hold anymore.

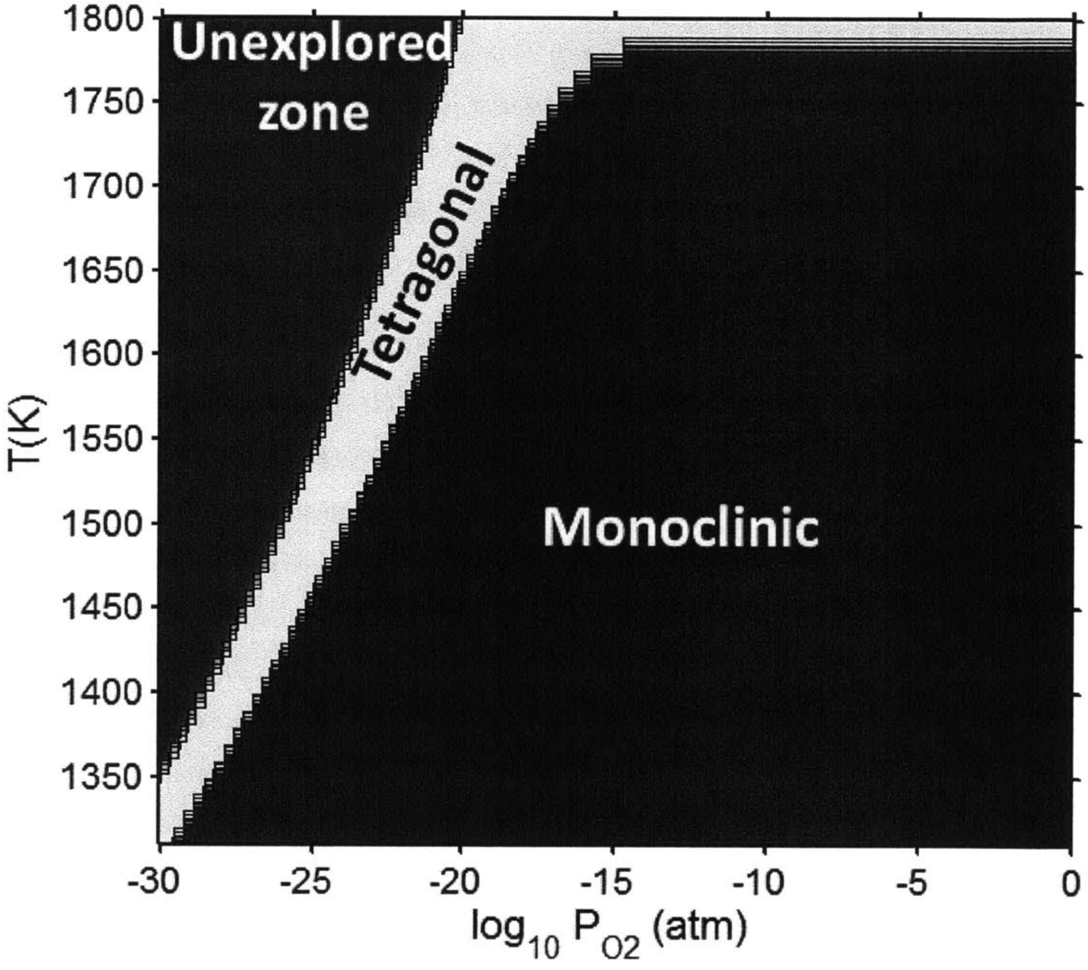

Figure 5-2: The calculated temperature-oxygen partial pressure phase diagram for ZrO_2.

Based on this result we suggest that the fact the chemical potential of oxygen is low close to the metal/oxide interface in an oxide scale grown on zirconium alloy, is a contributing mechanism to the stabilization of the tetragonal phase at lower temperatures.

Chapter 6 : Hydrogen defects in tetragonal zirconium oxide

Abstract

In the energy-structure paradigm, we analyzed the defects that can arise in tetragonal zirconium oxide (T-ZrO_2) involving the hydrogen atom and the hydrogen molecule using density functional theory. Our results indicate that the dominant hydrogen defect in reducing conditions is $H_O^{\bullet}$, a complex formed between the hydride ion and a doubly charged oxygen vacancy. This result is consistent with the experimental observation that in reducing conditions, the solubility of hydrogen is proportional to the degree of hypostoichiomtery of T-ZrO_2. In oxidizing conditions we found three different hydrogen defects, each predominate in a specific range of chemical potential of electrons. Starting from the valence band top toward the conduction band bottom, these defects are the interstitial proton, $H_i^{\bullet}$, a complex formed between two hydrogen species and a zirconium vacancy with a net effective charge of (2-), $(2H)_{Zr}^{''}$, and finally a complex similar to the latter but with a net effective charge of (4-), $(H_2)_{Zr}^{''''}$. In $(2H)_{Zr}^{''}$ the two hydrogens exist in the form of hydroxyl groups, while in $(H_2)_{Zr}^{''''}$ they exist in the form of a hydrogen molecule. In addition, we found that up to three hydrogen species can favorably accumulate in a zirconium vacancy in oxidizing conditions. The clustering of hydrogen in cation vacancies can be a precursor for the deleterious effects of hydrogen on the mechanical properties and stability of metal oxides, in an analogy with hydrogen embrittlement in metals. Finally we observed a red-shift and a blue-shift for the vibrational frequencies of all the hydroxyl groups and all the hydrogen molecules, respectively, in T-ZrO_2 when compared to the gas phase frequencies. This is an important characteristic for guiding future experimental efforts to detect and identify hydrogen defects in T-ZrO_2. The insights presented in this work advance our predictive understanding of the degradation behavior of T-ZrO_2 as a resistant corrosion passive layer, as a gate dielectric and in biomedical applications.

6.1 Introduction

The pickup of hydrogen through the oxide scale until it reaches the underlying metal can proceed by several mechanisms. One possible mechanism is simply solid state diffusion through the oxide [153]. Another mechanism [154] suggests that the hydrogen generated by the corrosion reaction can accumulate in the tangential cracks in the oxide. Then by a synergistic chemical and mechanical action it can break the oxide until the metal surface is directly exposed at which point hydrogen enters the metal. A fundamental understanding of any of these mechanisms requires a critical analysis for the form in which hydrogen exists in zirconia. The goal of this chapter is to unravel the complex interaction between hydrogen and tetragonal zirconium oxide. In particular we used density functional theory to study the energy and structure of hydrogen point defects and defect complexes that can arise in T-ZrO_2. In the next chapter we examine the interplay between hydrogen defects and the planar compressive stress that T-ZrO_2 experiences at the metal/oxide interface due to the lattice mismatch between the oxide and the metal.

The urge to thoroughly understand the physics of hydrogen defects in T-ZrO_2 arises in other fields as well. We briefly describe here two other examples.

Zirconia was suggested to replace silica in metal oxide semiconductor devices due to its good thermal stability and high dielectric constant [83]. However, hydrogen is unintentionally incorporated in ZrO_2 films during the manufacturing process. Some of the incorporated hydrogen persists in the oxide in spite of post annealing. The adverse consequence is that certain forms of hydrogen defects can lead to undesirable fixed charge in the oxide [155] and can further reduce its dielectric constant [156]. Thus, mitigating these adverse effects of hydrogen requires a fundamental understanding for how it exists in zirconia films which can contain the tetragonal phase after the annealing process [83].

The second example comes from the biomedical applications of zirconia as in hip implants and dental restorations. These applications of zirconia rely on stabilizing the tetragonal phase since it exhibits high fracture toughness. However, the continuous exposure of T-ZrO_2 to moisture in a range of temperatures (30-300 ^{0}C) leads eventually to an expansive phase transformation to the monoclinic phase. The volume expansion accompanying this phase transformation leads to severe degradation and cracking of the oxide and hence limits its long term stability in usage. This phenomenon is known as the low temperature degradation of T-ZrO_2 [14, 15]. All the attempts to explain and overcome this phenomenon relate to hydrogen defects that appear in T-ZrO_2 as a consequence of water splitting on the surface of the oxide [14, 15].

Although the above examples clearly point toward the need of a thorough and a fundamental understanding of hydrogen defects in tetragonal ZrO_2, up till now this has not been realized. The earliest attempts to elucidate the types of hydrogen defects in zirconia and particularly the tetragonal phase were motivated by the nuclear industry and relied on the measurement of hydrogen permeability and solubility in zirconia [153, 157]. Collectively these experiments suggested that, in reducing conditions, oxygen vacancies are needed for the dissolution and migration of hydrogen in ZrO_2. More recently, muon spin spectroscopy experiments [115] were performed on wide band gap oxides and focused on identifying the charge state of interstitial hydrogen (indeed the analysis did not account for any possibility of hydrogen trapping in the native defects). The results suggested that in monoclinic ZrO_2 neutral interstitial hydrogen, H_i^x, predominates at low temperatures (10-100 K) while at higher temperatures (300 – 600 K) a diamagnetic form of hydrogen, $H_i^\bullet$ or H_i', predominates.

Atomistic simulations using density functional theory (DFT) were proved to be a powerful tool in studying hydrogen defects in semiconductors and insulators [133, 158-164]. In spite of this, only very few studies appeared recently to address specific types of hydrogen defects in monoclinic [133, 159], and yttria stabilized cubic zirconia [165]. For tetragonal zirconia, Shluger et al., in their review article about atomisitc simulation of defects in wide band gap oxides [83], considered performing a brief DFT comparison between the interstitial proton and the interstitial neutral hydrogen atom. They showed that the interstitial proton is stable and binds to one of the lattice oxygen to form a hydroxyl group, while the neutral interstitial hydrogen is only metastable and the electron delocalizes immediately leaving interstitial proton behind upon thermal activation.

Given the importance of deciphering the nature of hydrogen defects in T-ZrO_2, and the current status of our limited knowledge about these defects, we performed a comprehensive DFT investigation of the energetics and structure of hydrogen defects and defect complexes in T-ZrO_2. We identified the hydrogen defects that predominate separately in oxygen rich and in oxygen poor conditions. In addition, we introduced a new definition for the binding energy of a defect complex, and with it, quantified the thermodynamic stability of the complexes that forms between the hydrogen and the native defects of T-ZrO_2. Finally, we examined the electronic and atomic structure of all hydrogen-related defects and computed the vibrational frequencies of the hydroxyl group or hydrogen molecule that may exist in these defects. The latter computation is useful in guiding future experimental efforts to detect and identify hydrogen defects in T-ZrO_2.

6.2 Theoretical and computational approach

6.2.1 Defect structures and charges

We considered the defects that can arise in bulk tetragonal zirconia due to both hydrogen atom and hydrogen molecule. These defects can be classified according to the lattice site as an interstitial, a complex with an oxygen vacancy and a complex with a zirconium vacancy. The native interstitial defects were found to have very low concentration (cf. chapter 3) and hence their complexes with hydrogen were not considered here. We describe here the structures we investigated for these defects and the logic behind the charge states that we examined for each.

The initial guess for hydrogen complexes with native vacancies was obtained by replacing zirconium or oxygen with a hydrogen atom or molecule. In the case of the molecule, the center of the H_2 molecule was placed coincident with the site that was originally occupied by oxygen or zirconium. We considered 5 possible orientations of the H_2 molecule in 5 nonequivalent crystallographic directions which are <001>, <100>, <110>, <101>, and <111>. In most cases after relaxation, the molecule splits to two hydrogen species, as will be presented in the Results and Discussion section.

We performed an extensive search for the lowest energy interstitial site for the mono-hydrogen. We considered five dumbbell configurations (in some literature termed anti-bonding sites) formed by the lattice oxygen and the interstitial hydrogen in the crystallographic directions <001>, <100>, <110>, <101>, and <111>, and two dumbbell configurations formed by the lattice zirconium and the interstitial hydrogen in <001>, and <100>. We also examined two so-called bond center sites by inserting the interstitial hydrogen at the center of the bond between zirconium and oxygen. There are two distinct bond center sites because of the tetragonal distortion of the oxygen columns in tetragonal zirconia. Finally, we considered interstitial hydrogen in the octahedral site, i.e., in the middle of the conventional unit cell of T-ZrO_2 and in two crowdion sites in the directions <001> and <100>. Interstitial hydrogen molecule was examined by placing its center in the octahedral site and allowing it to take one of five orientations in the directions <001>, <100>, <110>, <101> and <111>. For illustration, we show in Figure 6-1 representative examples of the defect structures that we summarized above.

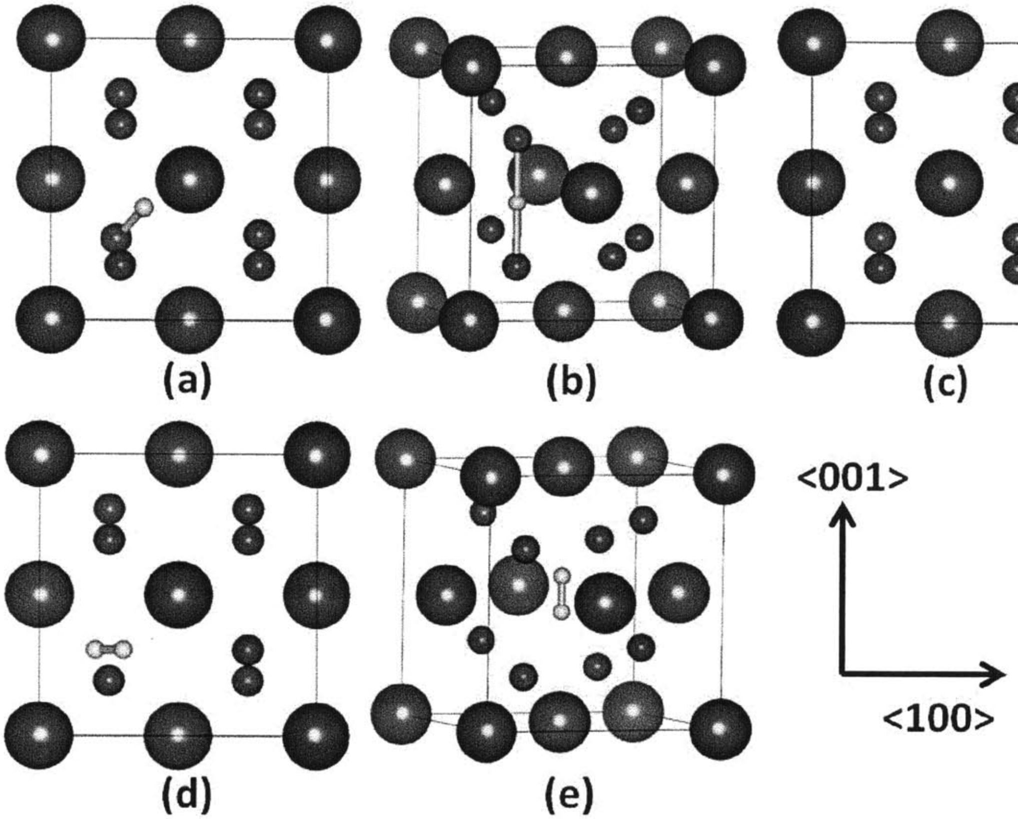

Figure 6-1: Representative hydrogen defect structures. Interstitial mono-hydrogen: (a) forming a <111> dumbbell with lattice oxygen, (b) in a <001> crowdion site between two lattice oxygens, and (c) in a bond center site. Hydrogen molecule: (d) substituting a lattice oxygen and oriented in <110>, and (e) in an interstitial octahedral site and oriented in <001>. Green (large), red (medium), and white (small) balls represent zirconium, oxygen, and hydrogen, respectively. The sticks are guide for the eye and have no physical significance.

For each one of the hydrogen defect configurations described above, we examined multiple possible charge states. The rationale behind what was considered as a possible charge state is the following. We regard the zirconium vacancy, oxygen vacancy, and both the atomic and molecular interstitial hydrogen as elementary defects. Each of these elementary defects, D, can have a charge state that ranges from $q^{D}_{\min}$ to $q^{D}_{\max}$. The values of these two extrema were taken to be (4-,0), (0,2+), (-,+) and (-,+) for zirconium vacancy, oxygen vacancy, and atomic and molecular interstitial hydrogen, respectively. For both the cation and anion vacancies, a wider range of charge states is possible, however, modeling these extra charge states need computationally expensive non-local DFT functionals and they are anticipated to have high formation energies [4, 9, 166]. When a complex is formed as the union of two elementary defects (D_1, D_2) , its charge state can in principle take any value in the range from $q^{D_1}_{\min} + q^{D_2}_{\min}$ to $q^{D_1}_{\max} + q^{D_2}_{\max}$. This simple rule sets the ground for a systematic way to investigate the possible charge states for charged defect complexes.

However, not every charge state expected for the defect complex based on the previous rule can be actually realized. As extensively discussed in Ref. [125, 167] certain charge states (including neutral) may not be possible to realize because the last added electron (hole) does not localize on the defect and favors relaxation into the conduction (valence) band. Examining the charge density and the net spin density, and performing Bader charge analysis [168, 169] were our tools to investigate and decide charge localization on the defect. Kröger-Vink notation for charged defects will be used throughout the paper.

So far we presented a systematic way to investigate the possible configurations and charge states of atomic and molecular hydrogen defects in a T-ZrO_2. However, there is evidence both from our results discussed below and from prior DFT calculations [170] on Al_2O_3 that hydrogen can cluster in the cation vacancy. This phenomenon can have a significant deleterious impact on the mechanical stability of metal oxides as hydrogen is known to be bond breaker. As a technological consequence of this, the metal oxide can fail to act as a protective passive layer for the underlying metal in a corrosive environment. Thus, it is important to quantify the energetics and understand the structure of these clusters in order to assess any potential degradation of the mechanical properties of the metal oxide. However, once the number of hydrogen species in a defect exceeds two, the possible configurations and charge states become intractable. In spite of that, our systematic investigation guided us to intuitively consider only two important clusters between hydrogen and zirconium vacancy. Those are $(3H)_{Zr}$ in the charge state (-) and $(4H)_{Zr}$ in the charge state (0). The rationale behind our choice for those two particular defects will be examined in details in section 6.4.3. Here we suffice to state that these combinations of the number of hydrogen species and the charge of the defect lead to hole-free oxygen ions around the defect which is energetically favorable.

6.2.2 Defect energetics

The abundance and stability of hydrogen defects were characterized by two energy metrics; the formation energy and the binding energy, respectively. While the former metric is applicable to any defect, the latter is devoted for complexes. The theoretical formalism to understand the energetics of defect equilibria is detailed elsewhere [3, 79]; here we summarize the relevant notions.

The formation energy of a defect D with charge q is denoted by $E^f_{D,q}$ and defined as:

$$E^f_{D,q} = E_{defected} - E_{perfect} + \sum_k \Delta n_k \mu_k + q(E_{VBM} + \mu_F) + E_{MP}, \qquad (6\text{-}1)$$

where $E_{defected}$ and $E_{perfect}$ are the DFT energies of the supercell that contains the defect and the perfect crystal supercell, respectively. Δn_k is the number of atoms of the species k in the perfect crystal supercell less the number of the atoms of the same species in the defected cell. μ_k is the chemical potential of the species k, E_{VBM} is the energy of the valence band maximum in the perfect crystal supercell, and μ_F is the chemical potential of electrons (or the Fermi level) referenced to the valence band maximum of the prefect crystal. Thus, μ_F can take a value in the range from 0 to the value of the width of the band gap in the perfect crystal. The latter was found to be 3.9 eV. Finally, E_{MP} is the Makov-Payne correction [89]. In applying this correction, we used the experimental value [91] for the static dielectric constant of yttria-stabilized tetragonal zirconia 39.8. As demonstrated in chapter 3 on the native defects of tetragonal zirconia, considering the leading term of this correction is adequate in comparison with the computationally expensive finite size scaling correction [136]. Here we demonstrate this adequacy also for selected hydrogen defects in section 6.5 at the end of this chapter. In particular we found the absolute error in the formation energies to be within 0.3 eV from the values obtained by finite size scaling for hydrogen defects.

In thermodynamic equilibrium, there are constraints on the chemical potentials of the species present inT-ZrO_2. The chemical potential of oxygen, μ_O, in T-ZrO_2 cannot exceed the chemical potential of the oxygen atom in the O_2 molecule in the gas phase. The latter is taken as ½ the DFT energy of the oxygen molecule, thus, $\mu_O \leq \frac{1}{2} E^{DFT}_{O_2}$. The chemical potential of hydrogen is constrained in the same way and hence, $\mu_H \leq \frac{1}{2} E_{H_2}^{DFT}$. Similarly, the upper bound of the chemical potential of zirconium, μ_{Zr}, in T-ZrO2 is the chemical potential of the zirconium atom in bulk zirconium metal. The latter is taken to be the DFT calculated cohesive energy of zirconium atom in hexagonal close-packed zirconium, thus, $\mu_{Zr} \leq E_{Zr-metal}^{DFT}$. The lower bounds of the chemical potentials of both zirconium and oxygen are constrained by the expression: $2\mu_O + \mu_{Zr} = E_{ZrO_2}^{DFT}$, where $E_{ZrO_2}^{DFT}$ is the DFT calculated energy of the ZrO2 unit formula in the bulk of perfect crystal T-ZrO2. Finally, the introduction of hydrogen into the system imposes an additional constraint, which is: $2\mu_H + \mu_O \leq E_{H_2O}^{DFT}$, where $E_{H_2O}^{DFT}$ is the DFT calculated energy of the water molecule in the gas phase. In our modeling for hydrogen defects in tetragonal zirconia, we considered the two extremes which are oxygen rich (zirconium poor) and oxygen poor (zirconium rich). The chemical potential of hydrogen was always set to the highest value possible (hydrogen rich) but limited by the formation of water as discussed above. The values of the chemical potentials of all the species in the two limiting cases and the DFT energies of the reference states that set the bounds discussed above are summarized in Table 6-1.

Table 6-1: The chemical potential of all the species in the two limiting extremes considered in this work. Also shown the DFT energies of the reference states that sets the bounds on the chemical potentials. All energies are in eV.

Chemical potential	oxygen rich	oxygen poor
μ_O	-4.93	-9.93
μ_H	-4.65	-3.38
μ_{Zr}	-18.56	-8.55
$E_{Zr-metal}^{DFT}, E_{O_2}^{DFT}, E_{H_2}^{DFT}, E_{H_2O}^{DFT}, E_{ZrO_2}^{DFT}$	-8.55, -9.85, -6.77, -14.23, -28.41	

The binding energy is a measure of the thermodynamic stability of a complex against dissociation into its constituents. We define the binding energy, E_b, of a complex C whose charge is q to be:

$$E_b = \max(E^f_{C,q} - \sum_k^{\prime\prime\prime} E^f_{D_k,q_k}), \qquad (6\text{-}2)$$

where k represents each constituent defects of the complex C, and the triple prime over the summation sign indicates the three constraints imposed on the summation. The first is the conservation of species, that is the defects D_1, D_2,... when combined together have to be chemically equivalent to the complex C. The second constraint is the conservation of charge, that is $q = \sum_k q_k$. *Thus, the binding energy is neither dependent on the chemical potential of species forming the complex, nor the chemical potential of electrons.* The third constraint is physically motivated, and discards the dissociation pathways for the complex that can lead to the formation of a disallowed charge state for certain constituent defect, D_k. The last constraint is concerned with the defects that exhibit negative-U behavior. The latter are the singly charged oxygen vacancy as shown in our previous study on the native defects (cf. chapter 3), and the neutral interstitial hydrogen atom as discussed below. The max function in the definition indicates that the stability of the complex is determined by its easiest dissociation pathway. This is an important point to emphasize as we believe that most of the binding energy values for hydrogen complexes in ionic materials reported in the literature are somewhat exaggerated because of limiting the search to one dissociation pathway. To the best of our knowledge, only the work of Kang et al. on hydrogen defects in HfO_2 considered this important aspect [155]. The convention we adopt for the binding energy in equation (6-2) is such that negative values indicate stable complexes and positive values indicate unstable complexes.

Strictly speaking the binding energy alone is not enough to characterize the stability of defect complexes. A better metric would be, $-E_b + E_a$, where E_a is the activation energy needed for the dissociation of the constituents of the defect complex [160]. In other words, a defect may possess a positive binding energy (thermodynamically unstable) but could be kinetically trapped and be present because of the high activation energy for dissociation at a given temperature. The formation of kinetically stabilized defect complexes can occur in a non-equilibrium process such as crystal growth or corrosion. In this work we focus on the thermodynamically stable defect complexes as these are anticipated to be the predominant in terms of concentration.

We emphasize here based on sections 6.2.1 and 6.2.2 that we will limit the discussion in what follows to the defects in the configurations that has the lowest formation energy <u>and</u> in the charge states that are both physically realizable <u>and</u> thermodynamically stable against dissociation. In this context, "a thermodynamically stable defect" means it has a negative binding energy, while "a stable defect" indicates that its charge is possible to realize in the simulation cell without delocalization of electrons or holes. In the following, the defects that satisfy both of these definitions are presented.

6.2.3 Density functional theory calculations

The projector-augmented plane-wave method [100] as implemented in the Vienna Ab-initio Simulation Package (VASP) [101-104] was utilized to perform the density functional theory calculations. The parameterization of Perdew, Burke, and Ernzerhof (PBE) [105, 106] was used to represent the exchange-correlation. Consistent with our previous work on the native defects of tetragonal zirconia (cf. chapter 3), we used a kinetic energy cutoff of 450 eV, a supercell composed of $2\times2\times2$ conventional unit cells, and $2\times2\times2$ Monkhorst-Pack *k*-point mesh.

In order to understand the effect of the local structure in a crystalline solid on the vibrations of hydrogen and also to provide a computationally derived database that can be validated by Infra Red and Raman spectroscopy measurements, we calculated the vibrational frequencies for certain hydrogen defects. In particular, whenever a hydroxyl group or a hydrogen molecule is part of a thermodynamically stable defect, we calculated their stretch mode frequency in the harmonic approximation. We targeted these particular species because their stretch mode frequency is known to be much higher than the host vibrational modes and hence justifying fixing the host ions while calculating the vibrational frequencies of hydrogen. The details of the calculations are similar to what is presented in chapter 3 except that we found a finite difference distance of 0.008 Å is needed to obtain converged frequencies for hydrogen defects in contrast to 0.004 Å used in our study of the native defects. Since anharmonic effects and the limitations inherent in DFT functionals (including hybrids) can significantly affect the absolute values of the vibrational frequencies [161], it was suggested that , $\Delta\omega$, the difference between the harmonic frequency in the crystalline solid and the harmonic frequency in the gas phase, is a better metric to utilize when comparing with experiments. Thus, the stretch mode of the hydrogen molecule and the hydroxyl group in the solid was referenced to the same mode of these species in the gas phase. Our calculated reference values are 4317 cm^{-1} for H_2 and 3684 cm^{-1} for OH^- both in the gas phase. The experimental values (anharmonic) for these modes are 4161 cm^{-1} and 3556 cm^{-1}, respectively [171, 172].

6.3 The energetics of hydrogen defects in tetragonal zirconia

In this section we discuss the formation energies of the three categories of hydrogen defects, namely, the interstitial, the complex with an oxygen vacancy, and the complex with a zirconium vacancy in the two limiting cases of oxygen rich (oxidizing) and oxygen poor (reducing) conditions. This is followed by a discussion of the thermodynamic stability of the complexes utilizing the binding energy as a metric.

6.3.1 Formation energies and thermodynamic transition levels

Figure 6-2 is a plot of the formation energies of hydrogen defects as a function of the chemical potential of electrons in (a) oxygen poor conditions, and (b) oxygen rich conditions. For each defect we show only the predominant charge states. For comparison, we show also the formation energies of oxygen and zirconium vacancies. The shading in the figure indicates the range of the chemical potential of electrons accessible by self-doping due to the native defects of T-ZrO_2 as determined in chapter 3. The presence of hydrogen in T-ZrO_2, regarded as an extrinsic dopant, can affect this range. Quantifying the effect of hydrogen on this range requires thermodynamic analysis similar to what is presented in chapter 3 which is not the scope of this work. Thus, the shaded range shown in Figure 6-2 has to be regarded as a very probable initial guess for the accessible range in hydrogenated T-ZrO_2. On the other hand, the remaining range of μ_F can also be made accessible by doping with aliovalent cations or anions, making it important to consider the region outside the shading as well. Before discussing the details of Figure 6-2, it is important to stress that the thermodynamic transition levels from charge q_1 to charge q_2 for each defect are independent of the chemical potentials of species. Hence, in the discussion we will quote the values of these levels. On the other hand, the range of μ_F over which certain defects predominate over the others depends on the chemical potential of species. Figure 6-2 depicts only the two extremes of μ_O (poor and rich) and the rich extreme of μ_H.

Hence, it is not that meaningful to quote in the discussion exact ranges of μ_F over which predomination of certain defect takes place. We will thus, limit the discussion of predomination to qualitative trends. It is straightforward, however, to derive from Figure 6-2 quantitative ranges of predomination at specific values of the chemical potential of species when desired.

Our calculations indicate that interstitial hydrogen, H_i, exhibits a negative-U behavior with a U value of -1.96 eV. Moreover, the interstitial hydrogen defect was found to be amphoteric, i.e., it can exist both as a hydride ion and as a proton in distinct ranges of μ_F. The thermodynamic transition level (+/-) for interstitial hydrogen from proton to hydride ion happens to be at 2.84 eV which is within the range of μ_F accessible by self-doping due to the native defects. Recently, it was also shown that interstitial hydrogen is both amphoteric and a negative-U defect in monoclinic zirconia [133]. A further confirmation for the negative U-behavior is evident from the atomic and electronic structure of interstitial hydrogen defects in the next subsection. The interstitial hydrogen molecule, $(H_2)_i$, is predominantly neutral and has higher formation energy compared to the interstitial mono-hydrogen.

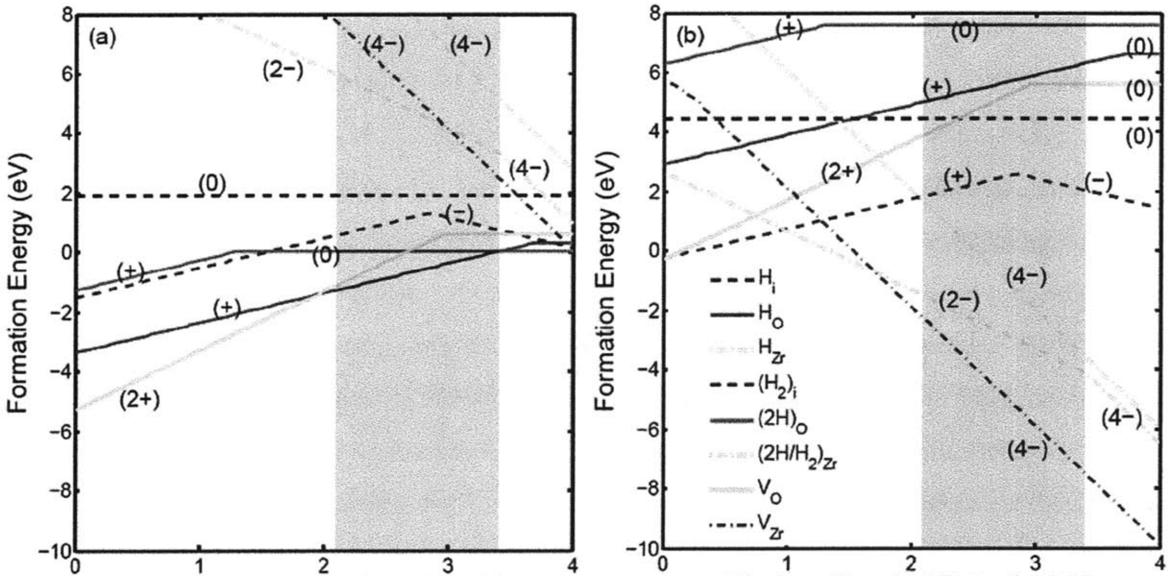

Figure 6-2: The formation energy of hydrogen defects in (a) oxygen poor conditions, (b) oxygen rich conditions. Solid, dashed, dot-dashed lines indicate oxygen-related, interstitial, zirconium-related defects, respectively. The shading indicates the range of the chemical potential of electrons accessible by self-doping due to the native defects as determined in chapter 3.

The charge state (+) is predominant for the defect complex made of a mono-hydrogen and an oxygen vacancy, H_O, in almost all the band gap except for a narrow range close to the conduction band where the neutral charge state predominates. This behavior for this defect was found recently in monoclinic ZrO_2 and HfO_2 [133]. However, in another n-type oxide (ZnO) only the charge state (+) was found to be dominant [158], while in a p-type oxide (Cu_2O) each of the charge states (-,0,+) was found to predominate a certain region of the band gap [173]. We also found that upon inserting another hydrogen species in the oxygen vacancy site to form $(2H)_O$, the formation energy of the complex increases compared to that of H_O (except for a narrow range of μ_F in the oxygen poor conditions). The tendency of the oxygen vacancy to reject hydrogen clustering was also observed in ZnO and MgO [158]. Contrary to the mono-hydrogen case, the neutral charge state of the complex of two hydrogen and an oxygen vacancy, $(2H)_O$ is predominant in most of the band gap except for a range of 1.3 eV near the valence band where the (+) charge state predominates.

The predominant charge state for the complex made of a mono-hydrogen and a zirconium vacancy, H_{Zr}, is (4-) and indeed it is the only thermodynamically stable charge state. Interestingly adding another hydrogen species into the zirconium vacancy to form $(2H/H_2)_{Zr}$ lowers the formation energy of the complex compared to that of H_{Zr} and in this case multiple charge states are thermodynamically stable. The charge state (2-) predominates starting from the valence band edge up to the thermodynamic transition level (2-/4-) at 3.4 eV. A similar tendency for hydrogen accumulation in cation vacancies was also observed in Al_2O_3 [170]. This accumulation can take place in a non-equilibrium process such as crystal growth or corrosion. The abundance of the clusters formed in this process depends on the formation energy of these clusters. Once equilibrium is reached in the region in which hydrogen clusters were formed, the binding energy would be the metric to decide their thermodynamic stability. Quantifying the abundance, thermodynamic stability and electronic structure of these complexes is of paramount importance to assess the resistance of the oxide layers natively grown on metal surfaces to the deleterious effects of hydrogen. Hydrogen is known to interact strongly with the host lattice and can lead to bond breaking subsequently followed by degradation of the mechanical properties of the host. While this effect is well-studied in metals and is commonly termed as hydrogen embrittlement, it is by far less studied in oxides. The fact that two hydrogen species in a zirconium vacancy have lower formation compared to the case of mono-hydrogen led us to investigate two special cases where three or four hydrogen species accumulate in a zirconium vacancy. These two cases are discussed later.

Figure 6-2 contrasts the predominant hydrogen defects in oxygen poor and oxygen rich conditions. In the former case (Figure 6-2(a)), mono-hydrogen associated with an oxygen vacancy, H_O, in the charge state (+) predominates for most of the band gap except for a narrow range close to the conduction band in which di-hydrogen oxygen vacancy complex, $(2H)_O$, in the neutral charge state predominates. In the oxygen rich conditions (Figure 6-2(b)) and starting from the valence band edge, the interstitial proton predominates over a range of μ_F. For the rest of the band gap and up to the conduction band edge, the di-hydrogen associated with a zirconium vacancy, $(2H/H_2)_{Zr}$, predominates first in the charge state (2-) and then in the charge state (4-). Our results in the oxygen poor conditions are consistent with the experimental findings of Park and Olander [157]. They observed that in oxygen poor (reducing) conditions, the solubility of hydrogen increases with the increase of the off-stoichiometry, x, in T-ZrO_{2-x} in accordance with our finding that hydrogen associates with oxygen vacancies in these conditions.

We examined the clustering of 3H and 4H in a zirconium vacancy in the charge states (-) and (0), respectively. The choice of these particular charge states is justified in the atomic and electronic structure section 6.4.3. In Figure 6-3 we present all the zirconium related defects in oxygen poor (a) and oxygen rich conditions (b). It is clear from the figure that the clusters $(3H)_{Zr}^{'}$ and $(4H)_{Zr}^{x}$ predominate the hydrogen-zirconium vacancy complexes in certain ranges of μ_F mainly in the p-type region. In the oxygen rich conditions these clusters have low formation energies. This demonstrates that zirconium vacancies can act as trapping sites for hydrogen and the resulting complexes can be precursors for the adverse effects of hydrogen on the mechanical stability of the oxide. Furthermore, as we show below, most of the hydrogen-zirconium vacancy complexes have high binding energy.

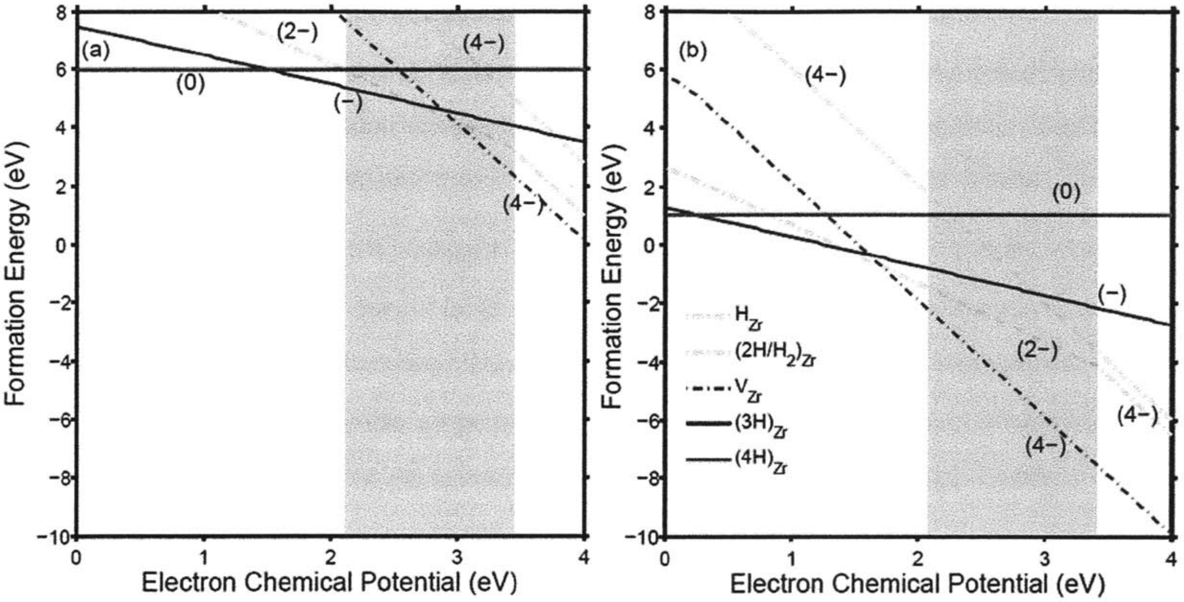

Figure 6-3: The formation energy of hydrogen defect complexes with a zirconium vacancy including the two special clusters that contain 3H and 4H in (a) oxygen poor conditions and (b) oxygen rich conditions. The formation energy of the zirconium vacancy is included for comparison. The shading indicates the range of the chemical potential of electrons accessible by self-doping due to the native defects as determined in chapter 3.

6.3.2 Binding energies

The calculated binding energies for the thermodynamically stable complexes are reported in Table 6-2 Although in our classification of the defects presented above we regarded the interstitial hydrogen molecule as an elementary defect, it is also possible to consider it as a complex formed due to association between a proton and a hydride ion. Assuming the latter picture, we found it to be stable against dissociation with a binding energy of -0.74 eV. The predominant mono-hydrogen oxygen vacancy complex charge state identified above is (+) and this indeed is a highly stable complex with a binding energy -2.22 eV. For this complex, the calculation of the binding energy for the charge states (2+) and (0) according to our definition is problematic. The only possible dissociation pathways for those two charge states involve the formation of a disallowed charge state for a negative-U defect (that is the singly charged oxygen vacancy and neutral interstitial hydrogen). We reported in the table values calculated upon relaxing the constraint of discarding the negative-U disallowed charge states. Thus, $H_O^{\bullet\bullet}$ was deemed to be unstable, while H_O^{x} was found to be stable with a binding energy of -1.5 eV. On the other hand, the calculated binding energies for the di-hydrogen oxygen vacancy complexes indicate relatively shallow binding. We found the easiest dissociation pathway for these complexes to involve the formation of $H_O^{\bullet}$.

Only the charge state (4-) is stable thermodynamically for mono-hydrogen zirconium vacancy complex, H_{Zr}, with a binding energy of -1.28. For the di-hydrogen zirconium vacancy complex, the predominant charge states $(2H)_{Zr}^{''}$ and $(H_2)_{Zr}^{''''}$ have binding energies of -2.79 eV and -1.06 eV, respectively. The latter charge state is distinct from the rest by the fact that is the only one in which the hydrogen molecule exists as an entity in the vacant site. In the other charge states, the two hydrogen species exist as hydroxyl groups. More details on the structure are presented in the next subsection. The cluster of 3H and zirconium vacancy, $(3H)_{Zr}^{'}$, was found to be stable with a binging energy of -1.17 eV, while the cluster formed between 4H and a zirconium vacancy, $(4H)_{Zr}^{x}$, has a very shallow binding energy of -0.02 eV. The limiting dissociation pathway of the $(4H)_{Zr}^{x}$ cluster is the one that leads to the formation of the $(3H)_{Zr}^{'}$ cluster and an interstitial proton.

To reiterate, clustering of hydrogen in zirconium vacancies can lead to the formation of thermodynamically stable defects; a result of significant importance when considering the deleterious effects of hydrogen on the mechanical properties of oxides.

Table 6-2: The binding energy of the thermodynamically stable hydrogen defect complexes.

Complex	Binding Energy (eV)
$(H_2)_i^{x}$	-0.74
$H_O^{\bullet\bullet}$, $H_O^{\bullet}$, H_O^{x}, $H_O^{'}$	+0.59[a], -2.22, -1.5[a], -0.74
$(2H)_O^{\bullet}$, $(2H)_O^{x}$, $(2H)_O^{'}$	-0.09, -0.76, -0.78
$H_{Zr}^{''''}$	-1.28
$(2H)_{Zr}^{x}$, $(2H)_{Zr}^{'}$, $(2H)_{Zr}^{''}$, $(H_2)_{Zr}^{''''}$	-2.65, -2.79, -2.94, -1.06
$(3H)_{Zr}^{'}$, $(4H)_{Zr}^{x}$	-1.17, -0.02

[a] The only possible dissociation pathways for these complexes involve the formation of a disallowed charge state for a negative-*U* defect. Here we report the values computed based on equation (6-2) but by relaxing the constraint related to the negative-*U* defects.

6.4 The atomic and electronic structure of hydrogen defects in tetragonal zirconia

Understanding the defect atomic and electronic structure is of utmost importance. On one hand it can help in rationalizing many of the energy-based results. On the other hand it provides a basis for fundamental measurable quantities that can be probed experimentally such as the net spin of a defect that can be probed in muon spectroscopy [115] and characteristic vibrational frequencies that can be detected in Raman and Infra Red spectroscopy [174]. Finally, the underlying structure of a defect determines its response under mechanical loading. This response, in turn, is needed to understand and quantify the adverse effects of hydrogen on the mechanical properties of oxides.

In this section, we discuss the atomic and electronic structure of each of the three categories of hydrogen defects. In particular, for each category we examine the geometry of the minimum energy configuration of each defect. In addition, we utilize the net spin density and Bader charge analysis as metrics to understand the electron distribution within the defect. This analysis is complemented by examining the stretch mode frequency of any hydroxyl group or hydrogen molecule that resides as an entity within the defect. As discussed in section 6.2.3, we report the difference, $\Delta\omega$, between the harmonic stretch of the species in the condensed phase and the harmonic stretch of the reference (OH^- or H_2) in the gas phase. For comparison purpose, we report here that our calculated O-H and H-H bond lengths in the gas phase OH^- and H_2 are 0.977 Å and 0.751 Å, respectively. For each of the upcoming figures, the color code and the orientation of the simulation cell is the same as in Figure 6-1.

6.4.1 Interstitial defects

Figure 6-4 depicts the minimum energy configuration for the possible charge states of interstitial mono-hydrogen (a,b,c) and interstitial hydrogen molecule (d,e). An isosurface of the net electronic spin density is also shown whenever the defect exhibits a net magnetic moment. Closely related to Figure 6-4 is Table 6-3 in which we present the calculated Bader charges, the bond length of any OH^- or H_2 species and the quantity $\Delta\omega$ defined above.

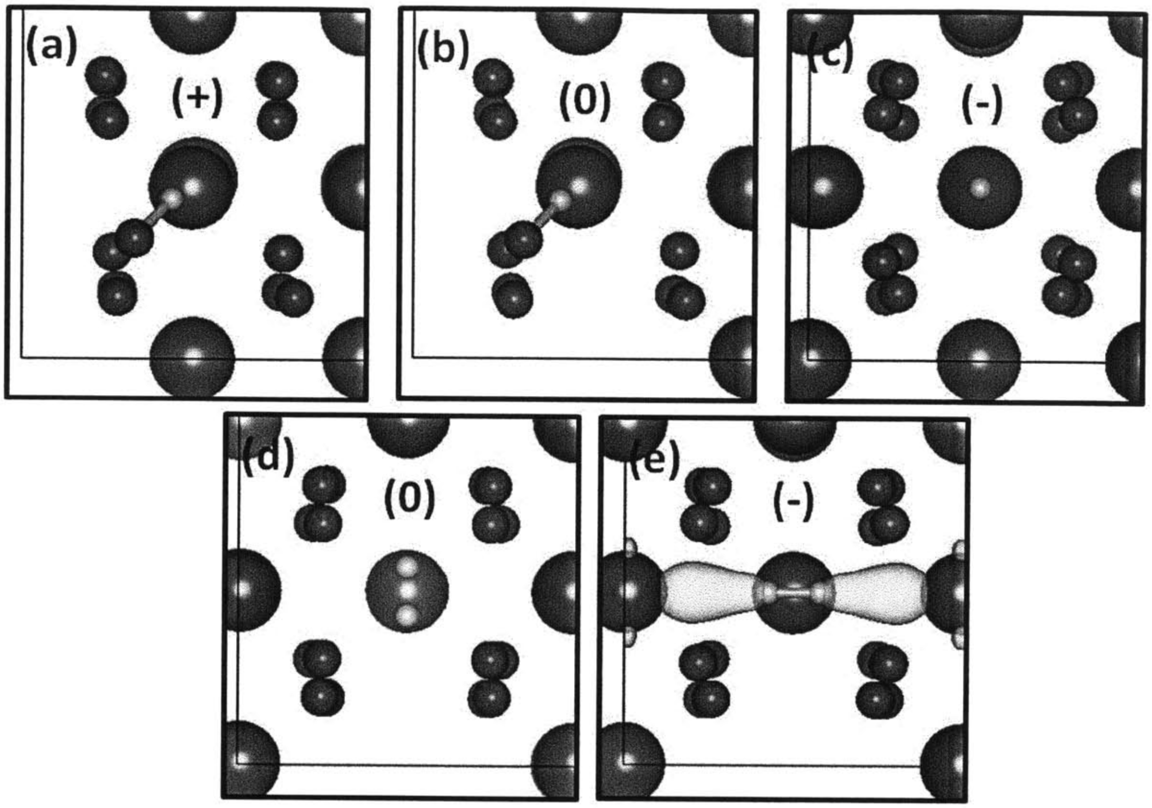

Figure 6-4: The minimum energy structures for the thermodynamically stable interstitial hydrogen defects together with an isosurface for the net spin density (if nonzero). (a) $H_i^{\bullet}$, (b) H_i^{x}, (c) $H_i^{'}$, (d) $(H_2)_i^{x}$, and (e) $(H_2)_i^{'}$. The yellow isosurface is taken at 0.01 Å^{-3}.

Table 6-3: Calculated properties for the interstitial hydrogen defects. Bader charges are shown for hydrogen only. The distance, *d*, is the bond length of H_2 or OH^- if either of them was detected in the simulation cell. The frequency difference, $\Delta\omega$, is defined in section 6.2.3.

Defect	Bader Charge (*e*)	*d* (Å)	$\Delta\omega$ (cm^{-1})
$H_i^{\bullet}$	+0.62	O-H: 0.986	-279 [a]
H_i^{x}	+0.61	O-H: 0.987	-310 [a]
$H_i^{'}$	-0.49	-	-
$(H_2)_i^{x}$	-0.11, +0.04	H-H: 0.739	+84 [b]
$(H_2)_i^{'}$	-0.14, -0.01	H-H: 0.786	-825 [b]

a The reference is the stretch mode of OH^-
b The reference is the stretch mode of H_2

The underlying structure for both the charge states (+) and (0) of interstitial mono-hydrogen is a hydroxyl group formed between hydrogen and one of the lattice oxygen and oriented in <111>. The same structure was also identified through DFT calculations on T-ZrO_2 in Ref. [83]. Furthermore, we found that the net spin localized on the defect in the case of neutral charge state is zero, indicating that the *1s* electron of the hydrogen atom is in a shallow electronic state right at the edge of the conduction band. This was also found to be the case in monoclinic zirconia through electronic density of states calculations [175]. Thus, in the neutral DFT simulation cell the hydrogen is indeed a proton and most of the *1s* electron wave function is delocalized. This is supported by the very similar Bader charge, O-H bond length, and $\Delta\omega$ for (+) and (0) cases. This also is in accordance with the negative-U behavior identified through the energetics. A general feature that we observe for all the OH^- groups that arise in the hydrogen defects in T-ZrO_2 is the reduction of the stretch frequency (e.g. -279 cm^{-1} for interstitial proton) compared to the gas phase OH^-. This is an important signature that is amenable to investigation in Raman and Infra Red spectroscopy experiments. A more striking feature was identified for H_2 vibrations and is discussed below.

The favorable site for the hydride ion was found to be the octahedral site as shown in Figure 6-4(c). This is expected given the electrostatic repulsion between the eight oxygen ions in the unit cell and the hydride ion. The zero net spin on the defect and the negative Bader charge both indicate the pairing between two *1s* electrons on the interstitial hydrogen and confirm its character as a hydride ion.

The neutral interstitial hydrogen molecule was found to be oriented in <001> direction as depicted in Figure 6-4(d). The bond length of the interstitial molecule is shortened by 0.012 Å and the stretch mode frequency is enhanced by +84 cm^{-1} compared to the gas phase. Our calculations indicate that this is a general feature for all the neutral hydrogen molecules that arise in a defect in T-ZrO_2. This is strikingly the opposite of what was found for the interstitial hydrogen molecule in semiconductors both experimentally and theoretically[161]. The shortening of the bond length of the molecule and the upshift of its vibrational frequency are the signature of enhanced *intra*molecular interaction. Such enhancement of the *intra*molecular interactions for a molecule due to the *inter*molecular interactions in the condensed phase is counterintuitive [176]. We believe that this important finding requires future experimental confirmation. We also found that the di-hydrogen anion is stable in the crystalline environment of T-ZrO_2 in <100> direction. The extra electron added to $(H_2)_i^x$ to form $(H_2)_i^{'}$ is mainly shared among the surrounding zirconium cations as indicated by the net spin density in Figure 6-4(e) and the Bader charge analysis. On the other hand, the di-hydrogen cation was found to be unstable in the crystalline environment of T-ZrO_2. Our findings related to the di-hydrogen anion and cation are consistent with what is generally known about these molecular ions, i.e., the former is stable in a condensed phase but not in the gas phase while the converse applies for the latter [177].

6.4.2 Hydrogen-oxygen vacancy complexes

The key to understand the structure of hydrogen-oxygen vacancy complexes is to recall the electronic structure of the oxygen vacancy identified previously in chapter 3. The latter was found to have a negative-U character. In addition, it was found that the neutral oxygen vacancy has the electronic structure of an F-center where two d-electrons from the neighboring zirconium ions localize on the vacant site. Removing one of these electrons to create a singly charged vacancy leads to the localization of the remaining electron right on the vacant site. Removing the last electron leads to the formation of the doubly charged oxygen vacancy. In Figure 6-5 we show the minimum energy configuration for the possible charge states of the complexes formed between the oxygen vacancy and the mono hydrogen (a,b,c), and between the oxygen vacancy and the di-hydrogen (d,e,f). Whenever a defect exhibits a net magnetic moment, an isosurface of the net spin density is also shown. In Table 6-4 we present the calculated Bader charges for the hydrogen species associated with the oxygen vacancy and the distance between the two hydrogen species if they coexist in the vacant site. This distance is not a bond length, because we did not detect any chemically bonded species when hydrogen associates with an oxygen vacancy. Thus, we did not calculate the vibrational frequencies of hydrogen in oxygen vacancies as the lack of chemical bonding leads to severe reduction in its frequencies. This reduction makes hydrogen vibrations not very distinguishable from the host vibrations.

The thermodynamically stable most positive charge state for mono-hydrogen oxygen vacancy complex is (+). The association results in a hydride ion located almost at the center of a doubly charged oxygen vacancy as shown in Figure 6-5 (a). Bader charge analysis also supports that the hydrogen species in this case is a hydride ion. This charge state was found to be energetically predominant for most of the band gap of T-ZrO_2. Adding one more electron to obtain the charge state (0) leads to the localization of this electron in the *d* orbitals of two neighboring zirconium ions at the edge of the conduction band minimum as shown in Figure 6-5 (b). This structure is akin to the so-called multicenter bond configuration for hydrogen in the oxygen vacancy in metal oxides [158]. The charge state (-) is obtained by adding one more electron, the resultant is a hydride ion associated with an F-center. The strong repulsion between the two electrons of the F-center and the hydride ion renders this charge state very unfavorable energetically.

We did not find any evidence that the hydrogen molecule can exist in an oxygen vacancy in T-ZrO_2. Thus, any two hydrogen species in an oxygen vacancy are not bonded together; instead they exist as an oriented dumbbell. We found that this dumbbell is favorably oriented in <110> for all the charge states. The thermodynamically stable most positive charge state for two hydrogen species in an oxygen vacancy is (+). The structure of this complex, shown in Figure 6-5 (d), consists of two hydrogen atoms separated by a distance of 0.984Å associated with a singly charged oxygen vacancy. The charge density of the electron of the singly charged vacancy is spread over the two hydrogen atoms and the surrounding oxygen and zirconium ions. The distance between the two hydrogen atoms is significantly larger than the bond length of hydrogen molecule or even the di-hydrogen anion. The charge state (0) of the complex, shown in Figure 6-5(e), consists of two hydride ions associated with a doubly charged oxygen vacancy. The partial charges on the two hydrogen species confirm their identification as hydride ions. Finally, obtaining the charge state (-) by adding one further electron leads to its localization on the *d* orbitals of two neighboring zirconium cations as shown in Figure 6-5 (f). The strong repulsion between the two hydride ions and the extra localized electron elongated the H-H distance to 2.071Å and renders the charge state energetically unfavorable, but still thermodynamically stable.

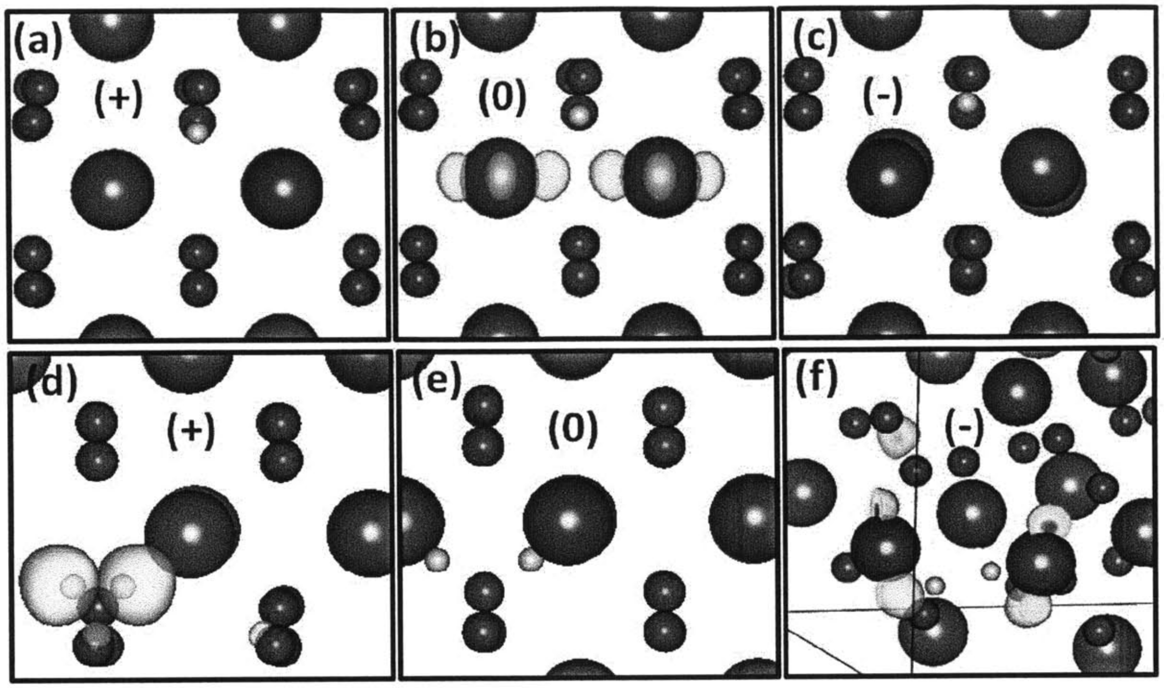

Figure 6-5: The minimum energy structures for the thermodynamically stable hydrogen-oxygen vacancy complexes together with an isosurface for the net spin density (if nonzero). (a) $H_O^\bullet$, (b) H_O^x, (c) H_O', (d) $(2H)_O^\bullet$, (e) $(2H)_O^x$, and (f) $(2H)_O'$. The yellow isosurface is taken at 0.01 Å^{-3}.

Table 6-4: Calculated properties for the hydrogen oxygen vacancy complexes. Bader charges are shown for hydrogen only. The distance, *d*, is between two hydrogen species and does *not* correspond to a bond length.

Defect	Bader Charge (*e*)	*d* (Å)
$H_O^\bullet$	-0.59	-
H_O^x	-0.66	-
H_O'	-0.76	-
$(2H)_O^\bullet$	-0.24, -0.19	0.984
$(2H)_O^x$	-0.50, -0.52	1.928
$(2H)_O'$	-0.55, -0.56	2.071

6.4.3 Hydrogen-zirconium vacancy complexes

Before discussing hydrogenated zirconium vacancies, we recall the electronic structure of pristine ones that we identified previously in chapter 3. The neutral zirconium vacancy has the V-center structure where the vacant site is surrounded by four holes localized on four neighboring oxygen ions. By filling the four holes with electrons one by one, we obtain all the possible charge states until filling all of them and obtaining $V_{Zr}^{''''}$. The latter was reckoned to be the predominant energetically. Figure 6-6 shows the minimum energy configuration for all the possible and thermodynamically stable charge states for the hydrogenated zirconium vacancies. An isosurface of the net spin density is shown whenever a defect exhibits a net magnetic moment. Table 6-5 shows the calculated Bader charge for hydrogen in zirconium vacancies, and the bond length and $\Delta\omega$ for any OH^- or H_2 species in the defect.

For the defect complex made of a mono-hydrogen and a zirconium vacancy, only the (4-) charge state is thermodynamically stable. The atomic and electronic structure of this defect depicted in Figure 6-6(a) reveals that hydrogen in atomic form is located in the center of $V_{Zr}^{''''}$. The spherically symmetric net spin density of the *1s* electron localized on hydrogen is clearly observed. The key to comprehend hydrogen molecule-zirconium vacancy interactions is the following rule that we deduced from our DFT simulations. The priority is to fill the holes localized on the oxygen ions surrounding the zirconium vacancy. This is accomplished by dissociating the H_2 molecule and donating its two electrons to fill the holes. The resulting two protons bind to two of the surrounding oxygens to form hydroxyl groups. Upon filling all the holes, the H_2 molecule can be stabilized in the vacant site. With this rule in mind we observe in Figure 6-6(b) that the association between H_2 and V_{Zr}^{x} lead to the dissociation of the molecule, filling two holes on two oxygen ions, forming two OH^- groups between the resulting two protons and the two hole-free oxygen ions, and finally leaving two holes localized on other two oxygen ions. Adding one electron to obtain the charge state (-) leads to filling one more hole as in Figure 6-6(c). Adding one further electron fills the last hole and leads to the charge state (2-) shown in Figure 6-6(d). This charge state is the one that predominates energetically for a wide range in the band gap of T-ZrO_2. At this stage trying to add one more electron to obtain the charge state (3-) does not lead to the localization of the electron on the defect. The reason is that no more holes are available for recombination and also the di-hydrogen cation cannot be stabilized in the condensed environment of T-ZrO_2 as mentioned above. Thus, the charge state (3-) cannot be realized. However, the charge state (4-) is possible where the last added two electrons lead to the formation of the H_2 molecule in the vacant site with <111> orientation being the most favorable as shown in Figure 6-6(e). The Bader charge analysis supports the arguments presented above, where all the identified protons have a partial charge of about +0.6 and all the neutral species (H_2 and H) have an almost zero partial charge as shown in Table 6-5. Also in accordance with what we identified earlier, the stretch frequency of any OH^- associated with zirconium vacancy is red-shifted while that of the H_2 molecule associated with zirconium vacancy is blue-shifted.

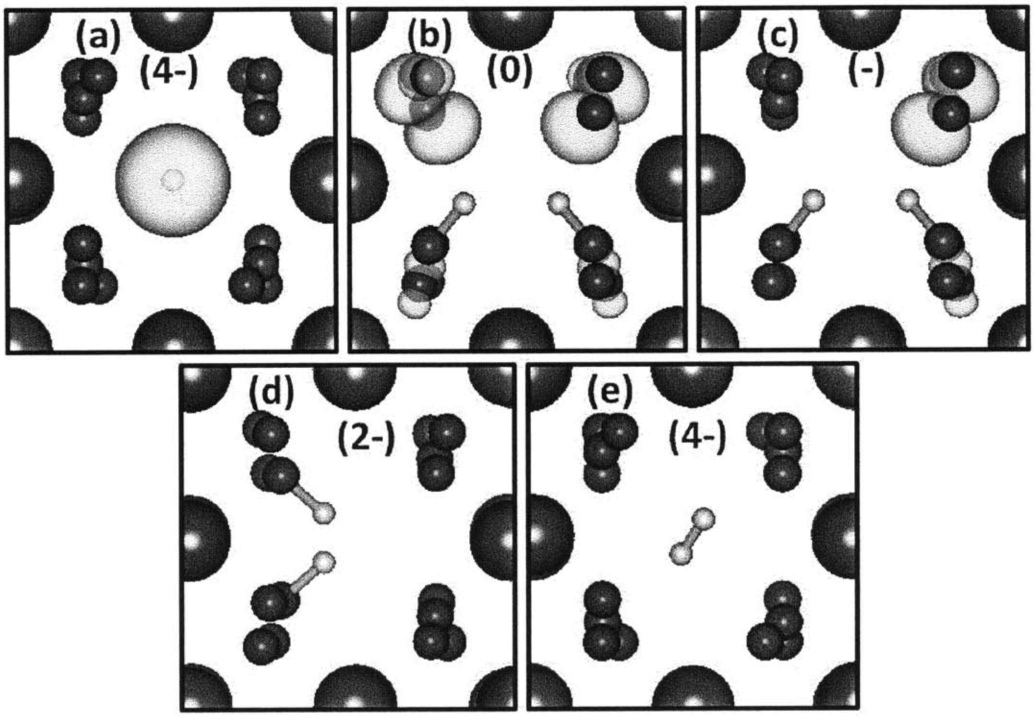

Figure 6-6: The minimum energy structures for the thermodynamically stable hydrogen-zirconium vacancy complexes together with an isosurface for the net spin density (if nonzero). (a) $H_{Zr}^{'''}$, (b) $(2H)_{Zr}^{x}$, (c) $(2H)_{Zr}^{'}$, (d) $(2H)_{Zr}^{''}$, and (e) $(H_2)_{Zr}^{''''}$. The yellow isosurface is taken at 0.01 Å^{-3}.

Table 6-5: Calculated properties for hydrogen-zirconium vacancy complexes. Bader charges are shown for hydrogen only. The distance, *d*, is the bond length of H_2 or OH^- if either of them was detected in the simulation cell. The frequency difference, $\Delta\omega$, is defined in section 6.2.3.

Defect	Bader Charge (e)	d (Å)	$\Delta\omega$ (cm^{-1})
$H_{Zr}^{''''}$	+0.04	-	-
$(2H)_{Zr}^{x}$	+0.63, +0.63	O-H: 0.974, 0.974	-120, -130 [a]
$(2H)_{Zr}^{\bullet}$	+0.62, +0.62	O-H: 0.975, 0.975	-91, -103 [a]
$(2H)_{Zr}^{\bullet\bullet}$	+0.62, +0.62	O-H: 0.977, 0.977	-56, -71 [a]
$(H_2)_{Zr}^{''''}$	-0.04, +0.03	H-H: 0.738	+145 [b]

a The reference is the stretch mode of OH^-
b The reference is the stretch mode of H_2

The rule identified above for the di-hydrogen interaction with a zirconium vacancy is what guided our choice to examine the charge states (-) and (0) for the 3H and 4H, respectively. Consider the neutral zirconium vacancy with 4 holes surrounding the vacant site as the starting point. Inserting 3H leads to filling three holes and forming three OH^- groups between the resultant protons and hole-free oxide ions. Given that hole localization on the oxide ion is not favored by the Madelung potential of the oxide [116], we decided to the fill the last hole by an electron and hence considering the charge state (-). In the case of 4H, the electrons provided by the hydrogen species are enough to fill all the holes and eventually forming four OH^- groups. However, it seems that the repulsion between the four protons is strong such that the binding energy of this complex is only -0.02 eV. Figure 6-7 shows the relaxed structure for these two special clusters. In Table 6-6 we report the calculated Bader charge for the hydrogen species together with the bond lengths and the vibrational frequencies for the hydroxyl groups. Bader charge analysis confirms that all the hydrogen species in these two clusters are protons. In addition to this, the vibrational frequencies of all the OH^- groups are downshifted conforming to the trend we identified for all OH^- in T-ZrO_2.

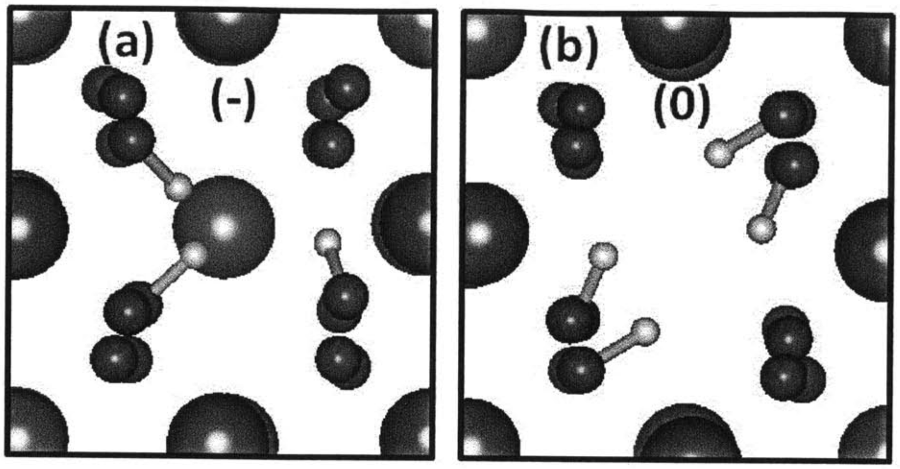

Figure 6-7: The relaxed structures of the clusters (a) $(3H)_{Zr}^{'}$, and (b) $(4H)_{Zr}^{x}$.

Table 6-6: Calculated properties for the two special clusters formed between hydrogen and the zirconium vacancy. Bader charges are shown for hydrogen only. The distance, *d*, is the bond length of the OH^- detected in the defect. The frequency difference, $\Delta\omega$, is defined in section 6.2.3.

Defect	Bader Charge (*e*)	d (Å)	$\Delta\omega$ (cm^{-1})
$(3H)_{Zr}^{'}$	+0.61, +0.63, +0.62	O-H: 0.973, 0.982, 0.991	-51, -239, -450 [a]
$(4H)_{Zr}^{x}$	+0.64, +0.64, +0.62, +0.62	O-H: 0.979, 0.979, 0.996, 0.996	-181, -188, -489, -494 [a]

a The reference is the stretch mode of OH^-

6.5 On the adequacy of Makov-Payne correction for hydrogen defects in tetragonal ZrO₂

We assessed the adequacy of the leading term of the Makov-Payne (MP) correction by comparing its results with the results obtained by finite size scaling. This assessment was done on four selected defects which are $H_i^{\bullet}$, $H_i^{/}$, $H_O^{\bullet}$, and $(H_2)_{Zr}^{////}$. The first two are generally regarded very important defects in metal oxides, the third is the predominant in oxygen poor conditions in T-ZrO_2, and the last predominates in oxygen rich conditions in T-ZrO_2 and is representative for the highest possible charge state for a hydrogen defect in this work. The details of the simulation cells used to perform finite size scaling are summarized in Table 6-7.

Table 6-7: The details of the supercells used to perform the finite size scaling on selected hydrogen defects in tetragonal zirconia.

Number of T-ZrO_2 unit cells	$1\times1\times1$	$2\times2\times2$	$3\times3\times3$	$4\times4\times4$
Number of atoms	12	96	324	786
k-points	$4\times4\times4$	$2\times2\times2$	$2\times2\times2$	$2\times2\times2$
Kinetic energy cutoff	450 eV			

The formation energy of a defect after performing finite size scaling is denoted by E_∞^f. It is obtained by fitting the raw uncorrected results from four (or more) simulation cells of different sizes to the equation:

$$E^f(L) = E_\infty^f + \frac{a}{L} + \frac{b}{L^3}, \tag{6-3}$$

where $E^f(L)$ is the uncorrected formation energy of the defect calculated from a supercell of length L which is defined as the cubic root of its volume. E_∞^f, a, and b are obtained from the fitting. We regard E_∞^f as the reference value for the formation energy of the defect and calculate the error in the results obtained from the $2\times2\times2$ supercell (with and without MP correction) with respect to this reference. Figure 6-8 summarizes the results of this procedure for the four selected defects, $H_i^\bullet$, $H_i^/$, $H_O^\bullet$, and $(H_2)_{Zr}^{////}$.

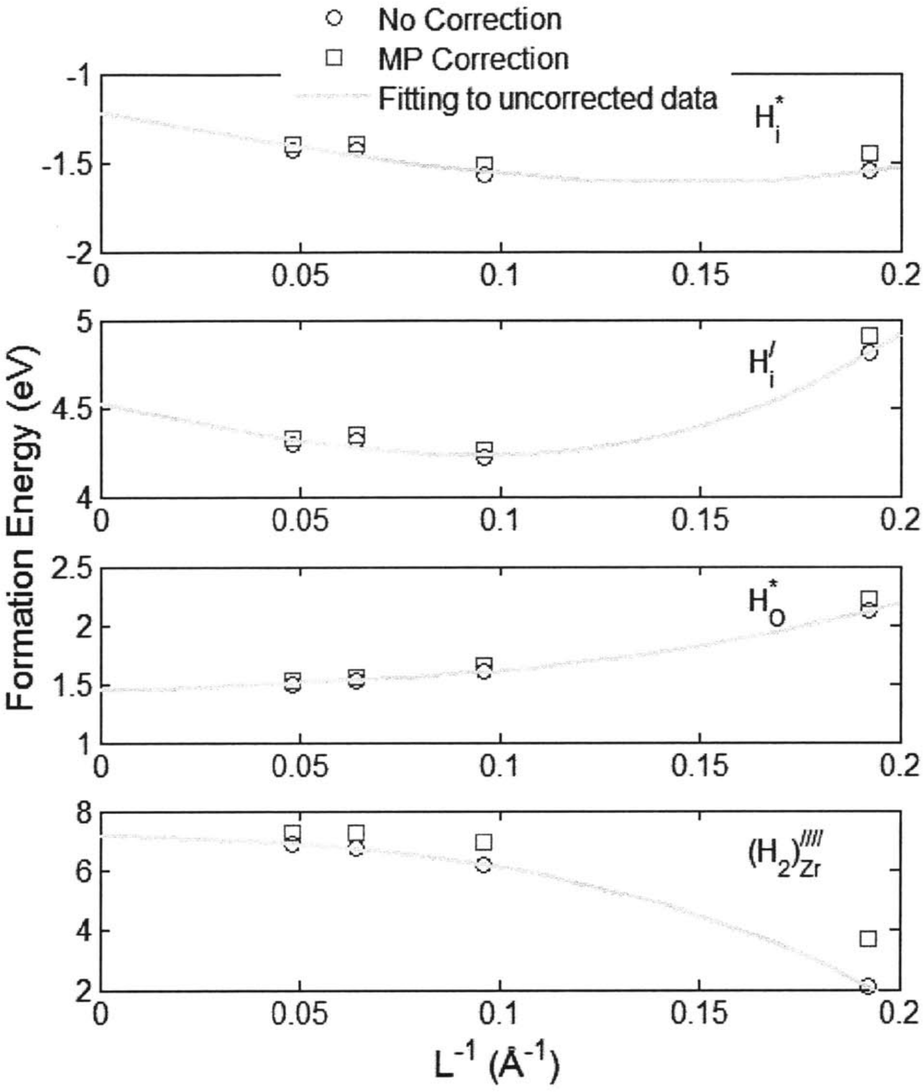

Figure 6-8: The formation energy of $H_i^\bullet$, $H_i^/$, $H_O^\bullet$, and $(H_2)_{Zr}^{////}$ obtained without correction and with the MP correction. The fitting was performed on the uncorrected results to obtain reference values.

In Table 6-8 we provide a summary for the formation energies (at zero chemical potential of electrons and in oxygen rich conditions) for the selected defects using the three schemes: finite size scaling, raw uncorrected results, and MP corrected results. We also show in the table the value of the thermodynamic transition level (+/-) for the interstitial hydrogen. In general MP correction performs reasonably well (maximum error in the formation energy is 0.3 eV) and including it is better than leaving the formation energies without any corrections at all. Finite size scaling is of course more robust, however it is computationally very expensive and indeed impractical when it comes to study 30 charged defect as in this work and for each one of the 30 we need to consider several crystallographic structures (for example 12 structures for $H_i^\bullet$ only).

Table 6-8: Summary of the values of the formation energies of the defects on which the finite size scaling was performed. These values are at zero chemical potential of electrons and in oxygen rich conditions. Also shown the (+/-) thermodynamic transition level for the interstitial hydrogen. All energies are in eV.

	Reference value obtained by finite size scaling, E_∞^f	Raw results without correction (error) $2\times2\times2$ unit cells	Makov-Payne corrected results (error) $2\times2\times2$ unit cells
$H_i^\bullet$	-1.22	-1.57 (-0.35)	-1.52 (-0.30)
$H_i^{/}$	4.53	4.22 (-0.31)	4.27 (-0.26)
$H_O^\bullet$	1.44	1.60 (0.16)	1.65 (0.21)
$(H_2)_{Zr}^{////}$	7.17	6.17 (-1.00)	6.96 (-0.21)
(+/-) for H_i	2.87	2.91 (0.04)	2.91 (0.04)

6.6 Conclusion

The energy-structure paradigm was adopted to study hydrogen defects in tetragonal ZrO2 by means of density functional theory simulations. Defect energies were analyzed by two metrics; the formation energy and a new more comprehensive definition of the binding energy of a defect complex. The atomic and electronic structures of the defects were examined utilizing Bader charge analysis, shifts in the vibrational frequencies and the DFT-calculated relaxed geometries and net spin densities.

Our results indicate that in oxygen poor conditions and for most of the values of the chemical potential of electrons, the predominant form of hydrogen defects is $H_O^\bullet$. $H_O^\bullet$ is a complex formed by the association of a hydride ion and a doubly charged oxygen vacancy. This complex is very stable thermodynamically with a binding energy of -2.22 eV. Furthermore, this observation is consistent with the proportionality between hydrogen solubility and the degree of hypostoichiometry observed experimentally in oxygen poor conditions. In oxygen rich conditions several hydrogen defects predominate depending on the chemical potential of electrons. Starting from the edge of the valence band and toward the edge of the conduction band these are, interstitial protons, then the complex $(2H)_{Zr}^{''}$, and finally for the rest of the band gap, the complex $(H_2)_{Zr}^{''''}$. The latter two complexes are thermodynamically stable with binding energies of -2.94 eV and -1.06 eV, respectively. In $(2H)_{Zr}^{''}$ the two hydrogen species exist in the zirconium vacancy in the form of hydroxyl groups, while in $(H_2)_{Zr}^{''''}$ they exist as a hydrogen molecule.

We found out that zirconium vacancies have a tendency to act as hydrogen accumulators up to three hydrogen species per vacancy. This tendency of zirconium vacancies can be a precursor for the degrading effect of hydrogen on the mechanical properties of T-ZrO_2 and the metal oxides in general.

Finally, in order to assist future experimental detection of hydrogen defects in T-ZrO_2, we calculated the shifts in the vibrational frequencies of hydroxyl groups and hydrogen molecules that can arise as hydrogen defects in T-ZrO_2 taking their gas phase frequencies as reference. Without exception, we observed that all the hydroxyl groups experience a red-shift while all the hydrogen molecules experience a blue-shift in tetragonal zirconia.

We believe that the comprehensive study presented here concerning hydrogen defects in T-ZrO_2 is a major milestone in our understanding of technologically important phenomena such as hydrogen pickup in zirconium alloys in nuclear reactors, the low temperature degradation of zirconia ceramics in biomedical applications, and the adverse effects of hydrogen on zirconia gate dielectrics.

Chapter 7 : The interplay between planar stress and hydrogen defects in tetragonal zirconium oxide

Abstract

We studied the effect of planar compressive stress on the perfect and defected (001) and (101) gains of tetragonal zirconia. For the perfect grains and up to a stain of 4%, the (001) grains exhibit linear elastic behavior while the (101) shows a relaxation at about 2% strain. Moreover these two types of grains exhibit different response to stress in the presence of defects (whether hydrogen or native). In particular for the (101) grains, the formation energies of the defects that dominate in the oxygen rich conditions is lowered by biaxial compression while the formation energies of the oxygen poor defects increase by biaxial compression. The trend for the (001) grains is the opposite. For both types of grains the underlying reason for decreasing or increasing the formation energies of the defect is the stress induced by the defect. A defect that relaxes the compression gains lower formation energy by applying compression and vice versa. A mechanism for picking up hydrogen was proposed based on these observations.

7.1 Introduction

Once the oxide on zirconium alloys exceeds a thickness of about 2 microns, the corrosion kinetics undergo an accelerating transition [10]. This transition repeats itself in a cyclic fashion as the oxide continues the growth process and is usually associated with cracks in the oxide parallel to the metal/oxide interface. Recently a strong correlation was demonstrated between the kinetics of the corrosion process and the kinetics of hydrogen pickup [78, 178]. In particular it was shown that within each corrosion cycle, hydrogen pickup has an inverse relationship with the measured weight gain in corrosion experiments. At the start of each corrosion cycle the oxidation is fast and hydrogen pickup is slow and the situation is reversed at the end of the cycle. Moreover, recent experiments discovered that right before end of the corrosion cycle the compressive stress in the tetragonal phase of the zirconium oxide (T-ZrO_2) relaxes significantly and then subsequently increases [179]. This stress evolution behavior was attributed to the tetragonal to monoclinic phase transition where initially the relaxation of the compression on the tetragonal phase leads to transforming part of it to monoclinic phase (M-ZrO_2). The newly formed M-ZrO_2 has larger volume and hence exerts compressive stress on the remaining tetragonal phase which explains the restoration of the compression on T-ZrO_2 as observed in the experiments

In this chapter we introduced "a" missing link between the observed stress evolution during the corrosion cycle and the discovered correlation between oxidation and hydrogen pickup kinetics. In particular we demonstrate through density functional theory (DFT) calculations that the formation energy of hydrogen defects in the oxygen rich part of T-ZrO_2 (the part close to the water/oxide interface) decreases significantly in the presence of biaxial compressive stress. Furthermore, we showed that the same defects are able to relax the compressive stress in T-ZrO_2. This observed interplay between certain defects and planar stress was found to apply to the gains oriented in <101> direction but to the grains oriented in <001>.[‡‡‡] We limited our investigation to these two orientations because, as reviewed in chapter 2, Motta et al. showed that all zirconium alloys that exhibit "protective" corrosion kinetics, share a common feature which is the presence of highly textured tetragonal grains oriented in (001) at the metal/oxide interface [43]. The (001) grains are limited to the first 0.3 micron of the oxide and do not exist beyond this region, while (101) grains exist throughout the oxide.

Based on these DFT calculations we hypothesized that hydrogen pickup can takes place by catalyzing a degrading tetragonal to monoclinic phase transition in the (101) tetragonal grains. Initially the compressive stress is high enough in T-ZrO_2 which thermodynamically facilitates the incorporation of hydrogen into the oxygen rich part of the oxide. Continuous accumulation of hydrogen in this part of the oxide leads to decreasing the level of compressive stress which subsequently leads to the tetragonal to monoclinic phase transition. We think that this phase transition can introduce interconnected cracks that can provide a direct path for hydrogen to the metal. This does not exclude the possibility of the diffusion of hydrogen through a coherent oxide layer; instead it provides another mechanism for hydrogen entry. Both can act synergistically.

The organization of the rest of this chapter is as follows; first we present the details of the DFT calculations. Next, we present our results for the defect-free (001) and (101) grains and then

---

[‡‡‡] Crystallographic directions in this chapter are based on the primitive cell of tetragonal zirconia. Confer Figure 4-1.

for the grains that contains both hydrogen and native defects. Finally, we present a discussion of the news findings.

7.2 Computational details

Since this chapter is built upon the comprehensive study of hydrogen defects in tetragonal zirconia presented in chapter 6, we followed exactly the same simulation details except for some exceptions due to the application of planar strain to the simulation cells. Here summarize these exceptions and explain how the strain was applied.

The kinetic energy cutoff was increased to 520 eV to avoid Pullay stress issues. We simulated the biaxial compression on (001) and (101) grains by orienting a single crystal of T-ZrO_2 such that the <001> and <101> directions are coincident with z-axis for each grain type, respectively. The biaxial strain was applied to the x-y plane in steps of 0.002 from the zero strain state up to a strain of 0.04. At each step both the ionic positions and the z-axis of the simulation cell were allowed to relax. The simulation cell contained 32 and 36 ZrO_2 formula units in the case of (001) and (101) grains, respectively. A 2x2x2 k-point grid was used to perform integrals in the reciprocal space.

The procedure described above was applied for the defect-free grains and for grains that contain the most dominant hydrogen defects both in oxygen rich conditions (oxide/water interface) and oxygen poor conditions (metal/oxide interface). As determined in chapter 6, for the oxygen rich conditions $(2H)_{Zr}^{//}, (3H)_{Zr}^{/}$, and $(H_2)_{Zr}^{////}$ predominate while for oxygen poor $H_O^{\bullet}$ predominates. For the sake of comparison we also performed simulations were the simulation cell contains one of the native defects $V_O^{\bullet\bullet}$ and $V_{Zr}^{////}$.

7.3 The interplay between hydrogen defects and the biaxial stress

7.3.1 Defect-free (001) and (101) tetragonal ZrO_2 grains under biaxial compression

Figure 7-1 depicts the atomic configurations of the (101) and (001) tetragonal grains. It is interesting to note that the area per ZrO_2 unit formula on the (101) plane is about 11.72 Å^2 while this characteristic area is about 13.28 Å^2 on the (001) plane. In other words the atomic packing density on the (101) planes is higher than on the (001) planes. Intuitively one would think that it is easier to biaxially compress the (001) planes as compared to the (101) planes but our DFT calculations surprisingly indicate the converse as we explain below.

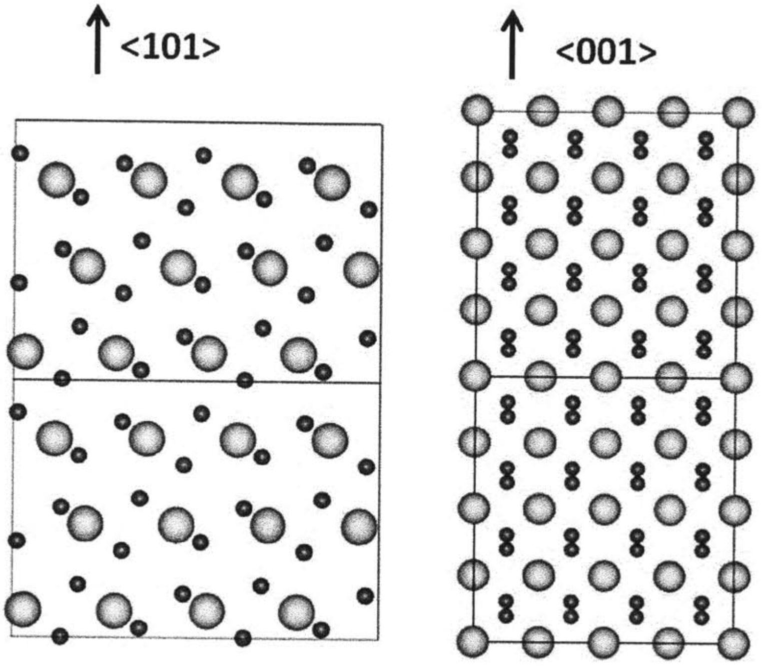

Figure 7-1: Schematic shows the simulation cell of the (101) grains (left) and the (001) grains (right). The box indicates the actual size of the DFT supercell and was doubled in z-axis for clear visualization. Green and red balls represent zirconium and oxygen, respectively.

In Figure 7-2 we present the calculated stress-strain response of both grain types. In addition, we show the change of the energy of the ZrO_2 unit formula under biaxial compression with respect to the energy of the zero strain state. The level of stress response in the (001) grains is much higher than the corresponding stress level in the (101) grains and is linear with strain all the way up to 4% strain as indicated in the figure. On the other hand, the stress level in the (101) grains reaches a value of about 2.64 GPa at a strain of 2% and decreases till 3% strain and then builds up again. Energetically it is also clear that deforming the (001) grains is more unfavorable energetically compared to the (101) grains. It is important to note that these energy changes in the figure are *not* too small to be evaluated by DFT since they are presented here on "per chemical formula" basis but indeed these changes are large enough to be adequately predicted using DFT. Again we emphasize that these results are counterintuitive considering that the (101) plains are atomically denser than (001) planes. The defect-free results hint that the response of these two types of grains to hydrogen defects will also be markedly different and this is actually the case as we present in the next subsection.

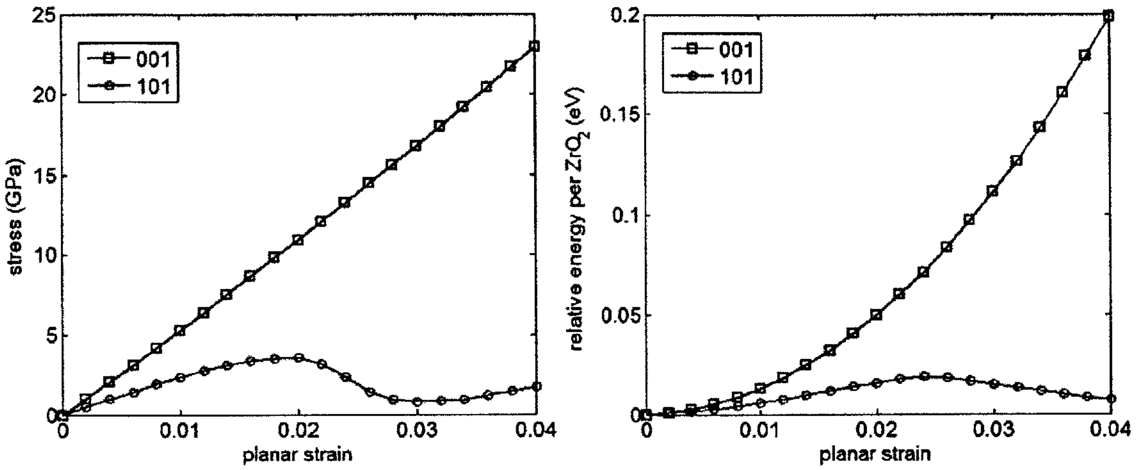

Figure 7-2: (left) The stress-strain response of the (101) and (001) grains under biaxial compression. (right) The change of the energy of the ZrO_2 chemical formula in biaxially compressed (001) and (101) grains with respect to the energy at the zero strain state.

7.3.2 Interplay between biaxial compressive stress and hydrogen defects in (001) and (101) tetragonal ZrO_2 grains

We examine the impact of biaxial compression on the formation energies of the dominant hydrogen and native defects. Figure 7-3 depicts the relative formation energy of these defects in both (001) and (101) grains as a function of applied strain with respect to the zero strain state.

For the (101) grains shown in the top part of the figure, the epitaxial compression favors the formation of the defects that predominates in oxygen rich conditions but not the ones in oxygen poor conditions. For all the defects (except $(3H)'_{Zr}$) the change in the formation energy due to strain is not significant up to a strain of about 0.014%. Beyond this strain the formation energy of the metal/oxide interface predominant defects starts increasing significantly while for the water/oxide interface defects, the formation energy starts decreasing significantly. The formation energy of the $(3H)'_{Zr}$ defect has an interesting behavior were it initially decreases upon applying the strain and then reaches a minimum at about 0.014% strain and then increases again. The changes in the formation energy shown in the figure are very significant and can lead to orders of magnitude changes in the defect concentrations.

For (001) grains, the impact of strain on the defect formation energies is reversed when we compare with the (101) grains. In particular, we can clearly see that the defects that predominate in oxygen rich conditions will be suppressed by applying compression on (001) grains while those defects that arise in oxygen poor conditions will get enhanced by applying compression. This is the converse of the trend in the (101) grains.

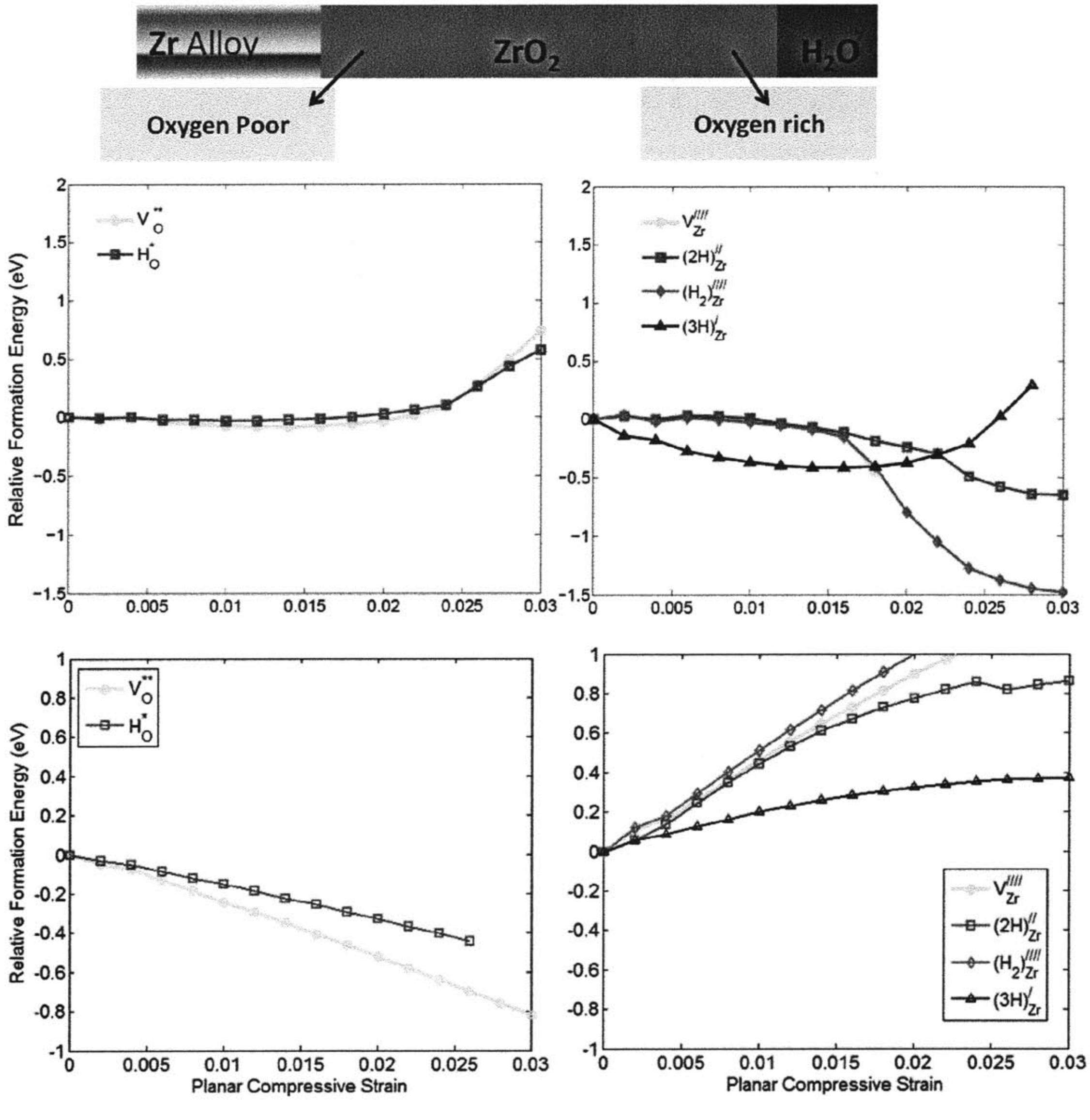

Figure 7-3: The relative formation energies of the predominant hydrogen and native defects with respect to the zero strain state. [Top] is the results of the (101) grains, [bottom] is the results of the (001) grains. [Left] is the defects that predominate in oxygen poor conditions, [right] is the defects that predominate in oxygen rich conditions.

The defect that introduces relaxation of the compressive stress in the lattice will in general be favored energetically. This can be readily seen once we consider Figure 7-4 in which we plot the stress-strain response of the defect-free T-ZrO_2 and also for T-ZrO_2 grains that contains hydrogen or native defects. In relating Figure 7-4 with Figure 7-3, we observe that any defect that leads to a stress level higher than that of the defect-free crystal would immediately be favored energetically.

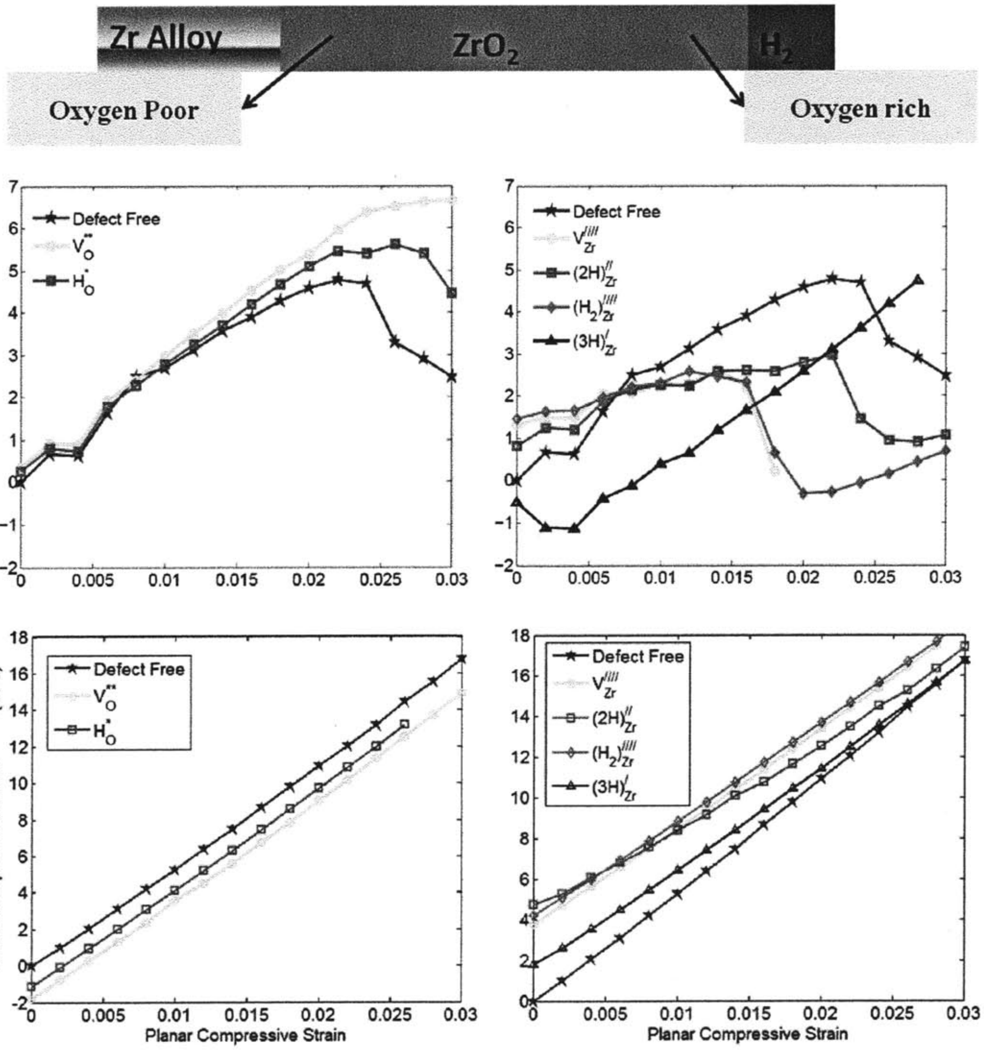

Figure 7-4: The stress-strain response for defect-free T-ZrO_2 and for T-ZrO_2 with hydrogen and native defects. [Top] is the results of the (101) grains, [bottom] is the results of the (001) grains. [Left] is the defects that predominate in oxygen poor conditions, [right] is the defects that predominate in oxygen rich conditions.

It is important to note two observations from the DFT calculations presented here. First, the defect-free (101) grains show an immediate stress relaxation at about 2% strain even though the corresponding stress level is not very high (less than 5 GPa). This is not a typical behavior of a ceramic material investigated by atomistic simulation in a defect-free setup. Indeed we checked that this behavior is special for the tetragonal crystal structure by performing the same calculations on the (001) and (101) grains of several cubic (fluorite) ceramics and on tetragonal hafnia. None of the cubic structures showed this early stage relaxation under biaxial compression on the (101) grains but tetragonal hafnia showed exactly the same behavior as tetragonal zirconia. Second, both Figure 7-3 and Figure 7-4 show that substitutional hydrogen defects follow the trends of the native defects on which they were substituted. So the oxygen-rich hydrogen defects more or less follow the behavior of the underlying zirconium vacancy while the oxygen-poor hydrogen defects adhere to the behavior of the oxygen vacancy.

7.4 Implication for the mechanism of hydrogen pickup

Based on the results presented in the previous section, we believe that hydrogen can induce the degrading tetragonal to monoclinic phase transition by acting on the (101) tetragonal grains. It is important to recall that the experiments showed that (101) grains exist throughout the oxide and are not limited to the metal/oxide interface as is the case for the (001) grains [43]. This implies that (101) grains are far from the strong constraint dictated by the metal/oxide interface lattice mismatch and thus amenable to stress relaxation by hydrogen defects. Moreover, the presence of the (101) grains throughout the oxide indicates that hydrogen have easier access to them compared to the (001) grains that resides in the metal/oxide interface. For hydrogen to reach the (001) grains, it has to diffuse through the coherent solid oxide. While for (101) grains, it could be a matter of surface-to-subsurface incorporation (without subsequent diffusion) for hydrogen to reach them. Recall that our DFT calculations indicated that hydrogen can degrade the (101) grains through the defects that arise in the oxygen-rich region that is at the water/oxide interface. This confirms the easy access of the degrading hydrogen defects to the (101) grains compared to the (001) grains.

We propose that hydrogen defects that dominate the oxygen rich part of the (101) grains in the oxide scale grown on zirconium alloys can induce the tetragonal to monoclinic phase transition by relaxing the compressive stress in the grains. This phase transition is associated with large volume expansion which can lead to cracking the oxide layer. By cracking the oxide, the underlying metal gets exposed directly to hydrogen which can then be picked up directly.

Chapter 8 : The impact of transition metal dopants on the hydrogen pickup capacity of zirconium oxide – solubility and surface reactivity

Abstract

In early 60's the nuclear industry discovered experimentally that hydrogen pickup in zirconium alloys exhibits a volcano-like shape as a function of the 3d transition metal alloying elements. The peak of the volcano is coincident with nickel, so nickel was subsequently excluded from zircaloy-4. Here we elucidate the underlying physical reason behind this volcano behavior by combining density functional theory (DFT) calculations and thermodynamic analysis of defects and electronic structure. The key is the ability of the transition metal to p-type-dope the zirconium oxide (ZrO_2) layer that grows natively on zirconium. The more p-type doping, the less the value of the chemical potential electrons (Fermi level) in the ZrO_2 is, and subsequently the more hydrogen can dissolve in ZrO_2 in the form of interstitial protons. Simultaneously, the charge transfer barrier to hydrogen on the surface is increased, and thus, the hydrogen gas evolution is expected to be suppressed. Across the 3d transition metal, our modeling showed a volcano of the solubility of hydrogen with the peak coincident on cobalt. The approach demonstrated here can be used to design hydrogen-pickup-resistant zirconium alloys starting from first principles.

8.1 Introduction

In the last two chapters we addressed the effect of hydrogen on mechanically degrading the oxide layer once it manages to reach to the bulk of the oxide. This degradation exposes the underlying metal direct to hydrogen insertion. However, one fundamental question remains; why does part of the hydrogen generated from the splitting of water molecules on the surface of zirconia manages to penetrate the oxide layer while the remaining part evolves as hydrogen gas? A closely related question is why the hydrogen pickup exhibits a volcano-like dependence when plotted as a function of the 3d transition metal alloying element as discussed in chapter 2 and as shown in Figure 8-1 below. The key to answer these questions is to consider the fate of the water molecule subsequent to its splitting on the surface of zirconia.

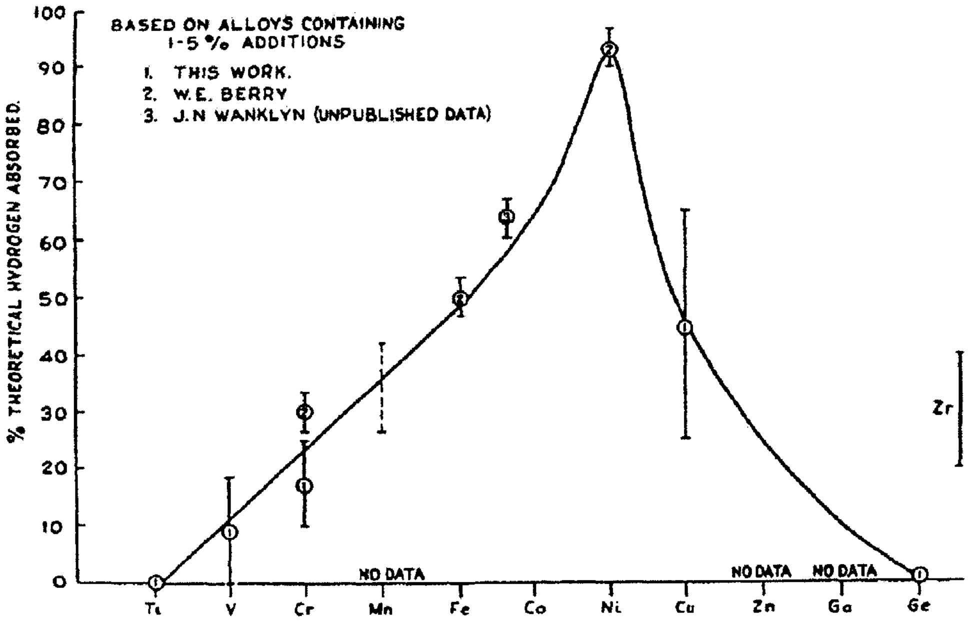

Figure 8-1: The effect of alloying elements on hydrogen pickup percentage [8].

Figure 8-2 shows schematic description of the elementary processes that can take place at the oxide/water interface. Upon the splitting of an H_2O molecule, the resulting OH^- adsorbs on a cation site forming a terminal hydroxyl group, while the H^+ adsorbs on an anion site forming a bridging hydroxyl [180]. The oxygen ion that is part of the terminal hydroxyl will eventually get into the oxide, diffuse towards the underlying zirconium metal and oxidize it. The actual mechanism is not known [15] but it is not hard to imagine that oxygen vacancies in the oxide play a major role in the mechanism of incorporating the oxide ion. Moreover the incorporation of the whole terminal hydroxyl group into the oxide is also a possibility which should not be excluded. The result on the surface is the protons that are part of the bridging hydroxyls in addition to any protons reminiscent of the terminal hydroxyls. This point is the onset of two competing scenarios. In the first scenario, these protons get incorporated into the oxide in the form of interstitial defects or via the native defects of the oxides (particularly cation vacancies). Needless to say, this is the undesirable scenario. In the second scenario, two electrons from the surface of the oxide discharge two adsorbed protons facilitating their recombination to from H_2 molecule. The presence of alloying elements in the oxide layer can promote one of these two scenarios over the other. *The goal of this work is to delineate the impact of 3d transition metals on the hydrogen pickup in monoclinic ZrO_2* utilizing the approach we developed to predict defect equilibria in a metal oxide in the limit of non-interacting defects (cf. chapter 3). The 3d transition metals include iron and chromium which are currently used in zircaloy-4, in addition they include nickel which was excluded from zircaloy-4 as it was observed experimentally to enhance the pickup of hydrogen. The choice of monoclinic zirconia (M-ZrO_2) as a host instead of the tetragonal phase is natural since it is anticipated for the monoclinic phase to dominate close to the water/oxide interface (i.e. far away from the metal/oxide interface where the tetragonal phase is stabilized by the planar strain or the low oxygen chemical potential as we showed in chapter 5).

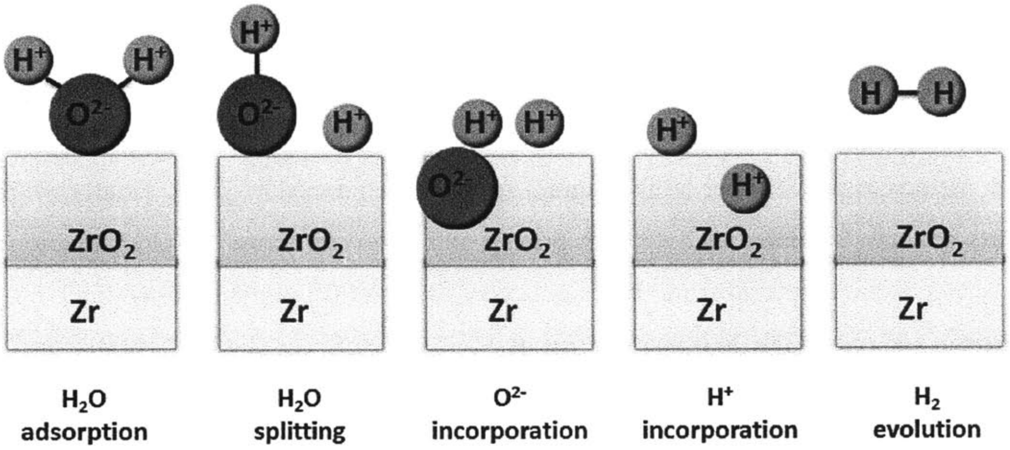

Figure 8-2: Schematics show the elementary processes that can take place at the oxide/water interface.

In particular we constructed the Kröger-Vink diagram for the hydrogen-doped M-ZrO_2. Subsequently we constructed the Kröger-Vink diagram for M-ZrO_2 co-doped with hydrogen and one of the 3d transition metals. It is known that certain alloying elements in Zr remain as secondary phase precipitates (SPP). However, the dissolution of the transition metals from the SPP (and their oxides) into the M-ZrO_2 phase is expected at high temperatures and especially under the irradiation conditions in a nuclear reactor.

This analysis allowed us to quantify the impact of the transition metal on enhancing or suppressing the solubility of hydrogen in M-ZrO_2. Our analysis revealed a volcano-like behavior for the change in hydrogen solubility in M-ZrO_2 when plotted as a function of the 3d transition metal with the peak coincident with cobalt. Further analysis showed that the underlying reason for this behavior is the extent to which the transition metal lower the chemical potential of electrons (μ_F) in monoclinic ZrO_2, i.e., the extent to which the transition metal p-type-dope M-ZrO_2. The lower μ_F, the more favorable it is for the interstitial proton to form inside M-ZrO_2 which overall increases the solubility of hydrogen in the oxide. While these results are thermodynamic in nature, they have a *kinetic incarnation*. Lowering μ_F leads to increasing the activation barrier for the transfer of free electrons from the surface of the oxide to the adsorbed protons. This is in turn increases the residence time of these protons on the surface of the oxide and hence facilitates hydrogen pickup and inhibits the evolution of H_2 gas. Thus, a transition metal dopant that lowers μ_F, will synergistically enhance the solubility of hydrogen in zirconia and increase the chance of incorporating the adsorbed protons into the oxide.

The organization of the rest of the chapter is as follows. First, we outline the computational approach which relies on the defect equilibria model introduced earlier in chapter 3. Second, we discuss the Kröger-Vink diagram for hydrogen doped M-ZrO_2. Finally we present and discuss the trends related to hydrogen pickup and observed across the 3d transition metal row. These trends are extracted from the calculated Kröger-Vink diagrams for M-ZrO_2 co-doped with hydrogen and one of the 3d transition metals.

8.2 Computational approach

8.2.1 Defect structures and charges

The same type of hydrogen defects that were modeled in tetragonal zirconia (cf. chapter 6) were also considered in monoclinic zirconia. These defects are interstitials and complexes with both anion and cation vacancies. We also considered the clustering of hydrogen in cation vacancies again along the lines of our investigations on tetragonal zirconia. The only exception is that we did not consider several orientations for every single defect as this would render the computational cost very expensive and intractable given the very asymmetric structure of monoclinic zirconia. Instead for every defect we chose only one orientation to study, guided by our work on the tetragonal phase, but allowed relaxation of all ionic and electronic degrees of freedom.

Transition metals are expected to be present in the lattice in the form of substitutional defects on the cation sites. However, we also considered interstitial defects in our simulations.

The minimum oxidation state for the transition metals were taken to be zero, that is the metallic state, while the maximum was taken from general inorganic chemistry texts (see for example [181]) and is summarized in Table 8-1.

Table 8-1: The maximum oxidation state of the 3d transition metals considered in the modeling.

Sc	Ti	V	Cr	Mn	Fe	Co	Ni	Cu	Zn
3+	4+	5+	6+	7+	6+	4+	4+	3+	2+

Charge localization on the defects was determined by performing Bader charge and spin analysis[§§§] [168, 169] and by examining isosurfaces of the DFT calculated charge density. However, contrary to hydrogen defects, transition metal defects pose a challenge to their examination using Bader charge analysis or indeed any charge analysis method. The reason is that the local charge on the transition metal site undergoes a negligible change whenever the oxidation state of the metal atom changes formally by integer values. This phenomenon was recently explained by the so-called charge self-regulation mechanism [182]. To overcome this issue, we employed a very dense grid during computing the Bader volume in order to obtain very accurate Bader charges (and spins).

8.2.2 Defect energetics and Kröger-Vink diagrams

The formalism described in detail in chapters 3 and 6 to calculate the zero Kelvin formation energies and to construct the Kröger-Vink diagram was adopted here as well. The exception is that we did not include the defect electronic entropy in the work presented here. The temperature of interest for the hydrogen pickup problem is the nuclear reactor coolant operation temperature (500-600K) and at these temperatures defect electronic entropy can be safely neglected. However, we included the vibrational free energy in our analysis which still has a non-negligible contribution even at 500K.

In constructing the Kröger-Vink diagram a reference chemical potential is needed for each element. In chapter 3 we showed how to compute the chemical potential for the native

---

[§§§] Bader spin is simply the net spin inside the Bader volume. The latter is readily computed during the evaluation of the Bader charge.

elements (Zr, O). Here we clarify the computation of the chemical potential for hydrogen and the transition metals. The chemical potential of hydrogen, μ_H, was computed as follows:

$$\mu_H(T) = \frac{1}{2}[\mu_{H_2O}(T, P_{H_2O} = 1atm) - \mu_O(T, P_{O_2} = 1atm)], \qquad (8\text{-}1)$$

where μ_{H_2O} and μ_O are corrected from thermochemical tables[94] as in chapter 3. The choice of temperature only dependent μ_H in (8-1) represents the situation where water is only located at the oxygen rich part of the oxide (water/zirconia interface) and provides the source term for all hydrogen defects throughout the oxide layer all the way up to the metal/oxide interface (oxygen poor part of the oxide).

The chemical potential for a transition metal, μ_M, was computed as follows:

$$\mu_M(T, P_{O_2}) = \frac{y}{x}[\frac{1}{y}\mu_{M_xO_y} - \mu_O(T, P_{O_2})], \qquad (8\text{-}2)$$

where $\mu_{M_xO_y}$ is the chemical potential for the metal oxide M_xO_y which is taken to be the DFT calculated energy for the chemical formula of this oxide. The choice of both T and P_{O_2} dependent chemical potential for the transition metal is consistent with the situation taking place in the zirconium alloy in the reactor. In this alloy the transition metal exists as a metallic precipitate which gets oxidized and forms the source term for the transition metal in zirconia. Since these precipitates are distributed throughout the zirconium alloy, it is expected to be present throughout the zirconia layer and hence exposed to the gradient of the chemical potential of oxygen across zirconia. In spite of this justification, all what we really need for the purpose of this particular study related to hydrogen pickup is the results in the oxygen rich part of zirconia, i.e. the results at $P_{O_2} = 1atm$. The reason is that the oxygen rich part is the closest to the interface with water were protons are adsorbed.

The reference oxide M_xO_y is not to be chosen arbitrarily. Rigorous justification for the choice of the oxide (i.e. the particular x and y) requires performing comprehensive DFT calculations coupled with finite temperature thermodynamic analysis for all the oxides known for each metal, in order to determine the one that is most stable in the thermodynamic conditions of interest. Being computationally prohibitive, we resorted to choosing the most widely known and used oxide for each metal. This is did not lead to any difficulty in the construction of the Kröger-Vink diagrams except in the case of Mn where initially chose MnO in the rock salt structure. It turns out that this highly reduced form of the manganese oxide leads to negative formation energies for Mn defects in zirconia in the oxygen rich parts of the Kröger-Vink diagram. Physically this is equivalent to say that if MnO was the only form to precipitate manganese oxide in oxygen rich condition, then it is energetically favorable for manganese defects to dissolve in zirconia rather than to precipitate as MnO. Thus, we replaced MnO with MnO_2 in the rutile structure which is a more oxidized form of manganese. Table 8-2 summarizes the reference oxides used in this study.

Table 8-2: The transition metal oxides that were used as reference states to compute the chemical potential of the transition metal.

Element	Reference Oxide	Crystal Structure of the Oxide	Magnetic Structure
Sc	Sc_2O_3	$Ia\bar{3}$ (bixbyite)	-
Ti	TiO_2	$P4_2/mnm$ (rutile)	-
V	V_2O_5	$Pmmn$	-
Cr	Cr_2O_3	$R\bar{3}c$ (corundum)	Antiferromagnetic
Mn	MnO_2	$P4_2/mnm$ (rutile)	Antiferromagnetic [a]
Fe	Fe_2O_3	$R\bar{3}c$ (corundum)	Antiferromagnetic
Co	CoO	$Fm\bar{3}m$ (rock salt)	Antiferromagnetic [b]
Ni	NiO	$Fm\bar{3}m$ (rock salt)	Antiferromagnetic [b]
Cu	Cu_2O	$Pn\bar{3}m$	-
Zn	ZnO	$P6_3mc$ (wurtzite)	-

a. This phase has a helimagnetic structure which is difficult to model, so it is approximated here by antiferromagnetic structure.

b. The so-called type-II antiferromagnetic structure.

8.2.3 Density functional theory calculations

The same calculation details used in chapter 3 and 6 were also applied in this study except that phonon calculations for the defects were performed using gamma point sampling. The monoclinic structure is very asymmetric and using $2 \times 2 \times 2$ k-point sampling was found to be very demanding.

For the transition metals, we summarize in Table 8-3 the electrons that were explicitly treated as valence electrons in the DFT calculations.

Table 8-3: Summary of the electrons that were treated as valence electrons for the transition metals.

Element	Valence
Sc	$3s^2\ 3p^6\ 4s^2\ 3d^1$
Ti	$3s^2\ 3p^6\ 4s^2\ 3d^2$
V	$3s^2\ 3p^6\ 4s^2\ 3d^3$
Cr	$3s^2\ 3p^6\ 4s^2\ 3d^4$
Mn	$3s^2\ 3p^6\ 4s^2\ 3d^5$
Fe	$3s^2\ 3p^6\ 4s^2\ 3d^6$
Co	$3s^2\ 3p^6\ 4s^2\ 3d^7$
Ni	$3p^6\ 4s^2\ 3d^8$
Cu	$3p^6\ 4s^2\ 3d^9$
Zn	$3p^6\ 4s^2\ 3d^{10}$

8.3 Hydrogen doped monoclinic ZrO_2

In this section we present the Kröger-Vink diagram for Hydrogen doped monoclinic ZrO_2 calculated at 600K which is representative of the nuclear reactor operation temperature. In all diagrams we limit the range of $\log P_{O_2}$ to the range between -15 and 0, and focus on the defects that has concentration greater than 10^{-16} per ZrO_2 chemical formula. The most relevant region in the diagrams for the problem of hydrogen pickup is the high P_{O_2} region (~ 1 am). The equilibria in this region decide the equilibrium solubility of hydrogen and the chemical potential of electrons close to the metal/oxide interface. These two quantities are crucial in deciding the pickup of hydrogen in the oxide and subsequently in the underlying metallic alloy.

Figure 8-3 depicts the calculated Kröger-Vink diagram for hydrogen doped monoclinic zirconia at 600K. Free holes, the dominant native defects in this regime of P_{O_2} in M-ZrO$_2$, are now compensated by the complex $H_{Zr}^{'''}$. The latter is a complex between a zirconium vacancy and trapped hydrogen in the vacant site in the form of a hydroxyl group. Other hydrogen defects which are still present by comparable concentrations are the interstitial proton $H_i^{\bullet}$ and the complex $(2H)_{Zr}^{''}$. The hydrogen related complexes are anticipated to be trapping sites for hydrogen that render it less mobile compared to its interstitial defects.

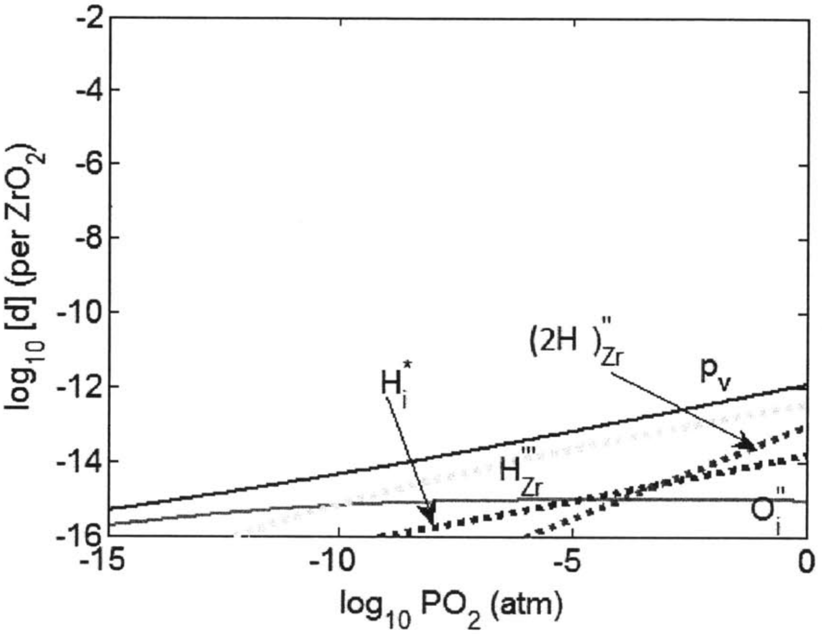

Figure 8-3: Calculated Kröger-Vink diagram for hydrogen doped monoclinic zirconia at 600K.

8.4 The origin of the hydrogen pickup volcano

The solubility of hydrogen at a given temperature and oxygen partial pressure is the weighted sum of the concentration of all hydrogen defects, where the weights are the number of hydrogen species in each defect. We extracted the solubility of hydrogen in monoclinic zirconia in the presence of 3d transition metals at P_{O_2} of 1 atm from the calculated Kröger-Vink diagrams and reported in Figure 8-4 the effect of the 3d transition metals on the solubility of hydrogen at three different temperatures. Important observations can be readily seen on the figure, which we summarize here:

1. Scandium which was not considered before to alloy zirconium for nuclear cladding (see Figure 8-1) is indeed the worst in terms of hydrogen pickup. The solubility of hydrogen increases by 4-5 orders of magnitude by doping ZrO_2 with scandium.
2. Titanium does not change the hydrogen pickup compared to the pure ZrO_2. This element dissolves in the form of Ti^{4+} substituting zirconium and hence and does not change the defect equilibria in ZrO_2 at all since it is neutral with respect to zirconium.
3. At 600K chromium indeed reduces the solubility of hydrogen compared to the pure ZrO_2.
4. Starting from Ti all the way to Zn, the solubility ratio exhibits a volcano-like shape with a peak on Cobalt. This is in line with trend observed experimentally except that the peak position is on Cobalt instead of Ni. The resolution of this difference calls for more accurate and "modern" experiments and also more accurate DFT calculations.

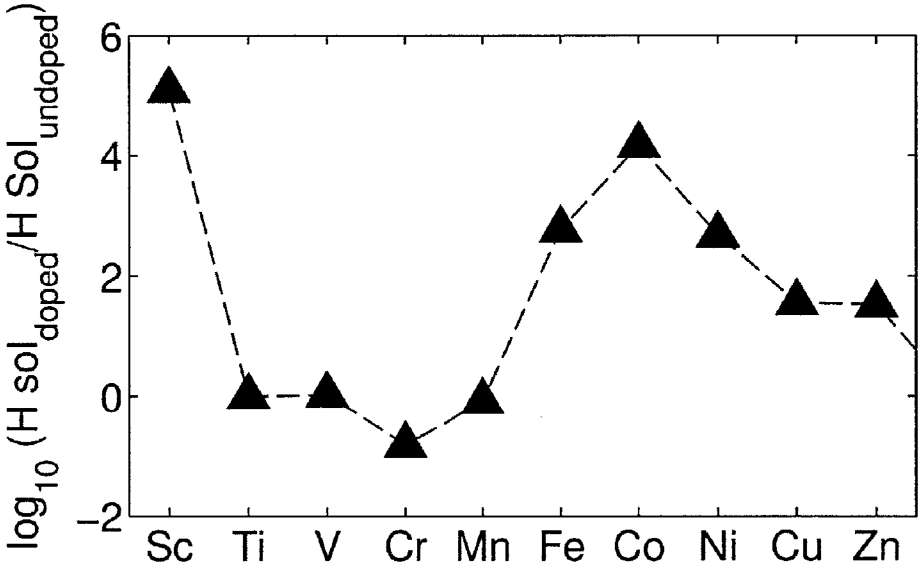

Figure 8-4: The ratio between hydrogen solubility in the transition metal doped monoclinic zirconia to the hydrogen solubility in the pure zirconia. These values were obtained from the calculated Kröger-Vink diagrams at 600 K and oxygen partial pressure of 1 atm.

In order to explain the origin of this volcano, we plot in Figure 8-5 the chemical potential of electrons (μ_F) at a 600K and P_{O_2} of 1 atm as a function of the alloying element. In the same figure we show μ_F in the absence of any alloying element. We observe that the elements who significantly increased the solubility of hydrogen are those who are able to p-type dope zirconia as much as possible (i.e. lower μ_F as much as possible). In particular in the case of Co, we found that μ_F is reduced by 0.7 eV at 600K. Such reduction in μ_F enhances the solubility of hydrogen since it reduces the formation energy of interstitial protons as show in Figure 8-6.

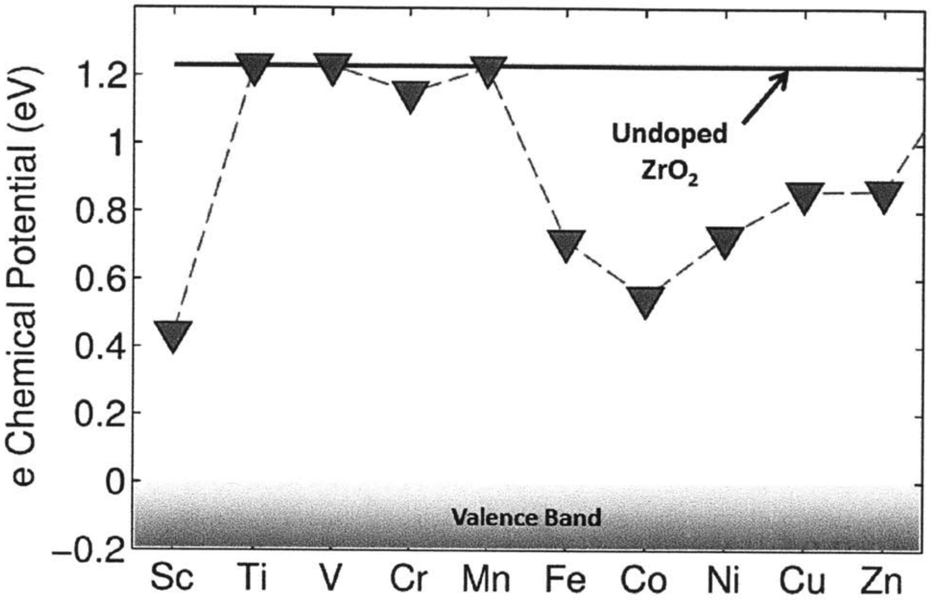

Figure 8-5: The chemical potential of electrons in the monoclinic zirconia co-doped with hydrogen and a transition metal element. The horizontal blue line shows the value of the chemical potential of electrons in pure zirconia. These values were obtained from the calculated Kröger-Vink diagrams at 600 K and oxygen partial pressure of 1 atm.

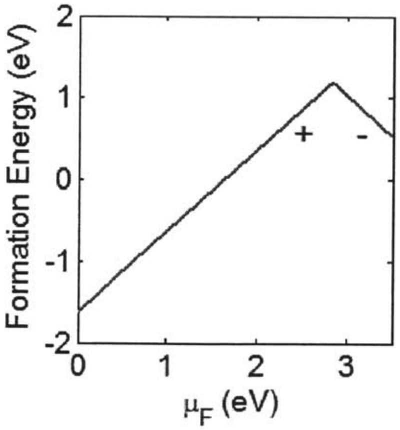

Figure 8-6: The zero kelvin formation energy of interstitial hydrogen as a function of the chemical potential of electrons. The defect is stable in two charge states; proton (+) and hydride ion (-).

The reduction of μ_F has also kinetic considerations as schematically shown in Figure 8-7. The value of μ_F compared to the energy state of the adsorbate on the surface of the oxide (adsorbed protons in our case) sets the lower bound for the energy barrier for *free* electron transfer from the surface of the oxide to the adsorbate. If this charge transfer does not take place, the hydrogen gas evolution cannot take place, and the residence time of the adsorbed protons on the surface of zirconia will increase, ultimately increasing the probability of its incorporation in the bulk of the oxide.

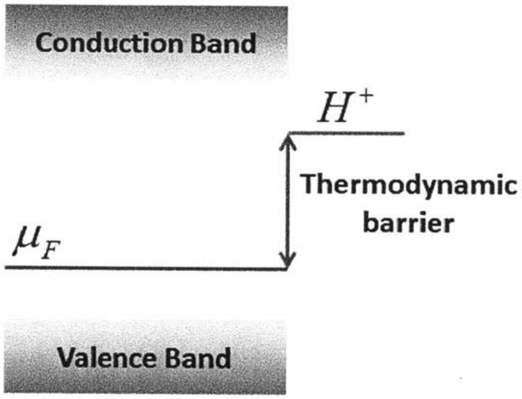

Figure 8-7: Schematic showing the thermodynamic barrier to transfer a free electron from the surface of the oxide to an adsorbed proton.

We believe that the analysis presented here gives a reasonable explanation for the observed trends for hydrogen pickup as a function of the 3d transition metals. However, it also motivates further controlled experiments in order to confirm and validated the explanation that we propose.

Chapter 9 : Epilogue

9.1 Summary

In this thesis we presented a framework to model non-interacting charged defect equilibria in a metal oxide informed by density functional theory and relying on notions of statistical mechanics. The framework was validated on the tetragonal and monoclinic phases of zirconium oxide and then applied to four problems of importance to understand the corrosion and hydrogen pickup of zirconium alloys in nuclear reactors.

The first problem is concerned with the self-diffusion of oxygen in tetragonal zirconia. We combined the predicted oxygen defects concentrations using the developed framework with the calculated migration barriers (using the Nudged Elastic Band method) to determine oxygen self-diffusivity as a function of independent thermodynamic variables such as the temperature and oxygen partial pressure. Our analysis naturally produces a spectrum of effective self-diffusion barriers as a function of oxygen partial pressure (or alternatively off-stoichiometry) providing a possible reconciliation for the scatter in the experimentally determined activation barriers for metal oxides in general. The computed self-diffusivity of oxygen in tetragonal zirconia can be fed to future macro-scale modeling of the growth of the oxide scale on zirconium alloys.

In the second application of the framework, we utilized the evaluated defect equilibria for both the monoclinic and tetragonal phases of zirconia to construct a temperature-oxygen partial pressure phase diagram. The diagram showed that the tetragonal phase can be stabilized at temperatures lower than its atmospheric transition-temperature by lowering the oxygen partial pressure. The reason is that the tetragonal phase admits more oxygen vacancies compared to the monoclinic phase. The configurational entropy of these oxygen vacancies lowers the free energy of the tetragonal phase and so stabilizes it. This analysis provides a different perspective on the stabilization of the tetragonal phase at the nuclear reactor temperature close to the metal/oxide interface on zirconium alloys. In addition to prior suggestions for the reason of this stabilization we add here that this region is oxygen poor which promotes a stabilization mechanism for the tetragonal phase.

Third, in 1960 the nuclear industry discovered that the hydrogen pickup of zirconium alloys exhibits a volcano-like dependence on the first raw transition metals that are used to alloy zirconium. This empirical discovery was utilized in the design of more resistant alloys but was never explained on physical grounds. Here we applied the developed defect equilibria formalism to model monoclinic zirconia co-doped with hydrogen and a first raw transition metal. The modeling revealed that the solubility of hydrogen exhibits a similar volcano-like dependence on the first raw transition metals. This was found to be related to the ability of the transition metal to p-type-dope zirconia by lowering the chemical potential of electrons. In particular, the metals on the top of the volcano (Fe, Co, Ni) are the ones that can minimize the chemical potential of electrons in zirconia. This, in turn, lowers the formation energy of interstitial protons and thus increases the solubility of hydrogen in zirconia. Moreover, this thermodynamic analysis has a kinetic flavor as well. Lowering the chemical potential of electrons also corresponds to increasing the activation barrier for the free electron transfer from zirconia to the adsorbed protons. This would obstruct the discharging of the adsorbed protons and the evolution of H_2 gas. The overall result is that the metals on the top of the volcano enhance the hydrogen pickup by facilitating the solubility of hydrogen and obstructing the charge transfer on the surface of zirconia. This physics-based explanation can open the door to design resistant zirconium alloys starting from first-principles. Moreover, it is much more efficient and economical to computationally screen dopants to design hydrogen-pickup-resistant alloys than to actually perform expensive experiments. The search space can be significantly broadened if one considers combinations of dopants and in that case, modeling and simulation, as demonstrated here, can help in down-selecting the most promising candidate combinations. These candidates can be subsequently tested experimentally.

Finally, we discovered a marked interplay between certain hydrogen defects in tetragonal zirconia and the planar compressive stress that this phase experiences in the nuclear reactor at the metal/oxide interface on zirconium alloys. We found out that the stress reduces the formation energies of these defects and in return these defects tend to relax the compressive stress. We proposed based on this interplay a hypothesis for the mechanism by which hydrogen can enter the zirconium alloy. First, these defects become abundant in the tetragonal zirconia under the influence of the stress, and then these very defects relax the compressive stress. The stress relaxation leads to the tetragonal-monoclinic phase transition which is accompanied by large volume expansion and crack generation. Cracking the oxide directly exposes the underlying metal to hydrogen leading to hydrogen pickup.

9.2 Suggested future directions

I believe that the framework presented in this thesis to model the equilibria of non-interacting charged defects in metal oxides can be further advanced, improved and coupled with other approaches to solve more challenging problems in the realm of materials physics and chemistry. Here I propose few future directions:

1. The density functional theory calculations that are needed to feed the framework can be obtained by more accurate computationally intensive exchange-correlation functionals. While we believe that for zirconium oxide standard PBE functional is sufficient to capture the essence of the electronic structure of its defects, for other metal oxides this might not be the case especially for strongly-correlated oxides. A more balanced approach would be to use standard PBE so sample the electronic structure of a large number of possible point defects, and then based on PBE results we can down-select a few of the most important defects to study them with more accurate approaches. This line of thinking was also suggested by J. Perdew [183].
2. There is also a room to improve the sampling of finite temperature effects and to consider more of these effects as well. In particular, throughout this work we relied on the harmonic approximation to model the vibrational free energy of the solid. We also showed that this approach can have a shortcoming at very high temperatures when it comes to predict the solid-solid phase transition temperature (cf. chapter 5). It is possible to resort to more expensive methods such as the quasi-harmonic approach. Again I believe a more balanced approach is to first sample a large number of defects using the harmonic approximation and then focus on the most important ones using a quasi-harmonic approximation. Moreover, there are some finite temperature excitations which we did not consider here either because they are not relevant to zirconia, or they are very computationally expensive to determine. Two examples I can mention here are the configurational electronic entropy of the point defect and the dependence of the band gap

on temperature. The first is actually not relevant to zirconia since none of its dominant defects is associated with localized polarons which can lead to a configurational electronic entropy contribution to the free energy of formation of the defect. This, however, is relevant to other oxides such CeO_2 where its most dominant defect, that is the oxygen vacancy, is associated with two localized electrons. The second example, the change of the band gap with temperature, is relevant to all materials but is very expensive computationally to determine. With the advance in computational power, sampling such excitations can be possible.

3. The approach we presented here targets the limit of non-interacting defects. This is very sufficient for oxides that do not exhibit large deviations from stoichiometric compositions such as ZrO_2 and MgO. However, other oxides exhibit large stoichiometric compositions such as UO_2 and CeO_2. There are techniques to model the interaction between defects that have large concentrations, for example the cluster expansion combined with Monte Carlo which was recently used to model the thermodynamics of oxygen vacancies in CeO_2 [184]. These interacting defects technique are inefficient to sample the dilute limit. Conversely, the dilute limit technique is inaccurate when the concentration of the defects increases significantly. Linking the two approaches can lead to successful modeling of oxides such as UO_2 and CeO_2 starting from fully stoichiometric compositions and spanning the whole off-stoichiometry spectrum.
4. The approach we presented in this thesis to model the defect equilibria in the bulk of a metal oxide can be used to set a necessary boundary condition to model the defect equilibria at an extended defect such as a grain boundary or a dislocation. The idea is to apply the herein developed framework at the bulk of the oxide and at the core of the extended defect and then connect these two boundary conditions by Poisson-Boltzmann equation. This approach was recently applied to model the defect equilibria at a grain boundary [131] in $BaZrO_3$ without finite temperature effects. Adding the missing finite temperature ingredient to this modeling idea can improve its predictions and reliability.
5. Finally, and I believe this is the most challenging, is to use the framework developed in this thesis to set a necessary boundary condition to model the defect equilibria close to a metal oxide/gas or a metal oxide/liquid interface. The idea is similar to what discussed in

the previous suggestion above. The difficulty here stems from two factors. First, it has been very challenging to model charged defects at the surface of a solid due to electrostatic convergence issues. However, very recently a correction was suggested to resolve this problem and successfully applied to model charged defects on the surface of NaCl [185]. The second difficulty arises from the lack of understanding how the gas or the liquid sets a boundary condition for the defect equilibria in the solid. This is even more pronounced when the gas (or the liquid) and the solid have a common element (for example O_2 gas and ZrO_2 have oxygen in common). There have been recent attempts to model this boundary condition [130] . We believe that ensuring that these two issues have been rigorously address, and then developing an overarching framework to model the defect equilibria at nonhomogeneous interfaces will have a great impact on the science and technology of metal oxides.

Bibliography

[1] C. Wagner, Schottky, Z. Physik. Chem., B11 (1931) 163.

[2] F.A. Kröger, H.J. Vink, Solid State Physics, 3 (1956) 307.

[3] C.V.d. Walle, J. Neugebauer, J. App. Phys., 95 (2004) 3851.

[4] J.-P. Crocombette, D. Torumba, A. Chartier, Phys. Rev. B, 83 (2011) 184107.

[5] S. Kasamatsu, T. Tada, S. Watanabe, Solid State Ionics, 183 (2011) 20.

[6] A.F. Kohan, G. Ceder, D. Morgan, C.G.V.d. Walle, Phys. Rev. B, 61 (2000) 15019.

[7] G. Henkelman, B.P. Uberuaga, H. Jónsson, J. Chem. Phys., 113 (2000) 9901.

[8] B. Cox, M.J. Davies, A.D. Dent, The Oxidation and corrosion of zirconium and its alloys, Part X., Hydrogen Absorption during oxidation in steam and aqueous solutions, in, HARWELL, 1960.

[9] J.L. Gavartin, D.M. Ramo, A.L. Shluger, G. Bersuker, B.H. Lee, App. Phys. Lett., 89 (2006) 082908.

[10] B. Cox, J. Nuc. Mat., 336 (2005) 331.

[11] "Waterside corrosion of zirconium alloys in nuclear power plants", TECDOC-996 International Atomic Energy Agency, 1998.

[12] E. Hillner, D.G. Franklin, J.D. Smee, J. Nuc. Mat., 278 (2000) 334.

[13] P. Billot, S. Yagnik, N. Ramasubramanian, J. Peybernes, D. Pecheur, J. ASTM Intl., 1423 (2002) 169.

[14] X. Guo, Chem. Mater., 16 (2004) 3988.

[15] J. Chevalier, L. Gremillard, A.V. Virkar, D.R. Clarke, J. Am. Ceram. Soc., 92 (2009) 1901.

[16] C. Angel, "Modified Oxygen and Hydrogen Transport in Zr-Based Oxides", PhD thesis, Royal Institute of Technology, Sweden, 2006.

[17] I. Wolsey, J. Morris, Corrosion, 37 (1981) 575.

[18] B. Cox, J.P. Pemsler, J. Nuc. Mat., 28 (1968) 73.

[19] J.L. Whitton, J. Electrochem. Soc., 115 (1968) 58.

[20] M. Houssa, M. Tuominen, M. Naili, V. Afanas'ev, A. Stesmans, S. Haukka, M. Hynes, J. App. Phys., 87 (2000) 8615.

[21] C. Degueldre, A. Amato, G. Bart, Scripta Mater., 54 (2006) 1211.

[22] N. Igawa, Y. Ishii, J. Am. Ceram. Soc., 84 (2001) 1169.

[23] G. Fadda, L. Colombo, G. Zanzotto, Phys. Rev. B, 79 (2009) 214102.

[24] J.X. Zheng, G. Ceder, T. Maxisch, W.K. Chim, W.K. Choi, Phys. Rev. B, 75 (2007) 104112.

[25] A. Foster, V. Sulimov, F. Gejo, A. Shluger, R. Nieminen, Phys. Rev. B, 64 (2001) 224108.

[26] A. Eichler, Phys. Rev. B, 64 (2001) 174103.

[27] A. Foster, A.L. Shluger, R.M. Nieminen, Phys. Rev. Lett., 89 (2002) 225901.

[28] A.A. Safonov, A.A. Bagatur'yants, A.A. Korkin, Microelectron. Eng., 69 (2003) 629.

[29] U. Brossmann, R. Wurschum, U. Sodervall, H.-E. Shaefer, J. App. Phys., 85 (1999) 7646.

[30] K. Park, D.R. Olander, J. Electrochem. Soc., 138 (1991) 1155-1159.

[31] T. Duong, A. Limarga, D. Clarke, J. Am. Ceram. Soc., 92 (2009) 2731.

[32] S. Abolhassani, R. Restani, T. Rebac, F. Groeshel, W. Hoffelner, G. Bart, W. Goll, F. Aeschbach, J. ASTM Intl., 1467 (2004) 467.

[33] K. Otsuka, A. Kuwabara, A. Nakamura, T. Yamamoto, K. Matsunaga, Y. Ikuhara, App. Phys. Lett., 82 (2003) 877.

[34] P. Billot, J.-C. Robin, A. Giordano, J. Peybernes, J. Thomazet, H. Amanrich, J. ASTM Intl., 1245 (1994) 351.

[35] X. Zhou, Q. Li, M. Yao, W. Liu, Y. Chu, J. ASTM Intl., 1505 (2009) 360.

[36] D. Marrocchelli, B. Yildiz, J. Phys. Chem. C, 116 (2012) 2411.

[37] N. Ramasubramanian, P.V. Balakrishnan, J. ASTM Intl., 1245 (1994) 378.

[38] O. Melikhova, J. Kuriplach, J. Cizek, I. Prochazka, G. Brauer, W. Anwand, J. Phys. Conf. Ser., 225 (2010) 012035.

[39] M. Kilo, R. Jackson, G. Borchardt, Philos. Mag., 83 (2003) 3309.

[40] N.G. Petrik, A.B. Alexandrov, I. Vall, J. Phys. Chem. B, 105 (2001) 5935.

[41] J. Medvedeva, A. Freeman, C. Geller, D. Rishel, Phys. Rev. B, 76 (2007) 235115.

[42] T. Nishizaki, M. Okui, K. Kurosaki, M. Uno, S. Yamanaka, K. Takeda, H. Anada, J. All. Comp., 330-332 (2002) 307.

[43] A.T. Motta, M.J.G.d. Silva, A. Yilmazbayhan, R.J. Comstock, Z. Cai, B. Lai, J. ASTM Intl., 1505 (2009) 486.

[44] L.-G. Liu, J. Phys. Chem. Solids, 41 (1980) 331.

[45] P. Bouvier, J. Godlewski, G. Lucanzeau, J. Nuc. Mat., 300 (2002) 118.

[46] S. Sankaranarayan, E. Kaxiras, S. Ramanathan, Energy and Environ. Sci, 2 (2009) 1196.

[47] W. Qin, C. Nam, H. Li, J. Szpunar, Acta Mater., 55 (2007) 1695.

[48] A. Yilmazbayhan, E. Breval, A.T. Motta, R.J. Comstock, J. Nuc. Mat., 349 (2006) 265.

[49] A. Yilmazbayhan, A. Motta, R. Comstock, G. Sabol, B. Lai, Z. Cai, J. Nuc. Mat., 324 (2004) 6.

[50] V. Bouineau, A. Ambard, G. Benier, F. Pecheur, J. Godlewski, L. Fayette, T. Duverneix, J. ASTM Intl., 1505 (2009) 405.

[51] Y.-S. Kim, Y.-H. Jeong, J.-N. Jang, J. Nuc. Mat., 412 (2011) 217.

[52] Q.V. Overmeere, J. Proost, Electrochim. Acta, 56 (2011) 10507.

[53] C. Roy, G. David, J. Nuc. Mat., 37 (1970) 71.

[54] H. Coriou, L. Grall, J. Munier, M. Pelras, H. Willermoz, J. Nuc. Mat., 7 (1962) 320.

[55] D. Pecheur, J. Godlewski, P. Billot, J. Thomazet, J. ASTM Intl., 1295 (1996) 94.

[56] A. Perkins, R. Busch, J. ASTM Intl., 1132 (1991) 595.

[57] B. Cox, J. Nuc. Mat., 249 (1997) 87.

[58] M. Okarsson, E. Ahlberg, K. Pettersson, J. Nuc. Mat., 295 (2001) 126.

[59] M. Vijayakumar, S. Kerisit, C. Wang, Z. Nie, K. Rosso, Z. Yang, G. Graff, J. Liu, J. Hu, J. Phys. Chem. C, 113 (2009) 2009.

[60] K. Jonsson, G.A. Nikalsson, M. Ritala, M. Leskela, K. Kukli, J. Electrochem. Soc., (2004) F54.

[61] N. Ramasubramanian, P. Billot, S. Yagnik, J. ASTM Intl., 1423 (2002) 222.

[62] F. Garzarolli, H. Siedel, R. Tricot, J. Gros, J. ASTM Intl., 1132 (1991) 395.

[63] D. Pecheur, V. Filippov, A. Bateev, J. Ivanov, J. ASTM Intl., 1423 (2002) 135.

[64] J. Godlewski, J. ASTM Intl., 1245 (1994) 663.

[65] K. Jung, E. Lee, K. Lee, J. All. Comp., 421 (2006) 179.

[66] Z. Huang, Z. Guo, A. Calka, D. Wexler, C. Lukey, H. Liu, J. All. Comp., 422 (2006) 299.

[67] P. Rudling, G. Wikmark, J. Nuc. Mat., 265 (1999) 44.

[68] E. Hillner, J. ASTM Intl., 633 (1977) 211.

[69] G. Berna, C. Beyer, K. Davis, D. Lanning, FRAPCON-3: A computer Code for the Calculation of Steady-State Thermal-Mechanical Behavior of Oxide Fuel Rods for High Burnup, NUREG/CR-6534, vol. 2, PNNL-11513 v.2, Pacific Northwest National Laboratory, Richland, WA, 1997.

[70] Y. Hatano, R. Hitaka, M. Sugisaki, M. Hayashi, J. Nuc. Mat., 248 (1997) 311.

[71] H. Anada, K. Takeda, S. Nasu, Y. Kobayashi, T. Nakamichi, J. ASTM Intl., 1423 (2002) 135.

[72] B. Lim, H. Hong, K. Lee, J. Nuc. Mat., 312 (2003) 134.

[73] M. Miyake, M. Uno, S. Yamanaka, J. Nuc. Mat., 270 (1999) 233.

[74] B. Warr, M. Elmoselhi, S. Newcomb, N. McIntyre, A. Brennenstuhl, P. Lichtenberger, J. ASTM Intl., (1991).

[75] T. Maekawa, M. Terada, Transactions of the Japan Institute of Metals, 4 (1963) 47.

[76] H. Avila-Paredes, C.-T. Chen, S. Wang, R.D. Souza, M. Martin, Z. Munir, S. Kim, J. Mater. Chem., 20 (2010) 10110.

[77] D. Khatamian, F. Manchester, J. Nuc. Mat., 166 (1989) 300.

[78] M. Harada, R. Wakamatsu, J. ASTM Intl., 1505 (2009) 384.

[79] M. Youssef, B. Yildiz, Phys. Rev. B, 86 (2012) 144109.

[80] A. Cheroneos, B. Yildiz, A. Tarancon, D. Parfitt, J. Kilner, Energy and Environ. Sci, 4 (2011) 2774.

[81] W.C. Maskell, Solid State Ionics, 134 (2000) 43.

[82] U. Schulz, C. Leyens, K. Fritscher, M. Peters, B. Saruhan-brings, O. Lavigne, J.M. Dorvaux, M. Poulain, R. Merval, M. Caliez, Aeroscpace Sci. Technol., 7 (2003) 73.

[83] A.L.Shluger, A. Foster, J.L. Gavartin, P.V. Sushko, in Nano and Giga Challenges in Microelectronics, edited by J. Greer, A. Korkin, and J. Labanowski (Elsevier, Amsterdam, 2003).

[84] B. Cales, Clin. Orthopaed. Relat. Res., 379 (2000) 94.

[85] I. Denry, J.R. Kelly, Dent. Mater., 24 (2008) 299.

[86] S. Hull, Rep. Prog. Phys., 67 (2004) 1233.

[87] A. Kushima, B. Yildiz, J. Mater. Chem., 20 (2010) 4809.

[88] Y.-M. Chiang, I. D. P. Birnie, W.D. Kingery, Physical Ceramics: Principles for Ceramic Science and Engineering, John Wiley & Sons, New York, 1997.

[89] G. Makov, M.C. Payne, Phys. Rev. B, 51 (1995) 4014.

[90] M. Leslie, M.J. Gillan, J. Phys. C, 18 (1985) 973.

[91] A. Dwivedi, A.N. Cormack, Philos. Mag. A, 61 (1990) 1.

[92] X. Zhao, D. Vanderbilt, Phys. Rev. B, 65 (2002) 075105.

[93] D.S. Sholl, J.A. Steckel, Density Functional Theory: A practical Introduction, Wiley & Sons, Hoboken, N. J., 2009.

[94] J. M. W. Chase, NIST-JANAF Thermochemical Tables, American Institute of Physics, Woodbury, N. Y., 1998.

[95] N. Aschcroft, N. Mermin, Solid State Physics, Brooks/Cole, Belmont, 1976.

[96] F. Zhou, T. Maxisch, G. Ceder, Phys. Rev. Lett., 97 (2006) 155704.

[97] B.T. Webber, M.C. Per, D.W. Drumm, L.C.L. Hollenberg, S.P. Russo, Phys. Rev. B, (2012) 014102.

[98] C. Wolverton, A. Zunger, Phys. Rev. B, 52 (1995) 8813.

[99] R. Pässler, J. App. Phys., 89 (2001) 6235.

[100] G. Kresse, J. Joubert, Phys. Rev. B, 59 (1999) 1758.

[101] G. Kresse, J. Hafner, Phys. Rev. B, 47 (1993) 558.

[102] G. Kresse, J. Hafner, Phys. Rev. B, 49 (1994) 14251.

[103] G. Kresse, J. Furthmüller, Phys. Rev. B, 54 (1996) 11169.

[104] G. Kresse, J. Furthmüller, Comput. Mater. Sci, 6 (1996) 15.

[105] J.P. Perdew, K. Burke, M. Ernzerhof, Phys. Rev. Lett., 77 (1996) 3865.

[106] J.P. Perdew, K. Burke, M. Ernzerhof, Phys. Rev. Lett., 78 (1997) 1396.

[107] D.W. McComb, Phys. Rev. B, 54 (1996) 7094.

[108] R.H. French, S.J. Glass, F.S. Ohuchi, Y.N. Xu, W. Ching, Phys. Rev. B, 49 (1994) 5133.

[109] V.I. Anisimov, F. Aryasetiawan, J. Phys. Condens. Matter, 9 (1997) 767.

[110] R. Ramprasad, H. Zhu, P. Rinke, M. Scheffler, Phys. Rev. Lett., 108 (2012) 066404.

[111] A.P. Scott, L. Random, J. Phys. Chem., 100 (1996) 16502.

[112] H. Tuller, S. Bishop, Annu. Rev. Mater. Res., 41 (2011) 269.

[113] P. Blöchl, O. Jepsen, O.K. Andersen, Phys. Rev. B, 49 (1994) 16223.

[114] A. Togo, F. Oba, I. Tanaka, Phys. Rev. B, 78 (2008) 134106.

[115] S.F.J. Cox, J.L. Gavartin, J.S. Lord, S.P. Cottrel, J.M. Gil, H.V. Alberto, J.P. Duarte, R.C. Vilao, N.A.d. Campos, D.J. Keeble, E.A. Davis, M. Charlton, D.P.v.d. Werf, J. Phys.: Condens. Matter, 18 (2006) 1079.

[116] G. Mahan, Solid State Ionics, 1 (1980) 29.

[117] M. Ganduglia-Pirovano, A. Hofmann, J. Sauer, Surf. Sci. Rep., 62 (2007) 219.

[118] W. Wang, D. Olander, J. Am. Ceram. Soc., 76 (1993) 1242.

[119] J. Xue, J. Electrochem. Soc., 138 (1991) 36C.

[120] P. Kofstad, D.J. Ruzicka, J. Electrochem. Soc., 110 (1963) 181.

[121] R.W. Vest, N.M. Tallan, J. Am. Ceram. Soc., 48 (1965) 472.

[122] L.A. McClaine, C.P. Coppel, J. Electrochem. Soc., 113 (1966) 80.

[123] A. Guillot, M. Anthony, J. Sol. Stat. Chem., 15 (1975) 89.

[124] J.L.M. Rupp, Solid State Ionics, 207 (2011) 1.

[125] D. Shrader, S.M. Khalil, T. Gerczak, T.R. Allen, A.J. Heim, I. Szlufarska, D. Morgan, J. Nuc. Mat., 408 (2011) 257.

[126] L. Wang, T. Maxisch, G. Ceder, Phys. Rev. B, 73 (2006) 195107.

[127] P.S. Archana, R. Jose, M.M. Yusoff, S. Ramakrishna, App. Phys. Lett., 98 (2011) 152106.

[128] A.C. Carniglia, S.D. Brown, T.F. Shroeder, J. Am. Ceram. Soc., 54 (1971) 13.

[129] J. Bisquert, J. Phys. Chem. C, 111 (2007) 17163.

[130] A.R. Hassan, A. El-Azab, C. Yablinsky, T. Allen, Journal of Solid State Chemistry, 204 (2013) 136-145.

[131] J.M. Polfus, K. Toyoura, F. Oba, I. Tanaka, R. Haugsrud, Physical Chemistry Chemical Physics, 14 (2012) 12339-12346.

[132] D. Simeone, G. Baldinozzi, D. Gosser, S. LeCaër, L. Mazerolles, Phys. Rev. B, 70 (2004) 134116.

[133] J.L. Lyons, A. Janotti, C.G.V.d. Walle, Microelectronic Engineering, 88 (2011) 1452.

[134] J. Zippel, M. Lorenz, A. Setzer, G. Wagner, N. Sobolev, P. Esquinazi, M. Grundmann, Phys. Rev. B, 82 (2010) 125209.

[135] A. Kumar, D. Rajdev, D.L. Douglass, J. Am. Ceram. Soc., 55 (1972) 439.

[136] C.W.M. Castleton, A. Höglund, S. Mirbt, Phys. Rev. B, 73 (2006) 035215.

[137] O. Kubaschewski, C.B. Alcock, P.I. Spencer, Materials Thermochemistry, Pergamon Press, Oxford, 1993.

[138] A. Janotti, C.G.V.d. Walle, Phys. Rev. B, 76 (2007) 165202.

[139] J.H. Harding, Rep. Prog. Phys., 53 (1990) 1403.

[140] P. Erhart, K. Albe, Phys. Rev. B, 73 (2006) 115207.

[141] G.E. Murch, in Diffusion in Crystalline Solids, edited by G. E. Murch, and A. S. Nowick (Academic Press, Orlando, 1984).

[142] G. Roma, Y. Limoge, S. Baroni, Phys. Rev. Lett., (2001) 4564.

[143] G.H. Vineyard, J. Phys. Chem. Solids, 3 (1957) 121-127.

[144] D.A. Andersson, T. Watanabe, C. Deo, B.P. Uberuaga, Phys. Rev. B, 80 (2009) 060101 (R).

[145] M. Sternik, K. Parlinski, J. Chem. Phys., 122 (2005) 064707.

[146] X. Luo, W. Zhou, S. Ushakov, A. Navrotsky, A. Demkon, Phys. Rev. B, 80 (2009) 134119.

[147] A. Kuwabara, T. Tohei, T. Yamamoto, I. Tanaka, Phys. Rev. B, 71 (2005) 064301.

[148] H.J.T. Ellingham, J. Soc. Chem. Ind., London, 63 (1944) 125.

[149] McQuarrie, Statistical Mechanics, University Science Books, Sausalito, 2000.

[150] A. Samanta, W. E., S.B. Zhang, Phys. Rev. B, 86 (2012) 195107.

[151] J.P. Coughlin, E.G. King, J. Am. Ceram. Soc., 72 (1950) 2262.

[152] M. Yashima, T. Mitsuhashi, H. Takashina, M. Kakihana, T. Ikegami, M. Yoshimura, J. Am. Ceram. Soc., 78 (1995) 2225.

[153] T. Smith, J. Nuc. Mat., 18 (1966) 323.

[154] B. Cox, J. Nuc. Mat., 264 (1999).

[155] J. Kang, E.-C. Lee, K.J. Chang, Y.-G. Jin, App. Phys. Lett., 84 (2004) 3894.

[156] G.D. Wilk, R.M. Wallace, J.M. Anthony, J. Appl. Phys., 89 (2001) 5243.

[157] K. Park, D.R. Olander, J. Am. Ceram. Soc., 74 (1991) 72.

[158] A. Janotti, G.G.V.d. Walle, Nature Mater., 6 (2007) 44.

[159] B. Malki, O.L. Bacq, A. Pasturel, J. Nuc. Mat., 416 (2011) 362.

[160] J.B. Varley, H. Peelaers, A. Janotti, C.G.V.d. Walle, J. Phys.: Condens. Matter, 23 (2011) 334212.

[161] C.G.V.d. Walle, J.P. Goss, Mater. Sci. Eng., B58 (1997) 17.

[162] C.G.V.D. Walle, Phys. Rev. B, 56 (1997) R10020.

[163] C.G.V.d. Walle, Phys. Rev. Lett., 85 (2000) 1012.

[164] C.G.V.d. Walle, J. Neugebauer, Nature, 423 (2003) 626.

[165] A.G. Marinopoulos, Phys. Rev. B, 86 (2012) 155144.

[166] A.M. Stoneham, J. Gavartin, A. L.Shluger, A.V. Kimmel, D.M. Ramo, H.M. Rønnow, G. Aeppli, C. Renner, J. Phys.: Condens. Matter, 19 (2007) 255208.

[167] F. Oba, A. Togo, I. Tanaka, J. Paier, G. Kresse, Phys. Rev. B, 77 (2008) 245202.

[168] R.F.W. Bader, Chem. Rev., 91 (1991) 893.

[169] W. Tang, E. Sanville, G. Henkelman, J. Phys.: Compute. Mater., 21 (2009) 084204.

[170] S.N. Rashkeev, K.W. Sohlberg, S. Zhuo, S.T. Pantelides, J. Phys. Chem. C, 111 (2007) 7175.

[171] B.P. Stoicheff, Can. J. Phys., 35 (1957) 730.

[172] J.C. Owrutsky, N.H. Rosenbaum, L.M. Tack, R.J. Saykally, J. Chem. Phys., 83 (1985) 5338.

[173] D.O. Scanlon, G. Watson, Phys. Rev. Lett., 106 (2011) 186403.

[174] T. Merle-Méjean, P. Barberis, S.B. Othmane, F. Nardou, P.E. Quintard, J. Eur. Ceram. Soc., 18 (1998) 1579.

[175] P.W. Peacock, J. Robertson, App. Phys. Lett., 83 (2003) 2025.

[176] K. Hermansson, G. Gajewski, P.D. Mitev, J. Phys. Chem. A, 112 (2008) 13487.

[177] T. Ichikawa, H. Tachikawa, J. Kumagai, T. Kumada, T. Miyazaki, J. Phys. Chem. A, 101 (1997) 7315.

[178] A. Couet, A.T. Motta, R.J. Comstock, R.L. Paul, Journal of Nuclear Materials, 425 (2012) 211-217.

[179] M. Preuss, P. Frankel, S. Lozano-Perez, D. Hudson, E. Polatidis, N. Ni, J. Wei, C. English, S. Storer, K.B. Chong, M. Fitzpatrick, P. Wang, J. Smith, C. Grovenor, G. Smith, J. Sykes, B. Cottis, S. Lyon, L. Hallstadius, B. Comstock, A. Ambard, M. Blat-Yrieix, J. ASTM Intl., 8 (2011).

[180] A. Hofmann, J. Sauer, J. Phys. Chem. B, 108 (2004) 14652.

[181] C. Housecroft, A. Sharpe, Inorganic Chemistry, 1st ed., Pearson Education Limited, Edinburgh Gate, 2001.

[182] H. Raebiger, S. Lany, A. Zunger, Nature, 453 (2008) 763.

[183] J.P. Perdew, MRS Bulletin, 38 (2013) 743.

[184] C.B. Gopal, A.v.d. Wlle, Phys. Rev. B, 86 (2012) 134117.

[185] H.-P. Komsa, A. Pasquarello, Phys. Rev. Lett., 110 (2013) 095505.